Determination of elastic constants of transition metal oxide based thin films using surface Brillouin scattering

Fekadu Hailu Ayele

A dissertation submitted to the Faculty of Science, Wits University,
in fulfilment of the requirements for the degree of Master of Science.

Declaration

I declare that this dissertation is my own, unaided work. It is being submitted for the degree of Master of Science in the University of Witwatersrand, Johannesburg. It has not been submitted before for any degree or examination in any other university.

____

(Signature of candidate)

30th day of March, 2016.

"Now what is history? It is the centuries of systematic explorations of the riddle of death, with a view to overcoming death. That's why people discover mathematical infinity and electromagnetic waves, that's why they write symphonies. Now, you can't advance in this direction without a certain faith. You can't make such discoveries without spiritual equipment. And the basic elements of this equipment are in the Gospels. What are they? To begin with, love of one's neighbor, which is the supreme form of vital energy. Once it fills the heart of man it has to overflow and spend itself. And then the two basic ideals of modern man—without them he is unthinkable—the idea of free personality and the idea of life as sacrifice."

Boris Pasternak, Doctor Zhivago

". . . I'm a Karamazov. . . . when I fall into the abyss, I go straight into it, head down and heels up, and I'm even pleased that I'm falling in such a humiliating position, and for me I find it beautiful. And so in that very shame I suddenly begin a hymn. Let me be cursed, let me be base and vile, but let me also kiss the hem of that garment in which my God is clothed; let me be following the devil at the same time, but still I am also your son, Lord, and I love you, and I feel a joy without which the world cannot stand and be."

Fyodor Dostoevsky, The Brothers Karamazov, Book III, Chapter 3.

To see a World in a Grain of Sand,

And a Heaven in a Wild Flower,

Hold Infinity in the palm of your hand

And Eternity in an hour.

————William Blake, Auguries of Innocence (1803)

Abstract

Bismuth ferrite ($BiFeO_3$) is a transition metal oxide that exhibits both antiferromagnetic and ferroelectric orderings and is termed a magnetoelectric multiferroic. These functional properties make it crucial for applications in various nanoelectronic devices and sensors. However, the integration of $BiFeO_3$ in devices requires the scaling down of bulk $BiFeO_3$ to nano dimensional length scales in thin film format. For this purpose, the elements of the elastic constant tensor of $BiFeO_3$ thin films are requisite, especially in multilayered or single layer-on-substrate device configurations. It is thus essential that mechanical properties of $BiFeO_3$ thin films be established due to their size and growth mode dependence.

Therefore, the study aims to determine the propagation of the surface acoustic waves and the elastic constants of $BiFeO_3$ (BFO) thin films in order to tailor the mechanical properties for device applications. In this approach the effect of morphology and microstructure on the elastic constants has been investigated.

To this end, BFO thin films have been grown following the predictions of the Structural Zone Model (SZM) using unbalanced RF Magnetron Sputtering. The RF sputter power (ad-atom energy) 30 -75 W, the negative substrate bias voltage $0-100$ V and the substrate temperature (ad-atom mobility) 100-600° C have been varied to establish the role of ad-atom energy, induced stress and ad-atom mobility on the film properties.

Atomic force microscope (AFM), scanning electron microscopy (FESEM), X-ray reflectivity (XRR), Rutherford backscattering (RBS), grazing incidence X-ray diffraction (GIXRD) and surface Brillouin scattering (SBS) techniques have been used for thin film characterization. The combined use of these techniques provide a powerful tool to correlate the microstructure and morphology of BFO thin films. Furthermore, the mechanisms of stress evolution in BFO thin films through Ar^+ implantation is demonstrated using an atomistic understanding.

Atomic force microscope (AFM) and field emission scanning electron microscopy (FESEM) studies on the surface topography (roughness) and the cross-sectional view of the microstructure of the films' growth have shown a surface roughness in

the range 0.17- 4.17 nm and a compact granular structure with columnar growth mode. These growth modes identified by FESEM have been found to be compatible to the zone 1 and zone 2 of the SZM for the deposition conditions of interest. X-ray reflectivity (XRR) provided a measure of the mass density ($7.71-8.25\pm0.05$ gcm^{-3}) and deposition rate in the range $4.1-11.1$ nms^{-1} for all the films. Rutherford backscattering (RBS) measurements of the film grown at the deposition conditions of interest yielded non-stoichiometric composition. In addition, measurements of these films under a negative substrate bias have confirmed the incorporation of Ar in the films. The amount of Ar was evaluated to be $0.1-5.5$ at. %. A study of the crystalline structure of the BFO thin films by grazing incidence X-ray diffraction (GIXRD) have shown amorphous and nanocrystalline phases in the films. The formation of these phases is strongly dependent on the ad-atom energy and surface diffusivity, which are determined by the sputter power and the substrate temperature, respectively.

For the surface Brillouin scattering measurements, a backscattering geometry was used to illuminate and collect the inelastically scattered light. The spectra were excited by the 514.5 nm line of an Innova Coherent Ar^{+} laser operated in a single axial mode. The backscattered light was guided by a series of optics to be analysed by a Sandercock (3 + 3) pass tandem Fabry–Pérot interferometer. The measured inelastically scattered light is frequency shifted by the vibrational modes propagating in the film-substrate system. These modes have been identified as the true surface acoustic waves (SAWs) comprising of the Rayleigh surface acoustic wave and the film guided modes or Sezawa waves (SWs). This observation presents the scenario of a slow on fast system. The phase velocities of the SAWs that propagate in every direction of the film-substrate system are obtained from the measured frequency shift as a function of $k_{||}h$ (where $k_{||}$ is a probing wave vector parallel to the surface of the film and h is the film thickness), which provide the experimental dispersion curves. Using the method of least squares minimization the elastic constants have been extracted through the simulation of the experimental dispersion curves. Fitting the experimental with the calculated dispersion curves using elastic constants of the BFO films as free parameters yielded the effective elastic constants of the films. Theoretical modelling based on the surface Green's functions was used to simulate and compare Brillouin spectra with the experimental spectra for selected thin films. The elastic constants obtained seem to have some relationships with the grain size that can be correlated with the stress developed in the films. The Ar^{+}incorporation has confirmed stress evolution in BFO thin films due to changes in the elastic constants based on the film growth conditions. The results have shown a decrease in

elastic constants and corresponding Bulk modulus as a signature of compressive stress. Moreover, we report an increase in the shear modulus of the biased BFO films by a factor greater than 2, $(21\ GPa < (G = C_{44}) < 49\ GPa)$. This increase is attributed to the localized deformation in the film due to Ar^{+} incorporation. The incorporation of Ar^{+} also decreases the bulk modulus by 57 %.

List of publications and conference presentations

The following list of publications and conference presentations are associated with the work presented in this thesis.

List of publications

F.H. Ayele, D.M. Wamwangi, J.D. Comins, D.G. Billing, E. Njoroge, Surface Brillouin light scattering from surface acoustic waves in $BiFeO_3$ thin Films, in preparation.

Lists of Conference Presentations

- **F.H. Ayele** , D.M. Wamwangi and J.D. Comins. June 29-July3 2015. Oral Presentation entitled Surface Brillouin characterizations of Bismuth Ferrite thin films. 2015 South African Institute of Physics annual conference held on Port Elizabeth , South Africa.
- **F.H. Ayele** , D.M. Wamwangi and J.D. Comins. October 2014. Poster Presentation entitled Characterization of Bismuth ferrite thin films for surface Brillouin scattering. 6^{th}Cross-Faculty Graduate symposium Wits University, Johannesburg, South Africa.
- **F.H. Ayele** , D.M. Wamwangi and J.D. Comins. April 2014. Poster presentation entitled Synthesis and characterizations of Bismuth ferrite thin film surface by X-ray reflectivity and atomic force microscope measurements. NRF/DST Center of excellence in strong materials student workshop, Wits University, Johannesburg, South Africa.
- **F.H. Ayele** , D.M. Wamwangi and J.D. Comins. May 2015. Poster presentation entitled Characterization of Bismuth ferrite thin films for surface Brillouin scattering. NRF/DST Center of excellence in strong materials student workshop, Wits University, Johannesburg, South Africa.
- F.H. Ayele , D.M. Wamwangi and J.D. Comins. Oral Presentation entitled Surface Brillouin characterizations of Bismuth Ferrite thin films. 8th African Laser Center Workshop held on Stellenbosch South Africa.

Acknowledgements

Above all, I would like to thank the almighty God, the God of Abraham, Isaac and Jacob for the Love he has for all of us.

Second, I would like to express my sincere gratitude to my supervisors Dr. Daniel Wamwangi and Prof. Darrell Comins, for their advice, support and guidance during the period of the thesis.

Special thanks should go to Dr. Wamwangi for his continuous availability and willingness for discussion, patience, motivation and positive attitude and Prof. Comins for his relentless efforts for the operations and functioning of the laser spectroscopy laboratory.

Material Physics Research Institute, School of Physics and the X-ray Diffraction Facility in School of Chemistry are thanked for provision of the requisite research infrastructure for this project.

I am very thankful to the Center of Excellence in strong materials, University of the Witwatersrand Post Graduate Merit Award (PMA), JC Carstens Funding and the African Laser Centre (ALC) for their financial support.

Finally, I would like to thank all the people with whom I have been working, for their timely help and contribution to this research: Special mention is given to Kudakwashe Jakata for his assistance and guidance in the practical aspects of surface Brillouin scattering (SBS) and Jonah Kuria for his encouragement.

Acronyms

- AFM····················Atomic force microscopy
- BFO···················· Bismuth ferrrite
- FESEM················· Field emission scanning electron microscopy
- GIXRD················· Grazing incident x-ray diffraction
- HRTEM················· High-resolution transmission electron microscopy
- RBS···················· Rutherford backscattering spectroscopy
- RF······················Radio frequency
- RSM····················Reciprocal space mapping
- SBS ····················Surface Brillouin scattering
- SNR····················Signal noise ratio
- SZM····················Structural zone model
- XRR ···················X-ray reflectivity

Contents

1 Introduction **1**

1.1 Properties of single phase multiferroic $BiFeO_3$ . . . 5

1.1.1 Structural properties . . . 5

1.1.2 Electrical properties . . . 8

1.1.3 Magnetic properties . . . 8

1.1.4 Mechanical properties . . . 10

1.2 Goal specifications . . . 10

1.3 Dissertation layout . . . 11

2 Theoretical Framework **13**

2.1 Elasticity fundamentals . . . 14

2.2 The elastodynamics of surface acoustic waves in thin supported films . . . 15

2.3 Surface Brillouin Scattering in thin supported films . . . 22

2.3.1 Basic principles of Surface Brillouin Scattering (SBS) . . . 22

2.3.2 SBS cross-section . . . 23

2.3.3 Kinematics of SBS . . . 26

2.4 Thin film growth . . . 28

2.4.1 Ferroelectric (BFO) thin film growth . . . 31

2.4.1.1 Film nucleation and growth . . . 31

2.4.1.2 Island coalescence . . . 32

2.4.1.3 Thickening . . . 33

2.4.1.4 Grain growth . . . 34

2.4.1.5 Surface melting . . . 36

2.4.2 Structural Zone Model (SZM) . . . 36

2.5 RF Magnetron Sputtering of $BiFeO_3$ thin films 38
2.5.1 Substrate temperature 38
2.5.2 Film thickness 40
2.5.3 Substrate bias voltage 40
2.5.3.1 Incorporation of foreign atoms 41
2.5.4 Sputter power 41
2.6 Stress in RF magnetron sputtered thin films 41
2.6.1 Stress in sputtered thin films 41
2.6.1.1 Thermal stress (extrinsic stress) 42
2.6.1.2 Intrinsic stress / compressive and tensile strain . . 42

3 Characterization techniques 43
3.1 Atomic Force Microscopy (AFM) 43
3.2 Field Emission Scanning Electron Microscopy (FESEM) 45
3.3 X-ray Reflectometry (XRR) 45
3.4 Rutherford Backscattering Spectroscopy (RBS) 46
3.5 Grazing Incidence X-ray Diffraction (GIXRD) 48
3.5.1 Bragg's condition 49
3.5.2 Crystallite size 49
3.5.3 Intrinsic strain determination 50

4 Experimental 52
4.1 RF Magnetron Sputtering system 52
4.2 Atomic Force Microscopy (AFM) apparatus 53
4.3 Field Emission Scanning Electron Microscopy (FESEM) 54
4.4 X-ray Reflectivity (XRR) 54
4.5 Rutherford Backscattering (RBS) 54
4.6 Grazing Incidence X-ray Diffraction (GIXRD) 55
4.7 Surface Brillouin Scattering (SBS) 55
4.7.1 Experimental setup 55
4.7.2 Laser 57
4.7.3 Fabry–Pérot interferometer 58

5 Results & Discussion: Characterization studies **61**

5.1 Introduction 61

5.2 Surface topography and cross-section image studies 61

5.3 Stoichiometric (composition) studies by RBS 66

5.4 Density, thickness, surface and interface roughness measurements . 71

5.5 Phase identification studies 75

6 Results & Discussion: Surface Brillouin Scattering studies **82**

6.1 Measured and simulated SBS spectra for $BiFeO_3$ thin films 82

6.2 Derivation of effective elastic constants of BFO thin films 90

6.3 Stress evolution 95

7 Conclusions and Future Work **97**

7.1 Conclusions 97

7.2 Future work 99

Bibliography **101**

List of Figures

1.1 The bulk crystal structure of BFO and its ferroelectric polarization (arrow), antiferromagnetic plane (shaded planes) and Hexagonal unit cell of BFO 7
1.2 Ferroelectric hysteresis loop for $BiFeO_3$ measured at 15 kHz on (100) Si substrates. 8
1.3 Part of $BiFeO_3$ lattice. The arrows show the Fe^{3+}moment direction of the proposed model 10

2.1 Rectangular plane system for the surface acoustic wave propagation in thin films (a) propagation direction and (b) sagittal plane coordinates 17
2.2 Examples of velocity dispersion curve of the BFO thin films. 24
2.3 Backscattering geometery 27
2.4 The process of sputtering 29
2.5 Schematic diagram of unbalanced magnetron sputtering setup . . . 30
2.6 Processes in the nucleation and growth of thin films on a substrate . 32
2.7 Grain structure evolution during deposition of polycrystalline thin film 34
2.8 Grain growth in a two dimensional polycrystalline thin films 35
2.9 Typology of the structure zone models 37
2.10 Growth modes 38

3.1 Atomic Force Microscope principles 44
3.2 Schematic diagram depicting the X-ray total external reflection from a film substrate system 46
3.3 Schematic illustration of a typical RBS experiment 47
3.4 A typical RBS spectrum of a BFO thin film deposited on a silicon substrate with sputter power of 30 W. 48

3.5 Bragg's condition for diffraction in real space 49
3.6 GIXRD profile with its 2θ peak position 50

4.1 RF magnetron sputtering system. 53
4.2 Systems of optics and other instrumentations of surface Brillouin scattering 56
4.3 Schemetic diagram of the experimental arrangement used for surface Brillouin scattering spectroscopy 57
4.4 Figure of laser gain profile 58
4.5 A photograph of a (3+3) multipass Tandem interferometer 59
4.6 Translational stage of the two Fabry–Pérot interferometers , Fabry–Pérot 1, Fabry–Pérot 2 that are able to scan synchronously 60

5.1 Surface topography of the pristine BFO thin films deposited at 30 W and 40 W for 5 min at room temperature and $V_b = 0\ V$, respectively. 62
5.2 Surface topography of the pristine BFO thin films deposited at 50 W and 75 W for 5 min at room temperature and $V_b = 0\ V$, respectively. 62
5.3 AFM micrographs of the pristine BFO thin films grown at 50 W, at [a] 100°C and [b] 200°C for 5 min. The substrate bias voltage was set to zero for both cases. 63
5.4 AFM images of the pristine films produced at 50 W, at [a] 400°C and [b] 600°C for 5 min. The substrate bias voltage was set to zero for both cases. 63
5.5 AFM images of films grown at 50 W with varying substrate bias of [a] $-25\ V$ $(R_q = 0.232)$ and [b]$-50\ V$ $(R_q = 0.197)$, respectively. . 64
5.6 AFM micrographs of films grown at 50 W with substrate bias of [a]$-75\ V$ $(R_q = 0.219)$ and [b] $-100\ V$ $(R_q = 0.383)$, respectively. 64
5.7 FESEM cross-sectional image of the BFO films prepared at [a] 30 W-3 hrs, [b] 30 W-5 hrs, ... 66
5.8 FESEM cross-sectional image of the BFO films prepared at [c] 30 W-6$\frac{1}{2}$ hrs and [d] 75 W-3 hrs. 66
5.9 RBS spectrum of as deposited layer of BFO 67

5.10 [a] RBS spectra of the pristine BFO deposited at 30 *W*, 40 *W,* 50 *W* and 75 *W* for 15 *min* at room temperature and zero substrate bias voltage. The black, red, green and blue plots are used for comparison of the raw data. [b] A zoom in from channels 200 to 400 to depict the compositional variation of BFO films under the various deposition conditions. 68

5.11 [a] RBS spectra of BFO deposited with a -50 *V*, -75 *V* and -100 *V* substrate bias voltage. The black, red and green plots depict the experimental data. Fig. [a] is zoomed in from channels 200 to 450 as shown in [b] in order to see the compositional variation among the films. 69

5.12 Depth profile analysis for films produced at 50 *W* and zero bias as a function of deposition time. 71

5.13 Raw (measured) and simulated XRR spectrum of RF magnetron sputtered BFO/SiO_2/Si layer stack with sputter power of 40 *W* and deposition time of 3 *min.* 72

5.14 XRR spectra of the as-deposited BFO samples with different sputtering power values, substrate bias voltages and temperatures. 72

5.15 Graph of bismuth density versus concentrations of the films as determined by RBS. The films were prepared at different sputter powers and hence have different densities. The bismuth content of films fabricated at 30 *W* and 40 *W* is the same (25.5 at %) but the films have different densities. 74

5.16 Bismuth contents in RF substrate biased and with different sputter power films as determined from RBS measurement. 75

5.17 Room temperature GIXRD patterns from BFO thin films deposited with different RF sputter powers. 76

5.18 Variations of grain size with substrate temperature. 77

5.19 Variations of grain size with sputter deposition parameters. 78

5.20 GIXRD patterns of BFO films with various substrate negative bias voltage. 79

5.21 The GIXRD patterns of BFO films produced at various substrate temperatures. 81

6.1 Dispersion curves of thin film of thickness h ranging from 30 to 652 *nm*. 83

6.2 The simulated cross sections of an elastodynamic Green's function calculation using the G_{33} component. 85

6.3 Typical Brillouin spectrum of the 318 nm thick sample taken at an incidence angle of 71.5°. 86

6.4 [a and b] Representative measured SBS spectra of intensity as a function of the frequency shift for BFO films produced at 50 *W* sputter power on a silicon substrate. 88

6.5 Representative measured SBS spectra of intensity as a function of the frequency shift for BFO films produced on a Si substrate at 50 *W* with a substrate bias of -50 *V*, 50 *W* with no substrate bias and 75 *W*, respectively. All the films have the same thickness of 228 *nm*. 89

6.6 Dispersion curves (measured and calculated) of the pristine films produced at 75 *W* and zero substrate bias voltage. The circles are the measured raw data. 91

6.7 Dispersion curves (measured and calculated) of the pristine films produced at 50 *W* and zero substrate bias voltage. The circles are the measured raw data. 91

6.8 Dispersion curves (measured and calculated) of films fabricated at 50 *W* and negative substrate bias voltage of -50 *V*. The circles are the measured raw and the solid squares represent the calculated best fits to the raw data. 92

6.9 Simulated and measured surface Brillouin spectra at 71.5° incident angle for a 109 *nm* BFO film fabricated at 75 *W* on a silicon substrate. 93

6.10 Simulated and measured surface Brillouin spectra at 71.5° incident angle for a 228 *nm* BFO film fabricated at 50 *W* on a silicon substrate. 94

6.11 Simulated and measured surface Brillouin spectra at 71.5° incident angle for a 91 *nm* BFO film fabricated at of 50 *W* and -50 *V* negative substrate bias voltage on a (001) silicon substrate. 94

6.12 Surface acoustic wave (SAWs) dispersion curves of films produced with -50 V (circular data points) and zero (triangular data points) substrate bias voltage 96

List of Tables

4.1 The sputtering parameters used for BFO growth. 53

5.1 Effect of deposition parameters on surface roughness and crystallite size 65

5.2 Stoichiometry of the BFO layer on (001) Si by RBS 70

5.3 Values of the parameters obtained by fitting X-ray reflectivity for films produced under diverse conditions 73

5.4 Effect of bias voltage and temperature on lattice parameters and macro strain in BFO films 80

6.1 $k_{||}h$ values for the various film thicknesses of BFO/Si 82

6.2 Effective elastic constants of BFO films obtained from the best fit of the calculated to the measured phonon dispersion curves, under the assumption of homogeneous films. 93

Chapter 1.

Introduction

Transition metal oxides exhibit a wide range of electronic, magnetic, optical and mechanical properties and constitute one of the most interesting classes of materials, which include insulators, semiconductors, multiferroics, and semi-metals [1]. Among these material classes multiferroics have received widespread interest due to their correlated functional properties such as ferromagnetism, ferroelectricity, ferroelasticity and ferrotoroidicity, which can exist independently within separate phases as a composite multiferroic. Alternatively these properties may be coupled to each other in single phase materials [2],[3],[4]. The coexistence of ferromagnetism and ferroelectricity, also known as multiferroism, has been found in perovskite based transition metal oxides.

The increased research interest in spintronics and also the drive towards the evolution of novel sensors that can be controlled either by magnetic or electric fields at room temperature has stimulated research on transition metal oxide based multiferroics. Thus, the mechanical, optical, electrical and magnetic properties of transition metal oxides have important practical applications.

$BiFeO_3$ (BFO) is the most important multiferroic material and is characterized by a high ferroelectric Curie temperature (Tc~1103 K) and an antiferromagnetic Neel temperature (T_N~643 K) [5]. In addition to its excellent optical properties [6], strong coupling between ferroelectric and magnetic orders have been observed in BFO at room temperature, making it the best candidate for room-temperature multiferroic devices[2]-[3] .

Moreover, the long range ordering properties of this material have been demonstrated in thin films, single crystal and bulk forms [6], [7], [8]. Unlike other multiferroic inorganic materials with perovskite structures, BFO has been studied extensively by different researchers because it is a lead (Pb) free and an environmentally clean material [2],[3],[4]. Despite the enormous research work on the magneto-electric properties of BFO, studies on the mechanical properties of multiferroics

(BFO) have been largely ignored. Specifically, as the mechanical properties of materials are size and phase dependent, the properties of thin films significantly differ from those of the bulk material [9]. Taking into account the fact that most practical applications of functional devices are fabricated in thin film format, there is a need to precisely determine the mechanical properties. This can be achieved through derivation of elastic constants from the dynamics of the surface acoustic waves on a film-substrate system. In this respect, therefore, it is imperative that the elastic constant tensor of thin films of BFO be determined, as it provides crucial information required for the integration of BFO in nanoelectronic devices and for light-controlled coherent acoustic phonon sources [10]. The elastic properties of BFO thin films are directly related to the nature of the atomic bonding, microstructure and crystal structure of the film.

$BiFeO_3$ thin films have been fabricated using unbalanced RF magnetron sputtering on a Si(001) substrate based on the structural zone model (SZM). Previous studies on the elasticity of thin films have not correlated the effects of variation in the film growth modes with their elastic constants.[10]. Thin films generally consist of two competing dimensional length scales (thickness and grain size), and usually possess a columnar microstructure and strong texture. Previous research has shown that the deposition parameters (bias voltage, substrate temperature, sputtering power etc.) strongly affect the microstructure and surface morphology of the thin films [11],[12],[13]. Thus, the correlation and effect of the deposition parameters on the elastic constants of $\mathrm{BiFeO_3}$ (BFO) thin films should be investigated.

This research establishes the components of the elastic constant tensor of $BiFeO_3$ as a transition metal oxide material in thin film format. This work enables the desirable properties of the polycrystalline (amorphous) thin films of $BiFeO_3$ to be engineered through manuplation of their microstructure. The microstructure of the films is the most defining element in determining the physical properties of films with nanometer scale thickness. The most important microstructural properties of thin films include thickness, density, grain size, grain size distribution, crystallographic texture and surface/interface roughness. Controlling the grain size is helpful for characterizing, optimizing and determining the desirable mechanical properties of thin films. It is noted that grain size control has found critical applications in magnetic data storage applications in which the grain size distribution in magnetic thin films have a significant influence on recording properties. Currently, the highest recording densities have been obtained by reducing the grain sizes to enable perpendicular recording. This concept has significantly increased the storage densities due to the reduced bit size without compromising the signal to noise ratio (SNR) [14]. Moreover, the

influence of grain size and its distribution can affect the various physical properties of the thin films, and a scientific approach over the control of these parameters is demanded, such as in coatings for solar cells [15],[16],[17],[18],[19], thermoelectric materials [20],[21],[22],[23], and thin film transistors [5],[24],[25][26],[27],[28]. Sputtering parameters like sputter power, substrate temperature and substrate bias voltage are used as controlling mechanisms for the grain growth in amorphous and polycrystalline films. Thornton's zone model provides an approach to describe and correlate the film growth morphology with the Ar gas pressure and the ratio of the melting point of the sputtered material to substrate temperature.

Films grown by RF magnetron sputtering can be nanocrystalline, polycrystalline, textured or amorphous. These phases do not possess single crystal like properties. Thus the determination of their elastic properties is highly dependent on the deposition conditions, which can be tailored using the concept of the structural zone model [29].

Surface Brillouin scattering (SBS) has been employed to study the propagation of acoustic phonons in thin supported films. The determination of the velocity dispersion curves makes this technique suitable to establish the elastic constants of BFO films. SBS has been a standard protocol within optical techniques in the inelastic light scattering measurements of diverse materials ranging from bulk to thin film samples. The study of acoustic phonon excitations in solids by inelastic scattering of light was first investigated by Brillouin [8] and independently by Mandelshtam [30]. After the invention of the laser, the Brillouin scattering (BS) technique became a popular method for the determination of elatic constants of materials. Many elegant experiments were carried out and showed that BS is an excellent means of investigating the elastic and photo-elastic properties of materials [31], as well as phase transitions [32],[33]. An advancement in these studies occurred with the introduction of the high-contrast spectrometer [34], enabling measurements on small and even opaque samples. SBS has been used to study solids and liquids [35], supported transparent films [36], and more recently, spherical nanoparticles [37], cellulose nanocrystal films [38], nanoscale permalloy stripes [39], carbon thin films [40], thin single silicon layers [41], planar magnonic crystals [42] and sodium silicate glasses [43]. A detailed and comprehensive treatment of the theoretical aspects of SBS can be found in [35], [44], [45]. Different researchers have employed various techniques to establish the values of the elastic constants of different sample formats of BFO. Borissenko *et al.* [46] studied the lattice dynamics of multiferroic single crystal $BiFeO_3$ by inelastic X-ray scattering, and the phonon dispersions along several directions were measured. A subset

of the elastic moduli of $BiFeO_3$ (C_{11}, C_{33}, C_{44} and C_{66}) was derived. Shang *et al* [47] determined the elastic properties of rhombohedral and cubic $BiFeO_3$ by using first principle DFT (density functional theory) calculations. The magnetic, dielectric and thermal properties of $BiFeO_3$ at room temperature have also been studied by Shang *et al.* [47]. Ruello *et al.* [10] used femtosecond laser pulses and measured coherent GHz acoustic phonons that are photogenerated and photodetected in $BiFeO_3$ multiferroic single crystals; their work established the corresponding sound waves for longitudinal and two transverse acoustic waves and experimentally evaluated the elastic coefficients of the multiferroic compound $BiFeO_3$ (such as, C_{11}=220 GPa, C_{33}=140 GPa, C_{12}=120 GPa, C_{13}=60 GPa, C_{44}=35 GPa, C_{14}=20 GPa and C_{66}=1/2(C_{11}-C_{12})). So far surface Brillouin scattering has not been used to derive the elastic constant tensor of Bismuth Ferrite thin films. Furthermore, the properties of $BiFeO_3$ thin films can be tailored to the desired material properties by ion implantation through stress evolution in the thin film. Implantation of argon/oxygen ions is considered as a possible approach to manipulating the properties of multiferroic materials through induced lattice distortion and formation of localized micro- or macro- strain in the thin films. The stress distribution and the relaxation of the multiferroic oxides such as $BiFeO_3$ have been studied by many researchers using various techniques. Cruz *et al.* [48] studied the stability of domains and domain walls in $BiFeO_3$ thin films using both a piezoelectric force microscopy and phase-field simulations. Nakashima *et al* [49] have investigated the influence of stress on the structural and ferroelectric properties of polycrystalline $BiFeO_3$ thin films using a membrane substrate for relaxing stress. Using reciprocal space mapping (RSM), they confirmed the stress dependence on the crystal structure of polycrystalline BFO thin films on Pt (200 nm)/TiO_2(50 nm)/SiO_2(600 nm)/Si (625 nm) substrate (stress-constrained BFO film) and on the Pt (200 nm)/TiO_2(50 nm)SiO_2(600 nm)/Si (15 nm) membrane substrate (stress-relaxed BFO film). Very recently, a strain driven morphotropic phase boundary (MPB) has been discovered in BFO thin films and both tetragonal and rhombohedral phases were observed by using high-resolution transmission electron microscopy (HRTEM) [50]. The epitaxial strain force changes the BFO rhombohedral phase into a tetragonal phase and in the process creates a MPB. Upon removing the strain force, the crystal structure reverts back to its original rhombohedral phase. Hence, due to compression and relaxation, the material can swing back and forth between the two phases or mixed phases. The determination of stress evolution of multiferroic oxides of $BiFeO_3$ thin films using elastic constants measured by SBS is a first attempt and to the best of our knowledge has not been done before.

1.1 Properties of single phase multiferroic BiFeO$_3$

1.1.1 Structural properties

The single phase multiferroic BFO has received extensive research interest due to its lead (Pb) free nature, room temperature multiferroism, domain wall functionalities and rich and complex phase diagrams (large polarization). In addition, the material's complex physical and structural properties can be tailored and controlled through various deposition parameters in a two dimensional thin film format for applications purposes.

From a thin film perspective, the film has a different crystal structure as compared to its bulk forms. At room temprature, bulk BFO has a G-type antiferromagnetic (AFM) (pseudo cubic) rhombohedral R3c structure. The structure of BFO is distinguished by two distorted perovskite unit cells (a_r= 3.96 Å, α_r = 0.6°) connected along their body diagonal, denoted by the pseudo cubic <111>, to form a rhombohedral unit cell as shown Fig. (1.1 a & b) [50],[51],[52]. The rotation of the two oxygen octahedra and the Fe-ion are an important structural parameter that determines the crystal structure of BFO. In this structure the two oxygen octahedra of the cells that appear along <111> are rotated counterclockwise and clockwise around <111> by ±13.8°and the Fe-ion is displaced by 0.135 Å along a similar axis away from the oxygen octahedron center position. The ferroelectric state is mediated by a large displacement of Bi-ions relative to the FeO_6 octahedra. Generally speaking, the structure of BFO is the result of:

- The phase shifts (the eight polarization variants) related to the four structural variants that are facilitated by the ferroelectric polarizations that lies along the pseudo cubic <111> directions.
- The antiferromagnetic (AFM) ordering of BFO is G-type in which each Fe^{3+} spin antiparallel to the six nearest neighbour spins that are aligned ferromagnetically within the (111) plane and antiferromagnetically between adjacent (111) plane. Besides, BFO show a spin cycloid structure in the bulk [50] and the antiferromagnetically aligned spins lie within the (111) plane that is perpendicular to the ferroelectric polarization along the axes within that plane. This means that polarization switching by either 71° or 109° along the six axes and perpendicular to the plane (111) will lead to a change in orientation of the magnetization plane (111), [50] (Fig.1.1[a]). The magnitude of the displacement of the ionic shifts are Bi: 0.62 Å along [111], Fe: 0.23 Å along [111] , O: 0.30 Å along [111] (all values ±0.03 Å). The unit cell of BFO

can be represented by having twice the volume of the unit molecular cell, and generated by taking three face diagonals meeting at a vortex of the cube depicted below as three intersecting edges of the rhombohedron.

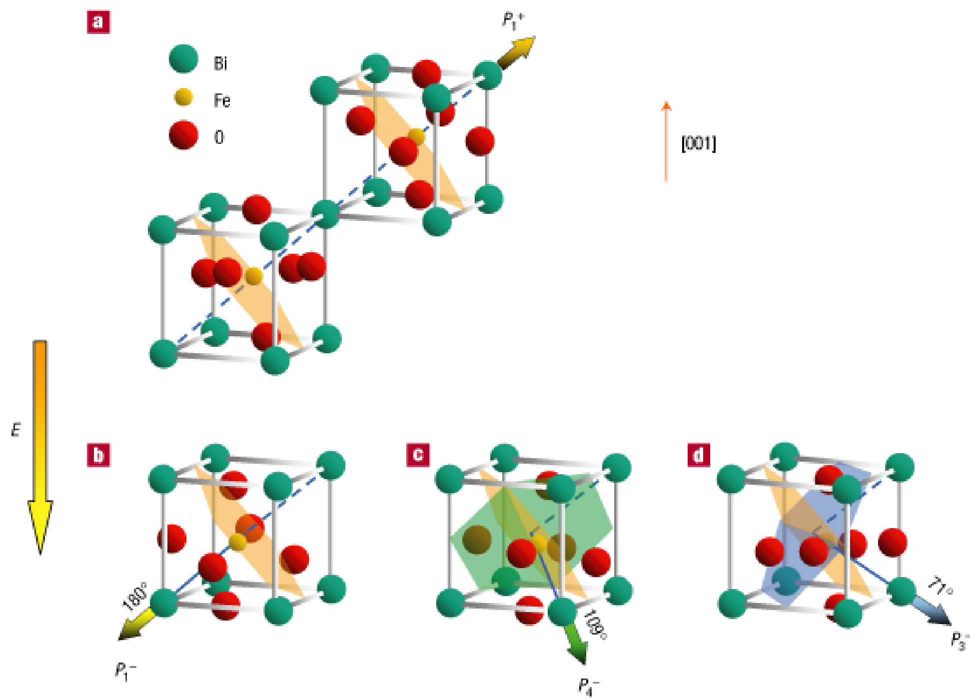

Fig.(a)

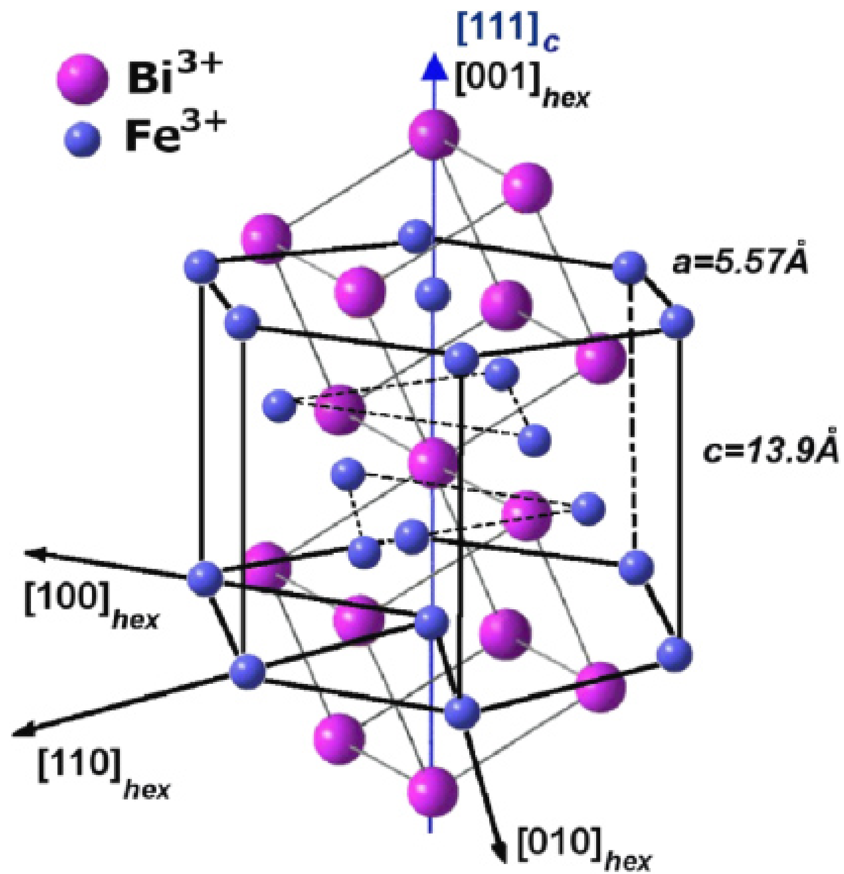

Fig.(b)

Figure 1.1: (a) The crystal structure of BFO and its ferroelectric polarization (arrow) and antiferromagnetic plane (shaded planes) [51] (b) Hexagonal unit cell of BFO [52].

1.1.2 Electrical properties

The electrical field applications and electrical characterization of $BiFeO_3$ ceramic material are very difficult due to its high resistivity and its very low conductivity. Variation from oxygen composition and the valence state alteration of Fe ions (+3 to +2 state) during the long sintering process has led to high conductivity in $BiFeO_3$. The hysteresis loop measured by Teague *et al.* [53] and shown in Fig. (1.2) confirmed the ferroelectricity in BFO. Their experiment under liquid nitrogen conditions yielded lower leakage current due to a lower charge carrier density and mobility. The measured spontaneous polarization was found to be 3.5 $\mu C/cm^2$ and 6.1 $\mu C/cm^2$ along the <100> and <111> directions, respectively. The measured results are much lower than anticipated, especially for ferroelectric material having such a high Curie temperature and a large distortion. Thus, leakage current due to defects and stoichiometry screen polarization, thereby diminishing its ferroelectric properties. To circumvent the leakage current, the substitution of Fe^{3+} by other transition-metal ions in $BiFeO_3$ is proposed.

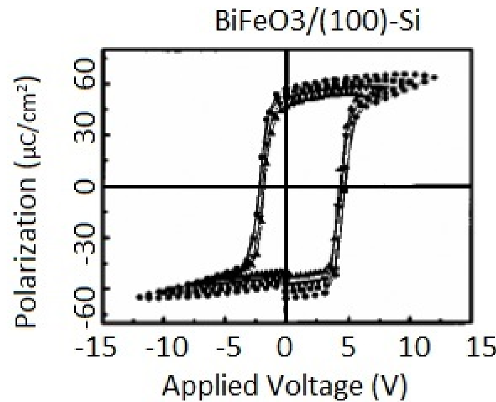

Figure 1.2: Ferroelectric hysteresis loop for $BiFeO_3$ measured at 15 kHz on (100) Si substrates [53] ,[54].

1.1.3 Magnetic properties

Broadly speaking, single phase materials can be subdivided into the following categories: materials with a distinct magnetic and ferroelectric ordering (type 1 multiferroics in the classification established by Khomskii [55]) and materials exhibiting a magnetic transition with collateral ferroelectric ordering (type 2 multiferroics).

- In type 1 multiferroics, the magnetism is attributed to partially filled d shells

and the ferroelectric distortions and the magnetic orderings cannot be produced by the same sources of ions [55]. $BiFeO_3$ is an example of a type 1 multiferroic.

- In type 2 multiferroics, the ferroelectric ordering coincides with a magnetic transition, specifically at low temperature; ferroelectricity is thus produced by the magnetic order. $BiFeO_3$ is a G-type antiferromagnet, with each Fe^{3+} spin antiparallel to the six nearest neighbour spins [55]. Sosnowska [56] proposed a modified G-type antiferromagnetic structure in which the spin of Fe^{3+} is subjected to a long range modulation as shown in Fig. 1.3. This antiferromagnetic structure of bulk $BiFeO_3$ is a complex interchange between spin, charge and lattice degrees of freedom. The ferroelectricity present produces a small spin canting through the Dzyaloshinskii-Moriya interaction. This small spin canting generates an inhomogeneous magnetization that can also couple to the polarization. The magneto-electric coupling wavelength ($\lambda > 60$ nm) leads to a spin cycloid propagating along the [110] direction, which cancels out the small ferromagnetic moment produced by the spin canting [56]. The suppression of the cycloidal magnetic structure in the thin films produces a small magnetization from the canted spins. The magnetic signal shown in the $BiFeO_3$ thin films results from the iron oxide impurity phases present in the film. The phases that have been observed to contribute to the magnetic response are γ-Fe_2O_3 or Fe_3O_4, or mixed valence effects on the Fe site [56].

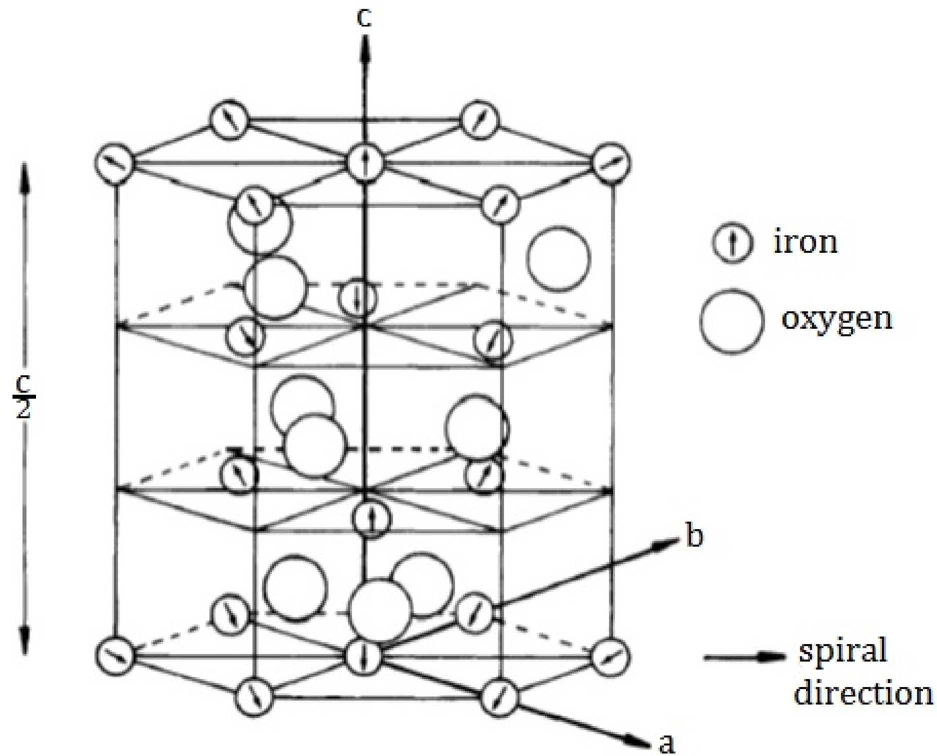

Figure 1.3: Part of $BiFeO_3$ lattice.The arrows show the Fe^{3+}moment direction of the proposed model. The spiral period is decreased for illustration purpose [56].

1.1.4 Mechanical properties

The mechanical characteristics of the $BiFeO_3$ thin films are such that the elastic deformation behaviour can be readily obtained from SBS measurements. The elastic constants that have been determined are related to the stresses developed in the thin films during film growth. Stress developed in the thin films are of intrinsic and extrinsic nature. The intrinsic stresses are induced by the impurities and defects introduced in the thin film during growth, whereas the extrinsic stresses are introduced in the thin film due to lattice and thermal expansion coefficient mismatches between the film and substrate. The latter component is very small as compared to the stress resulting from the former [57],[58] when the films were deposited at lower temperature.

1.2 Goal specifications

This dissertation focusses on the synthesis and characterization of multiferroic $BiFeO_3$ (BFO) thin films to establish the role of morphology and microstructure on their

elastic constants. BFO films have a wide range of electronic device and industrial applications, either as multilayered or single layer coatings. They are used in diverse applications such as solar cells and thin film transistors. The elastic constants of the $BiFeO_3$ thin films are some of the most desirable properties needed in device applications. To this end, thin films of $BiFeO_3$ have been grown on (001) Si under various deposition parameters using RF magnetron sputtering based on the SZM. The main objectives of the dissertation are:

• Optimization of process parameters that determine thin film growth through extraction of deposition rates with varied ad atom energies (sputter power and gas pressure) and roughness using atomic force microscopy (AFM).

• Characterization of thin film properties (thickness, density, interfacial roughness and crystal structure) using X-ray reflectometry (XRR) and phase identification using grazing incidence X-ray diffraction (GIXRD).

• Determination of the film composition using Rutherford backscattering spectroscopy (RBS).

• Establishing the effects of a variation in microstructure using field emission scanning electron microscopy (FESEM).

• Determination of stress evolution in $BiFeO_3$ thin films using elastic constants, upon substrate biasing during film growth.

• Derivation of the elastic constant tensor of $BiFeO_3$ thin films using SBS from the velocity dispersion curves of the grown thin films based on the Structural Zone Model.

1.3 Dissertation layout

The layout of the dissertation is presented below.

Chapter 2. A detailed description of the fundamental theoretical framework of elasticity, the propagation of elastic waves and surface Brillouin scattering mechanisms in thin supported films is given. In addition, the dynamics of thin film growth is presented. The basic concepts of the important process parameters, and fundamental processes through which the micro-and nano structure of the polycrystalline (amorphous) film evolve are discussed.

Chapter 3. The theoretical framework of the characterization techniques used throughout the studies are described. This includes atomic force microscopy (AFM), field emission scanning electron microscopy (FESEM), X-ray Reflectometry (XRR),

Rutherford backscatering spectroscopy (RBS), grazing incidence X-ray diffraction (GIXRD) and surface Brillouin scattering (SBS).

Chapter 4. The experimental setup and procedure for the main characterization techniques used are presented in detail in this chapter.

Chapter 5. This chapter is devoted to a discussion of the results from the AFM, FESEM, XRR, RBS and GIXRD characterizations, which are pre-requisite for SBS measurements.

Chapter 6. The results from surface Brillouin scattering both from measurement and theoretical formulations, are presented.

Chapter 7. This chapter presents a summary of the main and important results in this dissertation. Moreover, the unanswered and emerging questions and ideas are featured in the future outlook section.

Chapter 2.

Theoretical Framework

This chapter gives a theoretical description of the elasticity of materials, the propagation of elastic waves (surface acoustic waves) and a description of the surface Brillouin scattering technique on thin supported films. Finally, thin film deposition by the RF magnetron sputtering technique is discussed. Using the concepts of stress and strain, the mathematical formulation of Hooke's law is presented for an isotropic solid. The number of elastic constants which feature in the stress-strain relation are dependent on the symmetry characteristics of a solid. These concepts are essential in the derivation of the elastic constants of bismuth ferrite $(BiFeO_3)$ thin films using surface Brillouin scattering. The propagation of the elastic waves in a material are naturally occuring phenomena associated with the dynamical thermal fluctuations of phonons that move with small amplitude in the sample. This treatment is true for opaque materials, as the ripple mechanism dominates over the elasto-optic mechanism. The film used in this work presents a classical example of the surface ripple mechanism encountered in SBS. SBS is a well established and most utilized optical technique for investigations of the elastic constants of near opaque materials. SBS is a technique that is based on the measurements of elastic waves propagating in the materials in the GHz frequency range. It is a non destructive and contactless method.

To fabricate high quality films (optically smooth) with the desired composition, the deposition technique for ferroelectric oxides requires a precise control of the fluxes of elements or stoichiometrically transfering source materials to the substrate. It is because the microstructures and properties of the perovskite ferroelectric thin films are highly dependent on the composition (stoichiometry), orientation (as ferroelectric materials are anisotropic) and the initial stage of the film's growth. To this effect, much effort has been expended on the synthesis of ferroelectric perovskite oxides with the progress in thin film deposition techniques. The RF magnetron sputtering technique is the most popular method for ferroelectric thin film deposition, due to

its inherent advantages:

- good control of film stoichiometry
- orientation and high deposition rate.

In this work, high quality ferroelectric thin films have been deposited using the RF magnetron sputtering technique.

2.1 Elasticity fundamentals

For an isotropic elastic medium the displacement vector field $\vec{u}(\vec{r},t)$ and the stress tensor $\sigma_{\alpha\beta}(\vec{r},t)$ can be related by using the generalized form of Hooke's law [59]:

$$\sigma_{\alpha\beta} = \sum_{\gamma\sigma} C_{\alpha\beta\gamma\sigma} \frac{\partial u_\gamma}{\partial x_\sigma} \tag{2.1}$$

where $\sigma_{\alpha\beta}$ is the second rank stress tensor, $C_{\alpha\beta\gamma\sigma}$ is the fourth-rank elastic modulus tensor and $\frac{\partial u_\gamma}{\partial x_\sigma}$ is the second rank strain tensor, which can be expressed as $\eta_{\gamma\sigma} = \frac{\partial u_\gamma}{\partial x_\sigma}$.
Then the strain tensor can also be defined as

$$\eta_{\gamma\sigma} = \frac{1}{2}(\frac{\partial u_\gamma}{\partial x_\sigma} + \frac{\partial u_\sigma}{\partial x_\gamma}) \tag{2.2}$$

Since the stress and strain tensors are symmetric, the elastic constants $C_{\alpha\beta\gamma\sigma}$ can be given by two indices (x and y) as follows:

$C_{\alpha\beta\gamma\sigma} \longrightarrow C_{xy}$

$\alpha\beta \to x$, $\gamma\sigma \to y$

$11 \to 1$, $23,32 \to 4$

$22 \to 2$, $13,31 \to 5$

$33 \to 3$, $12,21 \to 6$

Using symmetry and energy arguments the C_{xy} can be related to the acoustic wave speed v_{xy} and density ρ through $C_{xy} = \rho v_{xy}^2$ [60]

For an isotropic medium the elastic constant matrix diminishes into:

$$\begin{bmatrix} C_{11} & C_{12} & C_{12} & 0 & 0 & 0 \\ C_{11} & C_{11} & C_{12} & 0 & 0 & 0 \\ C_{12} & C_{12} & C_{11} & 0 & 0 & 0 \\ 0 & 0 & 0 & C_{44} & 0 & 0 \\ 0 & 0 & 0 & 0 & C_{44} & 0 \\ 0 & 0 & 0 & 0 & 0 & C_{44} \end{bmatrix}$$

In this format only two independent elastic constants C_{11} and C_{44} are required as the third component C_{12} is expressed in terms of C_{11} and C_{44} based on the Cauchy formalism as $C_{12} = C_{11} - 2C_{44}$.

The elastic constants can be interpreted using the elastic moduli, E, G and B, which are given by the following relationships:

$$\begin{aligned} \eta_{kk} &= \frac{1}{E}\sigma_{kk} - \frac{\nu}{E}(\sigma_{jl}\sigma_{jl}), j,l \neq k \\ \eta_{jk} &= \frac{1}{2G}\sigma_{jk} \\ B &= -V\frac{dp}{dV} \end{aligned} \tag{2.3}$$

where σ_{jl} is the Kronecker symbol, p is the pressure and V is the volume. E is the Young modulus, B is the bulk modulus, G is the shear modulus and ν is the Poisson ratio.

For the 2 independent elastic constants the following relationships hold true:

$$\begin{aligned} E &= \frac{3C_{11} - 4C_{44}}{C_{11} - C_{44}} C_{44} \\ G &= C_{44} \\ \nu &= \frac{C_{11} - 2C_{44}}{2(C_{11} - C_{44})} = \frac{C_{12}}{C_{11} + C_{12}} \\ B &= C_{11} - \frac{4}{3}C_{44} \end{aligned} \tag{2.4}$$

2.2 The elastodynamics of surface acoustic waves in thin supported films

In the treatment of the propagation of surface acoustic waves (SAWs) on a film substrate system, the boundary effect needs to be taken into account. The presence of a

boundary influences the nature of the wave propagation. The theoretical and practical aspects of the boundary effects on the SAWs propagation in thin supported films will be given in the surface Brillouin cross section study in section 2.3.2. The propagation of surface acoustic waves in opaque thin supported films are mediated by the suface ripple scattering mechanism which can be described by the imaginary component of the Green's function $ImG_{33}(k_{\parallel},\omega)$. This component of the displacement $u_3(0)$ is related to the response function of the force perpendicular to the surface of a film-substrate system. The force applied on the sample is a function of position and time, i.e. F(x,t) is thus defined per unit mass and its harmonic time dependence. In this work, a Green's function approach [61] is used for predicting the experimental SBS spectrum for an isotropic BFO layer (polycrystalline and amorphous) on a cubic silicon substrate. Figure 2.1 shows the coordinate system of a thin layer on a backing substrate. In this consideration the layer and the substrate are considered infinite along their interface. It has been choosen from the coordinate system such that $x_3 = 0$ is at the interface plane, whereas the plane $x_3 = -h$ corresponds to the thin film surface. x_1 is the direction of surface acoustic wave propagation. The sagittal plane is the plane of incidence normal to the thin film surface. The normal modes of vibration from the surface excitations of the waveguide (thin film) can be treated by using the equations of motion and the boundary conditions. The displacement field of the film-substrate media must satisfy the equation of motion for an homogeneous elastic continuum

$$\rho\frac{\partial^2 u_i}{\partial t^2} = C_{ijkl}\frac{\partial^2 u_k}{\partial^2 x_j x_i} \tag{2.5}$$

where C_{ijkl} is the elastic tensor of the respective medium, ρ is the mass density and u_i are the displacements in each part of the waveguide (thin film). Considering a dimensionally infinite system consisting of a substrate and a layer in all directions, plane waves can be suggested solutions to the wave equation (2.5)

$$u_i = Nexp[ik(m_i x_i - vt)] \tag{2.6}$$

where N is the polarization vector of the waves, v is the phase velocity which is measured along the propagation vector k, whose direction cosines are given by (m_1, m_2, m_3). There are no variations in the displacement components of the free surface of the layer and the displacement is normal to the direction of propagation of the surface acoustic waves (SAWs). As $x_3 \longrightarrow \infty$, the amplitude of the waves vanishes and it is characterized as surface acoustic waves. The SAWs can be con-

sidered as a linear sum of plane waves, having the following form:

$$u_i = \sum_{n=1}^{3} \beta_n N_i^{(n)} exp(ikb_3^{(n)} x_3) exp(ik_{\parallel}.x_{\parallel} - vt) \tag{2.7}$$

where $x_{\parallel} = (x_1, x_2)$ and $k_{\parallel} = (\mathrm{k}_1, \mathrm{k}_2)$ describe the coordinate and propagation wave vector in $x_1 - x_2$ plane coordinate system, $\beta_n (n = 1, 2, 3)$ gives the amplitudes of each surface acoustic wave component and b is complex, which represents the variation of the amplitude with depth and phase of surface acoustic waves that are measured with a plane of constant phase i.e. a plane perpendicular to $x_{\parallel}$ [62]. Substituting the plane wave of eqn. (2.6) into the wave eqn. (2.5), gives the characteristic set of equations with three complex roots of $b_3^{(n)}$.

$$| \Gamma_{ij} - \delta_{ij} \rho v^2 | = 0, i, j = 1, 2, 3 \tag{2.8}$$

where $\Gamma_{jk} = m_i m_j C_{ijkl}$ is the Christoffel tensor. $N_i^{(n)}$ the polarization vector can be obtained from the Christoffel equation below:

$$| \Gamma_{ij} - \delta_{ij} \rho v^2 | N_i = 0 \tag{2.9}$$

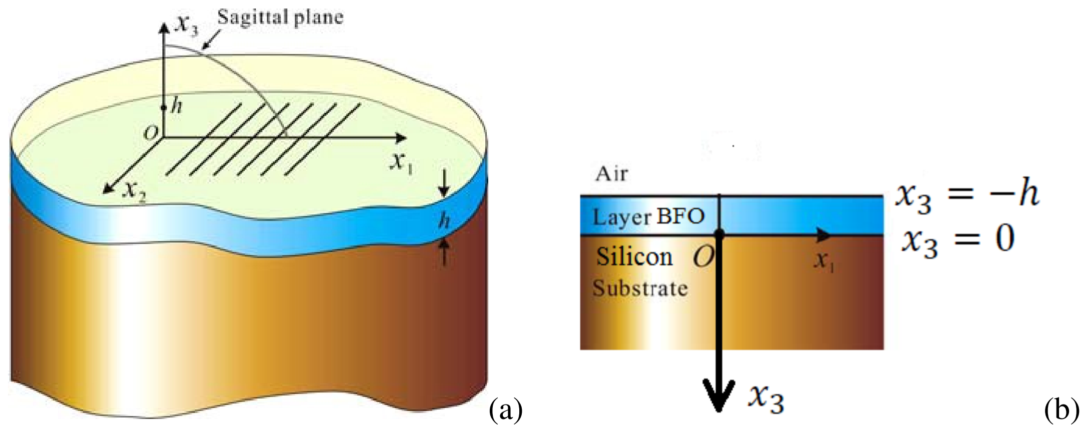

Figure 2.1: Rectangular plane system for the surface acoustic wave propagation in thin films: (a) propagation direction and sagittal plane, (b) sagittal plane coordinates [63]

Substituting eqn. (2.7) into eqn. (2.5), and using a numerical method gives a general matrix that satisfies the boundary conditions at the layer-substrate interface and also on the layer surface. This matrix relates the phase velocity v, the complex amplitude b and the polarization vector N_i. The thin film samples are polycrystalline or amorphous and can be considered as isotropic layers on top of single crystal silicon. The surface acoustic wave propagations along the [110] direction of the layer on the

(001) silicon substrate surface are assumed. The coordinate system for a layer and a substrate are depicted in Figure 2.1 where x_1 is along the [100] direction, x_2 is along the [010] direction and x_3 along the [001] direction and the origin is taken at the free surface. For an isotropic layer, we have two elastic constants (C_{11} and C_{44}). The Christoffel matrix for the layer can be given as [63]

$$\begin{bmatrix} \Gamma_{11}-\rho v^2 & \Gamma_{12} & \Gamma_{13} \\ \Gamma_{12} & \Gamma_{22}-\rho v^2 & \Gamma_{23} \\ \Gamma_{13} & \Gamma_{23} & \Gamma_{33}-\rho v^2 \end{bmatrix} \tag{2.10}$$

where $\Gamma_{11} = C_{11} + b^2 C_{44}$, $\Gamma_{22} = (b^2+1)C_{44}$, $\Gamma_{33} = b^2 C_{11} + C_{44}$, $\Gamma_{12} = \Gamma_{21} = 0$, $\Gamma_{23} = \Gamma_{32} = 0$, $\Gamma_{31} = \Gamma_{13} = b(C_{11} - C_{44})$. Hence the above matrix reduces to

$$\begin{bmatrix} C_{11}+b^2C_{44}-\rho v^2 & 0 & b(C_{11}-C_{44}) \\ 0 & (b^2+1)C_{44}-\rho v^2 & 0 \\ b(C_{11}-C_{44}) & 0 & b^2C_{11}+C_{44}-\rho v^2 \end{bmatrix} \tag{2.11}$$

Equation (2.11) is considered as a sextic equation in b (can be computed from the solution of the wave equations) and the phase velocity v of the acoustic wave can be found from the SBS measurement. For nontrivial solutions, the determinant of the square matrix in equation (2.8) must be zero and for the isotropic system, the associated eigen-vectors and eigen values of the top layers are as follows:

$$\begin{aligned} \rho v_1^2 &= C_{11}(1+b^2),\ \ N_1 = [1,\ 0,\ b]\ \ (sagittal\ \ motion) \\ \rho v_2^2 &= C_{44}(1+b^2),\ \ N_2 = [-b,\ 0,\ 1]\ \ (sagittal\ \ motion) \\ \rho v_3^2 &= C_{44}(1+b^2),\ \ N_3 = [0,\ 1,\ 0]\ \ (transverse\ \ motion) \end{aligned} \tag{2.12}$$

The solutions of the sextic equation in b with the phase velocity v are given as:

I. **for transverse motion in the layer**

$b^{(1)} = +i\sqrt{1-(\frac{v}{\hat{v}_t})^2}$ ································· $\mathbf{N}^{(1)} = [0,\ 1,\ 0]$

$b^{(2)} = -i\sqrt{1-(\frac{v}{\hat{v}_t})^2}$ ································· $\mathbf{N}^{(2)} = [0,\ 1,\ 0]$

II. **for sagittal motion in the layer**

$b^{(5)} = +i\sqrt{1-(\frac{v}{\hat{v}_t})^2}$ ································· $\mathbf{N}^{(5)} = [-b^{(5)},\ 0,\ 1]$

$b^{(6)} = +i\sqrt{1-(\frac{v}{\hat{v}_l})^2}$ ································· $\mathbf{N}^{(6)} = [1,\ 0,\ b^{(6)}]$

$b^{(7)} = -i\sqrt{1-(\frac{v}{\hat{v}t})^2}$ ································· $\mathbf{N}^{(7)} = [-\mathrm{b}^{(7)},\ 0\ ,1]$

$b^{(8)} = -i\sqrt{1-(\frac{v}{\hat{v}_t})^2} \cdots\cdots\cdots\cdots\cdots\cdots \mathbf{N}^{(8)} = [1,\ 0,\ \mathrm{b}^{(8)}]$

III. **for transverse motion in the substrate**

$b^{(a)} = -i\sqrt{1-(\frac{v_{t(l)}}{v})^2} \cdots\cdots\cdots\cdots\cdots\cdots \mathbf{N}^{(\mathrm{a})} = [0,\ 1,\ 0]$

IV. **for sagittal motion in the substrate**

$b^{(c)} = -i\sqrt{[1-(\frac{v}{v_t})^2]} \cdots\cdots\cdots\cdots\cdots\cdots \mathbf{N}^{(\mathrm{c})} = [-b^{(c)},\ 0,\ 1]$

$b^{(d)} = -i\sqrt{[1-(\frac{v}{v_l})^2]} \cdots\cdots\cdots\cdots\cdots\cdots \mathbf{N}^{(\mathrm{d})} = [1,\ 0,\ b^{(d)}]$

$$\begin{aligned}
b^{(5)} &= +i\sqrt{1-(\tfrac{v}{\hat{v}_t})^2} \\
b^{(6)} &= +i\sqrt{1-(\tfrac{v}{\hat{v}_l})^2} \\
b^{(7)} &= -i\sqrt{1-(\tfrac{v}{\hat{v}_t})^2} \\
b^{(8)} &= -i\sqrt{1-(\tfrac{v}{\hat{v}_l})^2} \\
b^{(c)} &= -i\sqrt{1-(\tfrac{v}{v_t})^2} \\
b^{(d)} &= -i\sqrt{1-(\tfrac{v}{v_l})^2}
\end{aligned} \tag{2.13}$$

where the superscripts a, 1, and 2 represent components for the transverse displacements, while the superscripts $5-8$, c and d are the roots of the sagittal-plane displacements [64].
$v_t = \sqrt{(\frac{C_{44}}{\rho})}$ and $\hat{v}_t = \sqrt{(\frac{\hat{C}_{44}}{\hat{\rho}})}$ are the transverse phonon velocities for bulk waves in the layer and substrate respectively, while $v_l = \sqrt{(\frac{C_{11}}{\rho})}$ and $\hat{v}_l = \sqrt{(\frac{\hat{C}_{11}}{\hat{\rho}})}$ are the coresponding bulk longitudinal phonon velocities. In order to obtain the phase velocity of the surface waves we have to substitute $b^{(n)}$ and $N_i^{(n)}$ in the characteristic wave equations of the matrix of eqn. (2.8) by taking into account the boundary condition imposed by the film-substrate interface. The boundary conditions define the continuity of displacements, stresses and strains at the interface and on the top of the layer. Thus, taking into account the boundary conditions we can obtain correct values for the b amplitudes with the effective elastic constants of the BFO films. The boundary conditions for the sagittal-plane displacements produce the following equation:

$$
\begin{pmatrix}
b^{(5)} & -1 & -b^{(5)} & -1 & -b^{(c)} & 1 \\
-1 & -b^{(6)} & -1 & b^{(6)} & 1 & b^{(d)} \\
1-b^{(5)2} & 2b^{(6)} & 1-b^{(5)2} & -2b^{(6)} & -\frac{C_{44}}{\hat{C}_{44}}(1-b^{(c)2}) & -2\frac{C_{44}}{\hat{C}_{44}}b^{(d)} \\
2b^{(5)} & -(1-b^{(5)2}) & -2b^{(5)} & -(1-b^{(5)2}) & -2\frac{C_{44}}{\hat{C}_{44}}b^{(c)} & \frac{C_{44}}{\hat{C}_{44}}(1-b^{(c)2}) \\
(1-b^{(5)2})exp(ikb^{(5)}h) & 2b^{(6)}exp(ikb^{(6)}h) & (1-b^{(5)2})exp(-ikb^{(5)}h) & -2b^{(5)}exp(-ikb^{(6)}h) & 0 & 0 \\
2b^{(5)}exp(ikb^{(5)}h) & -(1-b^{(5)2})exp(ikb^{(6)}h) & -2b^{(5)}exp(-ikb^{(5)}h) & -(1-b^{(5)2})exp(-ikb^{(6)}h) & 0 & 0
\end{pmatrix}
\begin{pmatrix} C_5 \\ C_6 \\ C_7 \\ C_8 \\ C_c \\ C_d \end{pmatrix} = 0 \tag{2.14}
$$

For a given crystal symmetry and configurations of both the substrate and the layer, we can see so far that the amplitude b is a function of the phase velocity, v. Upon substituting eqn. (2.13) into eqn. (2.14) and equating the determinant of the matrix to zero, an expression of the phase velocity v, as a function of $k_{\|}h$ (the dimensionless product of the probing wavenumber and the film thickness) can be defined. This relation $v = v(k_{\|}h)$ is called the dispersion relation. For a given $k_{\|}h$, there are many values of the acoustic wave speed v. The lowest value characterizes a Rayleigh surface acoustic mode, the next higher values represent the higher order frequency peaks called the Sezawa modes. A numerical approach to eqn. (2.14) is necessary to obtain the phase velocity v of the surface acoustic wave. The solution to eqn. (2.14) depends on the elastic configuration of the layer and substrate. A number of cases of the film-substrate systems should be considered to determine the relationships between the phase velocity of the surface acoustic waves v and $k_{\|}h$. There are two cases for the film-substrate system namely;

- Slow on fast system (the layer loads the substrate) and fast on slow system (the layer stiffens the substrate). A slow on fast film-substrate configuration is observed if the transverse bulk velocity of the substrate is greater than that of the thin film. In addition, if the mass density of the film is greater than the substrate, then this can create a slow on fast system [65]. In this case the Rayleigh wave velocity of the layer is reduced by the existence of the substrate. For the slow on fast system, the dispersion curve of the Rayleigh wave starts with negative gradient at the Rayleigh velocity of the substrate, for $k_{\|}h = 0$. As $k_{\|}h$ increases the phase velocities continue to decrease. All the higher order Sezawa waves have a lower frequency cutoff at the shear velocity of the substrate. These phase velocities have also a trend of decreasing with increasing $k_{\|}h$ until a high frequency asymptote at the layer longitudinal velocity. In this work we have the BFO film-silicon substrate system, which is an example of a slow on fast system and the dispersion curves of the different modes of propagation of the guided waves are depicted in section 2.3.2.

- When the transverse bulk wave velocity of the film is greater than the substrate then the system is said to be a fast on slow system and the thin film deposited always increases the SAWs above the Rayleigh velocity of the substrate. For the fast on slow situation, the dispersion curve of v vs. $k_{\|}h$ starts at $k_{\|}h = 0$ at the substrate Rayleigh velocity and increases until the substrate longitudinal velocity is attained at a particular value of $k_{\|}h$. But for very large values of $k_{\|}h$ the guided modes of propagation do not exist. This may be due

to the small effect of the substrate at large $k_{\|}h$, i.e. the substrate has negligible effect on the guided modes propagating in the film at large $k_{\|}h$. In this region the mode velocities attain either the film's Rayleigh wave velocity or the intrinsic transverse velocity of the film [66]. The mode velocities of the films between these limiting values are derived by the elastic properties and densities of the film and substrate.

2.3 Surface Brillouin Scattering in thin supported films

Surface Brillouin scattering spectroscopy is a complex optical technique that helps us measure the inelastic light scattered from a thin film-substrate system.

2.3.1 Basic principles of Surface Brillouin Scattering (SBS)

The surface Brillouin scattering (SBS) spectroscopic technique has been a standard tool for a considerable time for the studies of wave propagation in bulk materials, thin films and multilayer assemblies, to exploit the mechanical (elastic constants) and surface acoustic properties of the material under investigation [34]. The technique is based on the principle of inelastic coherent interaction between acoustic waves at hypersonic frequencies generated by thermally excited acoustic phonons of a sample and photons of electromagnetic waves (laser). The surface acoustic phonon wave vectors satisfy a quasi-momentum conservation principle that can be determined from the kinematics of the scattering geometry (which lies in the center of the Brillouin zone). For a backscattering geometry (angle of incidence equals angle of scattering), the Brillouin frequency shift ω_{SAW} of a surface peak is simply related to the acoustic velocity, wavelength of the beam and angle of incidence θ_i of the laser. The scattered beam from the sample contains shifted frequencies (ω_{SAW}) and its measurement in the frequency domain is enabled by a high resolution and high contrast multipass $(3+3)$ tandem Fabry–Pérot interferometer [67]. From the quantum perspective, the interactions between phonons and photons results in the creation and annihilation of phonons. This is represented in the Brillouin spectrum as doublets in the sidebands defined as the Stokes and anti-Stokes components, respectively. Brillouin scattering studies have been applied to our BFO thin films. The films could support multiple propagating modes because of the films' intrinsic acoustic properties, densities of the films that make up the waveguides and residual stresses in them. Various guided and localized acoustic modes (frequencies) have been observed from the experimental spectra including Rayleigh and Sezawa

waves. Numerical fitting of the measured acoustic surface wave velocities enabled the extraction of the elastic constants of the films.

In Brillouin scattering the acoustic excitations include ripple and elasto-optic scattering mechanisms. The ripple mechanism is a surface-type phenomenon and a substrate sub-surface interaction [68]. Each of these scattering mechanisms requires specific experimental configurations to obtain their contributions in the measurement of surface acoustic phonons in the spectrum. To observe contributions of the surface acoustic phonons from the SBS measurement of the ripple mechanism, the use of s-s polarization (the electric field of the laser normal to the plane of incidence) or p-p polarization (the electric field lies in the plane of incidence) configurations in the scattering geometry is important. These polarization configurations eliminate the effect of the surface spin waves arising from magnetic samples. Hence, in this study we do not consider the elasto-optic scattering mechanisms which require (s-p) and (p-s) polarization configurations, since the samples are opaque.

The surface acoustic phonon excitations have a wavelength of the order of submicrometer dimensions, which is the same order as optical wavelengths. Thus, this consideration enables the use of the continuum model of classical elastodynamics [69] for the treatment of macroscopic elasticity. The elastodynamic analysis of surface acoustic phonon excitations is given in section 2.2.

2.3.2 SBS cross-section

The surface acoustic waves (the moving phonons, the sound waves, the mechanical waves) scatter light by the surface ripple and elasto-optic mechanisms. If the incident light is scattered from the dynamic acoustic deformation (corrugation of a surface created by a thermodynamic equilibrium moving phonon with a small amplitude present in the sample) then it contributes to the ripple scattering cross-section in the surface Brillouin spectra. Otherwise, a bulk elasto-optic mechanism operates in which the interaction of incident and scattered light occurs by way of the acoustic modulation of the sample dielectric constant. Our thin film-substrate system is opaque and hence the scattering is dominantly mediated by the surface ripple scattering mechanism. For this kind of mechanism, the kinematic condition or the wave vector conservation eqn. (2.24) and (2.26) of the scattered light conserves only the wave vector component parallel to the surface. The scattering cross-section for the ripple mechanism with frequency ω and scattering wave vector $\vec{k}_{\parallel}$ is related to the power spectrum $<\mid u_3(k_{\parallel}, x_3 = 0; \omega) \mid^2>$ of the normal fluctuations on the surface profile.

The power spectrum of the normal displacements $u_3(0)$ of the surface of the thin film is proportional to the imaginary component of the surface Green's function given by [70]

$$<|\, u_3(k_{\shortparallel}, x_3 = 0; \omega)\,|^2> \propto \frac{k_B T}{\pi\omega} Im\{G_{33}(k_{\shortparallel}, x_3 = 0; \omega)\} \tag{2.15}$$

where G_{33} is the (x_3, x_3) component of the Fourier (frequency and wave vector) domain surface elastodynamic Green's function tensor $G_{ij}(x,t)$. This tensor is calculated using the force and displacement at the outer free surface of the layer. The simulation of the G_{33} components of the Green's function at $x_3 = -h$ of the sagittal coordinates of the free surface of the film gives the scattered mode intensities for a given $k_{\|}h$. Figure 2.2 shows the simulated dispersion curves of the BFO thin film.

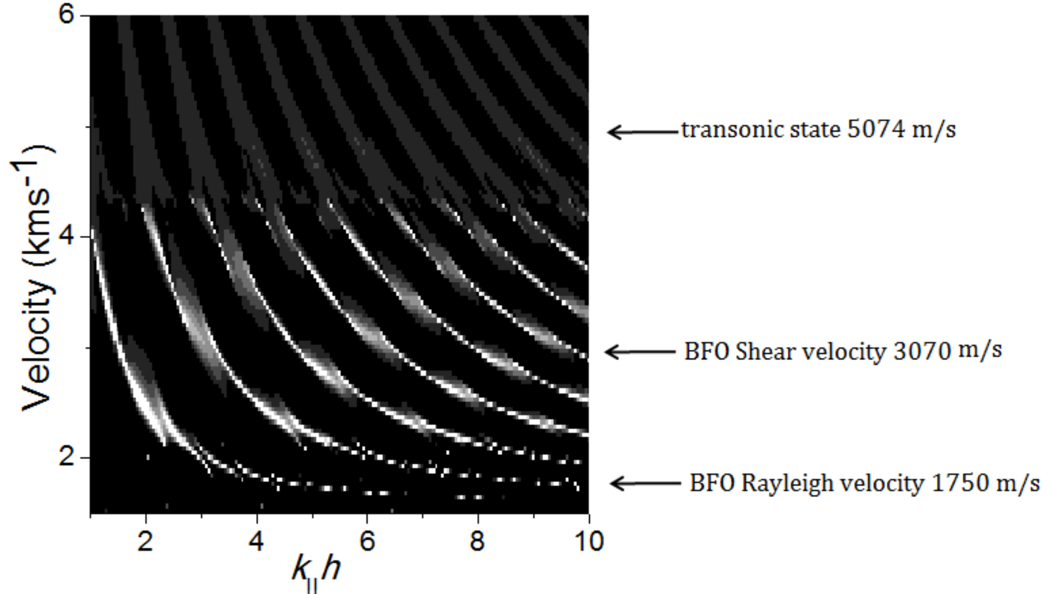

Figure 2.2: Examples of velocity dispersion curves of the BFO thin films, calculated using the elastodynamic Green's function using the G_{33} component for the $BiFeO_3$/Si film-substrate system of the dispersion modes of the guided waves for various $k_{\|}h$. The figure depicts the BFO layer on (001) silicon substrate, an example of a slow on fast system (loading case). BFO: $v_l = (4965-5535)\ m/s$, $v_t = (1720-3070)\ m/s$ and $v_R = 1750\ m/s$; Silicon: $v_l = 8344\ m/s$, $v_t = (5074-5656)$ m/s and $v_R = 5074\ m/s$. The Rayleigh surface acoustic wave (RSAW), Sezawa waves (SWs, 1st, 2nd and 3rd etc.), and pseudo-Sezawa wave region, which lies between the the transonic state and shear bulk wave velocity of the substrate, are shown. Sharp resonances appear in the region beyond the shear bulk wave velocity of the substrate.

From eqn (2.8), all six roots (real and complex conjugate pairs) are used in the calculation of the film displacement, whereas only the three roots of the positive

imaginary parts are used for the calculation of the substrate displacement. The displacement field in the layer is given as a linear combination of terms having the phase velocity v, [71]:

$$\tilde{u}_j = [\sum_m \widetilde{A}_n N_i^{(n)} exp(ik\widetilde{\beta}^{(n)} x_3)] exp[ik(x_1 - vt)], n = 1,2,...6 \tag{2.16}$$

and in the substrate as:

$$u_j = [\sum_m A_m N_i^{(m)} exp(ik\beta^{(m)} x_3)] exp[ik(x_1 - vt)], m = 1,3,5 \tag{2.17}$$

The coefficients A_m with even subscripts m are omitted because they are not related to finite solutions. $N_i^{(n)}$and $N_i^{(m)}$are complex eigenvectors related to eqn. (2.9) for the film and for the substrate and their eigenvalues are $\widetilde{\rho} v^2$and ρv^2 respectively. $\widetilde{A}_n$ and A_m are the weighting factors for the linear combination of waves in the film, eqn. (2.16) and the substrate, eqn. (2.17). The weighting factors can be determined from the boundary conditions.

The displacement and stress fields must be continous at the film-substrate interface and satisfy the boundary conditions of the film-substrate system. There are three boundary conditions:

- continuity of the stress at the interface, i.e. $\widetilde{\sigma}_{j3}(k_{\shortparallel}, x_3 = \widetilde{0}, \omega) = \sigma_{j3}(k_{\shortparallel}, x_3 = 0, \omega)$,
- continuity of the displacement field at the interface, i.e. $\widetilde{u}_i(k_{\shortparallel}, x_3 = \widetilde{0}, \omega) = u_i(k_{\shortparallel}, x_3 = 0, \omega)$, and
- the stress is free at the $x_3 = -h$, at the free surface of the film i.e. $\widetilde{\sigma}_{l3}(k_{\shortparallel}, x_3 = -h, \omega) = 0$.

These boundary conditions for the strain and stress fields are calculated for the films and the substrate using 9 equations with 9 unknowns. The solution to these equations is a dispersion relation for the guided acoustic waves polarized in the $x_1 - x_3$ plane. Applying the stress at the free surface $x_3 = -h$ leads to three linear equations for the partial wave amplitudes of $A^{(n)}$[72], [62].

$$\sum_{n=1}^{6} B_l^{(n)} A^{(n)} = \frac{i\delta_{3l}}{\omega}, l = 1,2,3 \tag{2.18}$$

Applying the continuity of the stress at the interface gives three equations for the

partial wave amplitudes

$$\sum_{n=1}^{6} B_l^{(n)} A^{(n)} = 0, l = 4,5,6 \tag{2.19}$$

The continuity of the displacement field at the interface results in three equations with the partial wave amplitudes given as:

$$\sum_{n=1}^{6} B_l^{(n)} A^{(n)} = 0, l = 7,8,9 \tag{2.20}$$

Combining eqn. (2.18), (2.19) and (2.20) gives a system of nine linear equations in nine unknown $A^{(n)}$ and it can be written in matrix form (B);

$$A^{(n)} = \frac{i}{\omega}(B^{-1})^{(n)} = \frac{i}{\omega}\frac{adj(B)^{(n)}}{det \mid B \mid} \tag{2.21}$$

where $adj(B)$ denotes the matrix adjoint of B.
By replacing these results for $A^{(n)}$ of eqn.(2.21) by the film displacement, we can obtain the displacement Green's function at the free surface of a the layer is

$$G_{33}(k_{\shortparallel}, x_3 = -h, \omega) = \sum_{n=1}^{6} \frac{i}{\omega}(B^{-1})_3^{(n)} N_3^{(n)} exp(-ik_3^{(n)} h) \tag{2.22}$$

Therefore, the intensity of the Brillouin scattering from the free surface of a supported layer is

$$I(\omega) \propto Im\left\{\sum_{n=1}^{6} \frac{i}{\omega}(B^{-1})_3^{(n)} N_3^{(n)} exp(-ik_3^{(n)} h)\right\} \tag{2.23}$$

2.3.3 Kinematics of SBS

The kinematics of surface Brillouin scattering provides an intuitive picture of the scattering interactions between photons and phonons. Incident light with a wave vector $\overrightarrow{k}_\circ$ and frequency ω_i is inelastically scattered by natural corrugations in the thin film-substrate system. The scattering mechanism by thermally equilibrium moving phonons (acoustic phonons or elastic waves) present in the sample having a wave vector $\vec{k}_\parallel$ and frequency $\omega(k)$ is shown in Figure 2.3. The scattered light has wave vector $\overrightarrow{k}_s$ and frequency ω_s. The conservation of momentum and energy in this scattering processes leads to the expression:

$$\overrightarrow{k_s} - \overrightarrow{k_o} = \pm \overrightarrow{k_{\parallel}} \tag{2.24}$$

$$\omega_s - \omega_i = \pm \omega(k) \tag{2.25}$$

where the plus sign refers to anti-Stokes events associated with the absorption of a phonon in the scattering process, while the minus sign corresponds to the Stokes events in which a phonon is created. The phonon frequencies probed in materials by Brillouin scattering are in the hypersonic regime $(10^9\ Hz < \omega(k) < 10^{12}\ Hz)$.

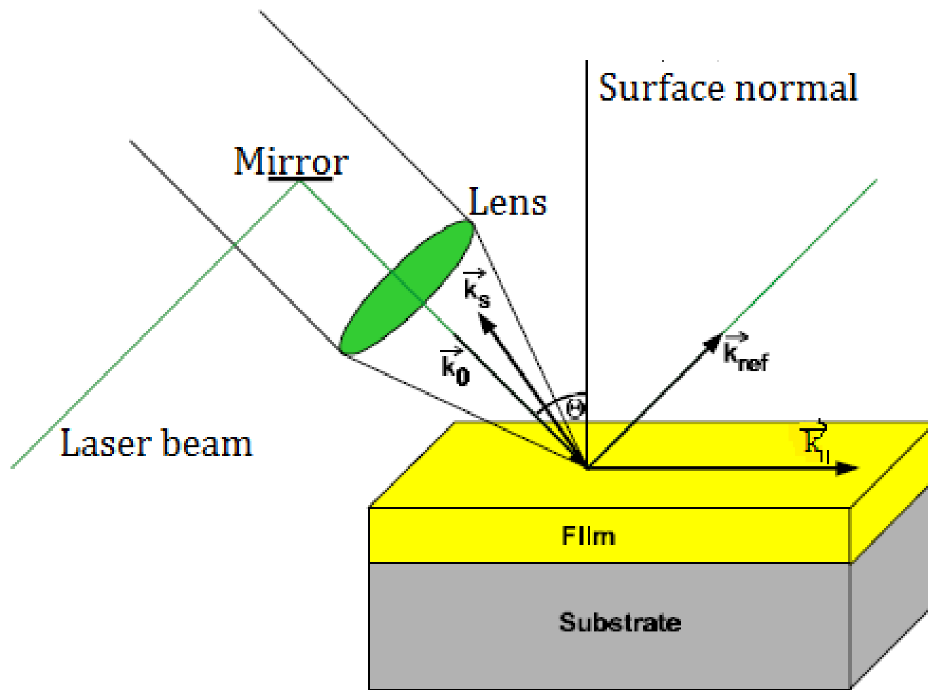

Figure 2.3: Diagram of inelastic light scattering processes and backscattering geometry [73]

For an opaque film, the scattering for SAW's are localized in a region close to the surface; and hence the conservation of momentum only applies to the components parallel to the surface. From conservation of momentum the surface phonon wave vectors (the probing vector) parallel to the surface is given as:

$$\overrightarrow{k_{\parallel}} = 2k_i sin\theta = \frac{4\pi}{\lambda_i} sin\theta \tag{2.26}$$

where θ is the angle of the incident photon wave vector. From conservation of total energy, the frequency shifts $(\omega_s - \omega_i = \Delta f)$ of the scattered light is the frequency shift of the surface acoustic phonons. Since the wave vector (the probe wave vector)

parallel to the surface $(10^5\ cm^{-1})$ is less than the dimensions of the Brillouin zone $(10^8\ cm^{-1})$ in the wave vector space, every information about the phonons in the center of the Brillouin zone can be linearly given in terms of the phase velocity of the surface acoustic waves i.e. $|\overrightarrow{k_{\parallel}}| = v\triangle f$, thus $v_{SAW} = \frac{\lambda_i \triangle f}{2sin\theta}$.

2.4 Thin film growth

Deposition of thin films of various materials such as metals, ceramics and plastics onto a surface (substrate) can be achieved through different deposition techniques. Typical deposition processes are categorized in a broad sense as physical vapour deposition (PVD) and chemical vapour deposition (CVD) processes. The PVD processes include, vacuum evaporation, pulsed laser deposition (PLD), molecular beam epitaxy (MBE) and sputtering. RF-magnetron sputtering was used to fabricate thin films using the concepts of the Thornton model.

Sputtering is the process of ejecting the target atoms upon collision with highly energetic ions, typically inert gas ions such as argon (Ar^+). This collision results in a momentum transfer from Ar^+ through the knock-off effect. The ad-atoms are later deposited as thin films on the substrate. Sputter deposition methods are used to generate and maintain a desired plasma and to establish a bias or electric field for the acceleration of ions to the electrode or target being bombarded [74]. Several processes occur upon bombardment of the target by Ar^+. These may consist of:

- ion reflection at the target surface, that might be neutralized in the process,
- ion implantation, consisting of a cascade of atomic collisions in the target that would also cause sputtering of target atoms,
- the ion may be permanently embedded in the target,
- emission of secondary electrons,
- emission of X-rays and photons.

The energy of the ions in the plasma is heavily dependent on the cathode potential (V_{cat}) and plasma potential (V_p) parameters. The difference between the cathode potential and the plasma potential is defined as the cathode fall, and its physical meaning is the energy (E) gained by the ions when they impinge on the target material. This is also the same energy attained by secondary electrons when they cross the cathode sheath and enter the main part of the plasma as shown in the equation (2.27)

$$E = q(V_p - V_{cat}) \tag{2.27}$$

where q is the electronic charge. In addition, the reflected neutralized ions are important as they could possess sufficient energy to reach the substrate and cause energetic particle bombardment on the growing film. It is evident that before the sputtered species reach the substrate they experience collisions and some are scattered in the process. Most of the time scattering reduces the kinetic energy of the sputtered species. This reduction in kinetic energy is accompanied by temperature reduction in a process that is referred to as thermalization. The sputter pressures and target to substrate distance are parameters that affect the thermalization process. At a lower pressure, the ad-atoms arrive at the substrate with considerably more energy. The $\frac{\lambda}{D}$ ratio determines the mechanisms that affects the sputtering process. λ is the mean free path, which scales inversely with pressure, D is the target-substrate distance. A diagram illustrating the sputtering processes is shown in Fig. 2.4.

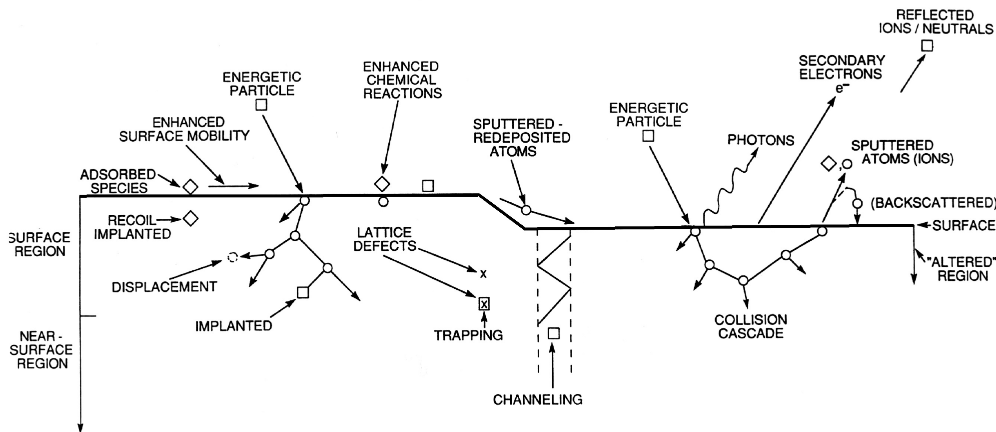

Figure 2.4: The process of sputtering [75]

The process of generating a plasma involves first pumping down the sputter chamber to an appropriate base pressure (~2×10^{-6} $mbar$). Next, a sputter gas (usually Ar) is introduced into the chamber and creates a low working pressure (~2×10^{-3} $mbar$). Sputtering occurs when a negative bias voltage is applied to the target material to cause a plasma or glow discharge [76]. The plasma consists of charged species such as ions and electrons, as well as neutral species. A schematic diagram of the unbalanced magnetron sputtering setup and its plasma components is depicted in Fig. 2.5.

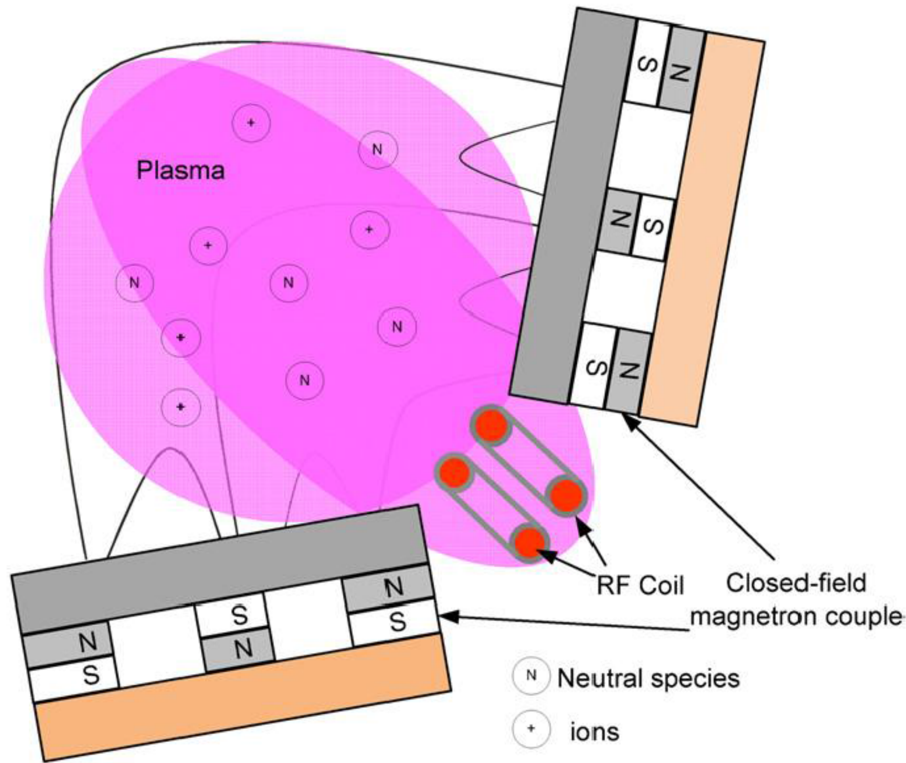

Figure 2.5: Schematic diagram of unbalanced magnetron sputtering setup [77]

Ions which impinge on the cathode surface cause atoms to be emitted through a cascade process, as indicated in Fig. 2.4. Among the numerous ion/surface interactions is the generation of secondary electrons. These electrons are accelerated into the plasma, causing further ionising collisions that help sustain the plasma process. However, the majority of the electrons produced will not participate in the collision processes but instead escape to the anode, making the process inefficient. The required gas pressure and applied voltage ranges needed for the parallel plate glow discharge to be maintained are around 3 -300 *Pa* and 1000 -2000 *V*, respectively. In order to improve the efficiency of the sputtering process, it is necessary to increase the number of collisions made by each secondary electron before it reaches the anode. This can be achieved by superimposing a magnet on the cathode, whose magnetic field confines the electrons in orbits close to the cathode. The electrons experience a Lorentz and electric force due to the fields:

$$\overrightarrow{F} = -e(\overrightarrow{E} + \overrightarrow{V} \times \overrightarrow{B}) \tag{2.28}$$

The component of the magnetic field that is parallel to the target causes the electrons to return towards the target in a cycloidal motion. For the insulating target, an RF voltage is applied to the target to effectively self-bias the insulating target to a neg-

ative potential, so that it is sputtered by positive ion bombardment. The uniformity of the ion flux throughout the plasma and the target and its limited area leads to a smaller ion current . On the other hand, the electron current is only determined by the plasma potential relative to the surface and is independent of surface area. As a result, the target receives a smaller ion current than electron current and is driven to a negative potential. At low frequencies (< 50 *kHz*), the mobility of the electrons and ions is greatly enhanced, thus rendering the electron and ion currents more sensitive to the switching of the polarity of the electrodes. At greater frequencies two things become apparent: first, the power can be transfered from the cathode through the insulating target by capacitive coupling. Moreover, the electrons oscillating in the glow region become energetic enough to cause ionizing collisions themselves, and hence reduce the need to maintain the secondary electrons in the cathode region. The standard RF frequency reserved for plasma processing is 13.56 *MHz*. Therefore, magnetron sputtering in the RF power mode was used in this study to fabricate BFO thin films from an insulating target.

2.4.1 Ferroelectric (BFO) thin film growth

The thin film growth process is a self-organizing structural evolution that takes place by an atom-by-atom rearrangement at temperatures far from thermodynamic equilibrium. This allows the controlled synthesis of metastable phases and artificial structures, such as multilayers and nanocomposites. The following subsections describe in detail the process of structural evolution in *in-situ* thin film growth by sputtering.

2.4.1.1 Film nucleation and growth

Thin solid films are fabricated from the vapor phase on a substrate by a process consisting of nucleation and growth of individual islands (or clusters). At the first stage, small nuclei are created from individual atoms or molecules. Then, as time progresses, these islands grow to coalesce and form a continuous film. Enhanced coalescence increases film thickness [78]. The morphology and structure of the thin film depend on the size, shape, area density and growth rate of the individual islands. The main stages during thin film nucleation and growth on a substrate are schematically illustrated in Fig. 2.6. Atoms originate from the vapor phase (the glow discharge) and are adsorbed on the surface. The incident rate at which the atoms strike the substrate surface is mostly dependent on the deposition parameters. The diffusion of the adsorbed atoms on the surface strongly depends on the

substrate temperature. Adsorbed atoms either re-evaporate or form clusters, which consequently develop into large clusters. Clusters greater than a critical size are stable (critical nucleus) and therefore proceed to form thin films.

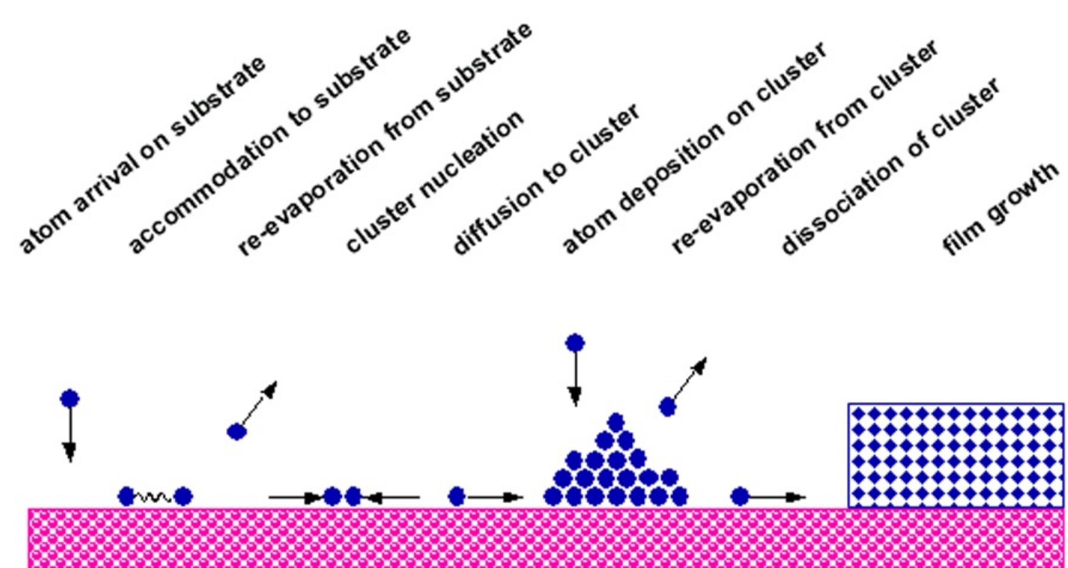

Figure 2.6: Processes in the nucleation and growth of thin films on a substrate [78]

Single atoms may diffuse across the substrate to be part of the stable clusters, or else they may impinge directly on the grown clusters and become incorporated in the clusters.

Figure 2.7 illustrates the steps to film growth spanning from the formation of separate islands, their coalescence and thickening to the formation of polycrystalline films with diverse grain sizes. The subsequent sections highlight each growth step in detail.

2.4.1.2 Island coalescence

Islands that reach a certain critical size start to impinge on each other. As the two islands get into contact, the driving force for island coalescence leads to the formation of a grain boundary to reduce the free surface energy of the two islands (Fig. 2.7[a]). Thus the islands commence to coalesce and form a continuous film. If the diffusivity is relatively low, the attraction between the islands is often accompanied by substantial straining of the developing film, which accounts for the intrinsic tensile stress that is often seen during the early stages of thin film growth [79]. If there is an energy difference between the two impinging islands that may be due to different size and/or different interfacial energies, then a driving force arises for the

growth of one island at the expense of the other. High diffusivity caused by grain boundary motion leads to the elimination of the smaller islands. However, low diffusivity is characterized by a static grain boundary, leading to relatively small grain sizes upon coalescence (Fig.2.7[b]). Since the energy of the individual islands depend on size and orientation, structural evolution during coalescence can affect both the developing grain size distribution and the orientation distribution [80].

2.4.1.3 Thickening

When an amorphous or a polycrystalline film is fully coalesced and a continuous film is produced, then the film thickness increases by continued deposition. In the thickening process, the structure evolves in different ways depending on the actual deposition conditions and the ad-atom mobility in the system, i.e. the ability for atomic diffusion on the surface, in the grain boundaries and in the interior of the grains [81]. New atoms arriving at the film surface may either nucleate new grains on top of the existing grains, or produce "local epitaxial growth", i.e, by joining the already formed grain, which provides a template with low-energy sites for additional (growth-induced) grain growth. The latter growth mode formed by nucleation of new grains mediated by impurities is thus predominantly equiaxed (Fig. 2.7 [d]). In the process of thickening, the growth of some grains may be prioritized due to interface and strain energy minimization, resulting in what is called a competitive growth [see Fig. 2.7 (c)] [81], [82].

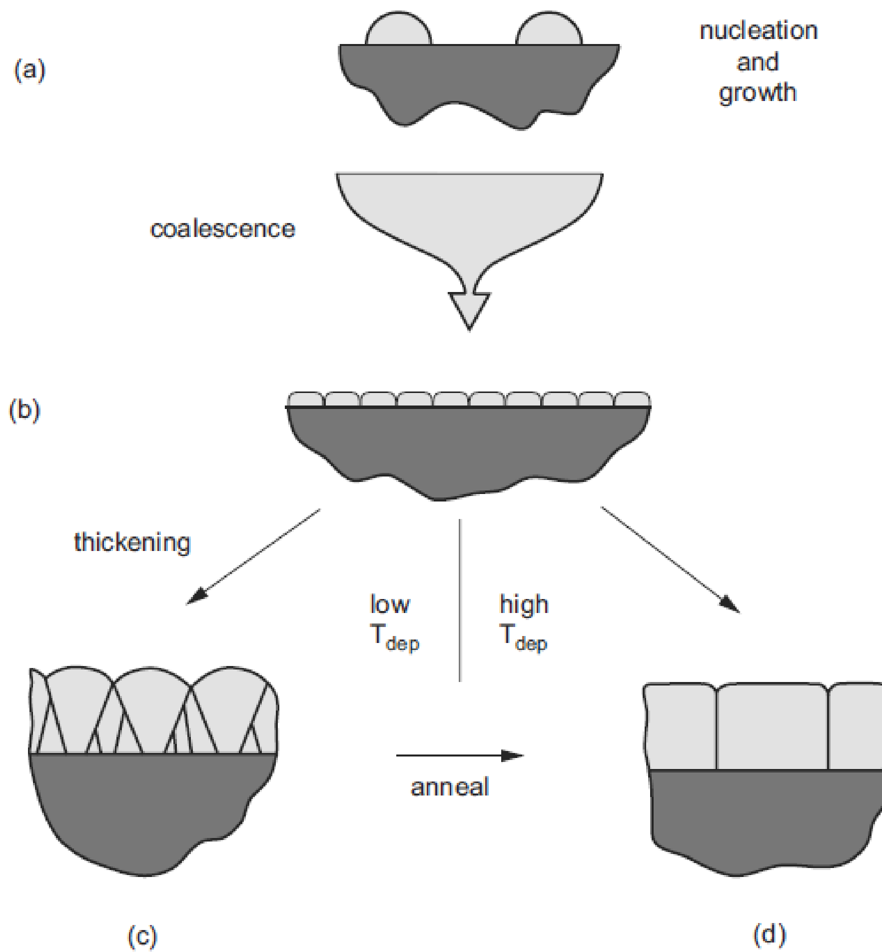

Figure 2.7: Grain structure evolution during deposition of polycrystalline thin film. Island formation and growth leads to impingement of islands to form grain boundaries. The development of grain structure during subsequent film growth is determined largely by surface mobility of ad-atoms relative to the deposition rate, and by the substrate temperature relative to the melting temperature of the film material. [81].

If the strain energy increases with film thickness, a continuous change in texture as a function of film thickness can be the result. Moreover, selective growth during sputter deposition is due to the fact that resputtering is more pronounced for some crystallographic orientations than others [83].

2.4.1.4 Grain growth

Grain coarsening occuring through motion of grain boundaries is normally referred to as grain growth, (see Fig.2.8 [84]). The grain boundary migration leads to shrinkage and elimination of smaller grains. Grain growth also decreases the interfacial energy and as a result the total energy of polycrystalline materials. A review of the

mechanisms and models of grain growth in polycrystalline thin films has been given by Thompson [85]. At high substrate temperatures, grain growth is facilitated by a reduction in the total grain boundary area. This process reduces the total free energy associated with the grain boundaries. The driving force pushes the boundaries to move towards its center of curvature.

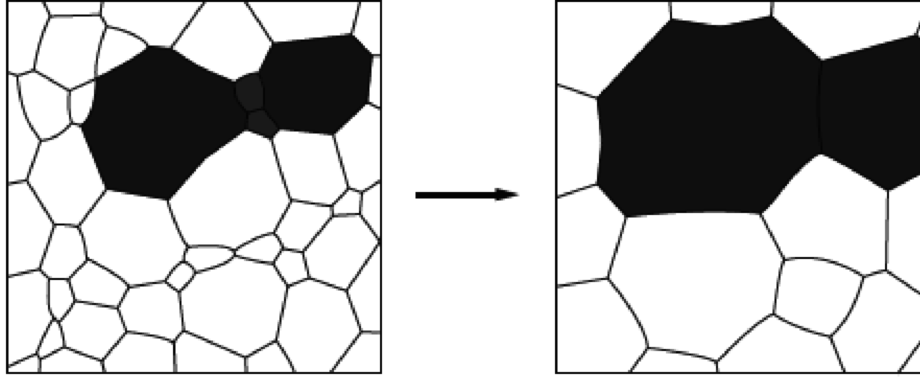

Figure 2.8: Grain growth in a two dimensional polycrystalline thin films [84]

Assuming the velocity of grain boundary migration (or grain growth rate) dD/dt is proportional to the driving force, $dD/dt = K.\gamma_{gb}/r$, where K is a rate constant ($\sim$mobility), γ_{gb} is the grain boundary energy and r is the radius of curvature of the grain (proportional to the grain size). The grain size D at time t and constant temperature T can be expressed as

$$D^2 - D_\circ^2 = K(T)t \tag{2.29}$$

where D_0 is the initial mean grain size, and $K(T)$ is a thermally activated rate constant. The rate constant is equivalent to the grain boundary mobility and can be expressed in an Arrhenius-type equation:

$$K = K_\circ exp(\frac{-Q}{k_B T}) \tag{2.30}$$

where $K_\circ$ is a pre-exponential constant, k_B is the Boltzmann's constant, and Q is the activation energy for the rate limiting atomic process needed for grain boundary migration. Many factors contribute to the grain-growth behavior. For example, in the formation of thin films, the interfacial energies related with the film-surface interface can play an important role. Moreover, impurity particles, pores or defects (e.g. dislocations, vacancies, stacking faults) can exert a drag or pinning force, which restricts the migration of grain boundaries. The models of eqn. (2.29) and eqn. (2.30) do not take account of the pinning forces. A model proposed by Bruke

[86] considers grain growth with due regard to pinning forces, where a limiting grain size is introduced. This model leads to the equation:

$$\frac{D_\circ - D}{D_m} + ln(\frac{D_m - D_\circ}{D_m - D}) = K_2 t \tag{2.31}$$

where D_m is the maximum grain size due to the pinning forces, and K_2 is an Arrhenius-type rate constant. In addition to drag or pinning forces, impedance to grain growth results from insufficient driving force due to structural factors, such as low-energy grain boundary structures, equiaxed grain morphology, narrow grain-size distribution, and flat grain boundary configurations [87]. In such a case, the growth of one type of grain does not occur at the expense of the other, leading to a metastable structure.

2.4.1.5 Surface melting

This phenomenon describes the presence of a stabilized quasi-liquid film on crystalline surfaces below the crystal melting point (T_m) [88].

2.4.2 Structural Zone Model (SZM)

The mobility of the ad-atoms during growth is dependent on the energy given to the atoms and this has an effect on the microstructure of the thin film. The energy given to the atom can be supplied by different mechanisms such as: thermal effect (substrate temperature), ionic bombardment and chemical reactions at the substrate. Thin films produced by these mechanisms can be explained by the Structural Zone Model (SZM). Irrespective of the type of material, the SZM can illustrate the nature of the morphology and microstructure of the films as a function of the ad-atom species or energy. The parameters that are used in this model for determining the microstructure of the films are;

- The substrate temperature,
- The working gas pressure,
- The bias voltage applied to the target and its polarity,
- The thermal characterstics of the target.

This model is based on the substrate temperature (T_s) which affects predominantly the film surface structure, based on the ratio $\left(\frac{T_s}{T_m}\right)$. The film microstructure is thus

divided into 3 main structural zones with boundary temperatures; $T_1 = 0.3T_m$ and $T_2 = 0.5T_m$, where $T_m(K)$ is the melting point of the target material . At low temperatures ($T < T_1$, zone 1), the surface diffusion of ad- atoms is too weak. This leads to the formation of columnar structures. Films produced at higher temperatures ($T_1 < T < T_2$, zone 2) show large columns. In this case the surface diffusion of ad- atoms is enough to engender surface crystallizations of the film. The films deposited at ($T > T_2$, zone 3) result in big grains with flat and faceted faces [89].

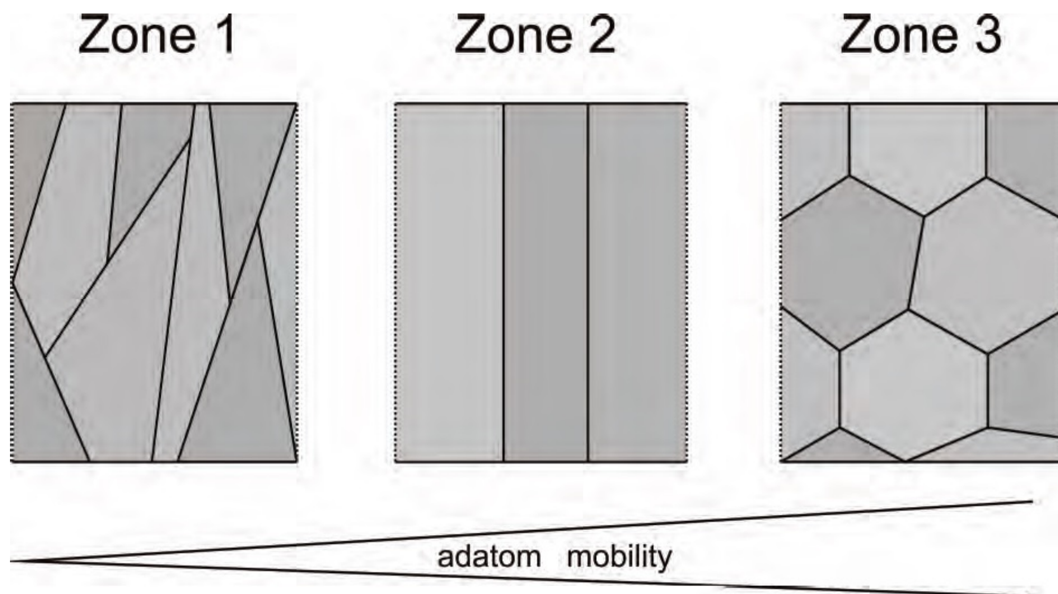

Figure 2.9: Typology of the structure zone models [90]

An increase in temperature produces a similar effect on the adsorption and mobility of the atoms [91]. The bias voltage also influences the mechanical properties of thin films by increasing the deformation of the lattice. This causes high residual stress and low adherence between the substrate and the film [92]. The power supplied to the target and the gas flows also affect the microstructure.

The nucleation and growth of thin films are entirely dependent on the thermodynamics and kinetics of the deposition and the substrate surface interaction between the substrate material and the ad-atoms [93]. The three basic modes of thin film growth are explicitly described by the following models and a schematic diagram of these growth modes is given in Figure 2.10:

- Frank-van der Merwe mode,
- Volmer-Weber mode and
- Stranski-Krastanov mode.

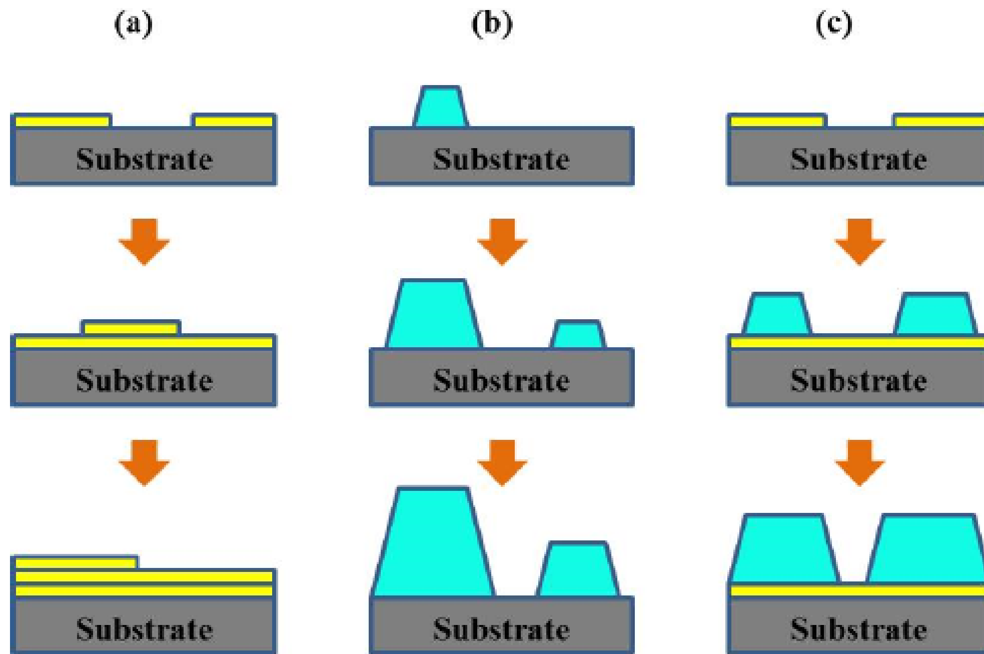

Figure 2.10: Growth modes: a -Frank-van der Merwe (layer by layer growth) b-Volmer-Weber (island growth mode) and c-Stranski-Krastanov (layer plus island growth) [93].

In the Frank-van der Merwe mode, the growth of a layer occurs by the incoming atoms and molecules which have less attractions among them than to the substrate. This growth mode is ideal for epitaxial growth. In the Volmer-Weber mode, the bonds among the incoming atoms are greater than with the substrate and hence the island (Volmer-Weber) growth results in 3 dimensional nuclei. Moreover, it is possible to have a combination of these modes of growth and this is demonstrated when the energy associated with consecutive layers changes. This is an example of a mixed mode and is known as the Stranski-Krastanov (S-K) mode.

2.5 RF Magnetron Sputtering of $BiFeO_3$ thin films

The correlation between the deposition parameters and the properties of $BiFeO_3$ films is presented below.

2.5.1 Substrate temperature

The mobility of ad-atoms and clusters on the substrate increases with increasing substrate temperature. Thus, the substrate temperature influences the microstructure and morphology of the BFO films. The nucleation of the thin film is determined by

the substrate temperature and the deposition rate, $\dot{R}$. Subsequently, the chemical free energy change per unit volume, $\triangle G_v$, is defined by the equation [83]:

$$\triangle G_v = \frac{-KT}{\Omega} ln \frac{\dot{R}}{\dot{R_e}} \tag{2.32}$$

where $\dot{R_e}$ is the equilibrium evaporation rate from the film nucleus at the substrate temperature T, and Ω is the atomic volume.

Assuming an inert substrate, i.e. γ_{vf}=γ_{fs}, where the interfacial tensions of vapor-film (γ_{vf}) and film-substrate (γ_{fs}) are equal, and differentiating the equation of the critical nucleus size r^* [94]

$$r^* = \frac{-2(a_1\gamma_{vf} + a_2\gamma_{fs} - a_2\gamma_{sv})}{3a_3\Delta G_v} \tag{2.33}$$

where a_1 , a_2 and a_3 are the geometric constants of the nucleus. results in

$$\left(\frac{dr^*}{dT} = \frac{2}{3} \left| \frac{\gamma_{vf}(\partial \triangle G_v/\partial T) - (a_1 + a_2)\triangle G_v(\partial \gamma_{vf}/\partial T)}{a_3 \triangle G_v^2} \right| \right) \tag{2.34}$$

If we substitute values for γ_{vf}, $\partial\gamma_{vf}/\partial T$, $\partial\triangle G_v/\partial T$and $|\triangle G_v|$ that are true for most materials, then one can easily show the following inequalities

$$\left(\partial r^*/\partial T\right)_{\dot{R}} > 0 \tag{2.35}$$

$$\left(\frac{\partial \triangle G^*}{\partial T} \right)_{\dot{R}} > 0 \tag{2.36}$$

and

$$\left(\frac{\partial r^*}{\partial \dot{R}} \right)_T < 0 \tag{2.37}$$

Direct chain-rule differentatiation of eqns. (2.34) and (2.35), yields

$$\frac{\partial r^*}{\partial \dot{R}} = \left(\frac{\partial r^*}{\partial \triangle G_v} \right) \left(\frac{\partial \triangle G_v}{\partial \dot{R}} \right) = \left(\frac{-r^*}{\triangle G_v} \right) \left(\frac{-KT}{\Omega \dot{R}} \right) \tag{2.38}$$

Since $\triangle G_v$ is negative, the overall sign is negative.

Similarily, it is easily shown that

$$\left(\partial \triangle G^*/\partial \dot{R}\right) < 0 \tag{2.39}$$

All of the four inequalities of eqns. (2.35), (2.36), (2.37) and (2.39) have interesting implications and describe a number of common effects observed during film deposition.

From eqn. (2.36) one can deduce that a higher substrate temperature leads to an increase in the size of the critical nucleus and a discontinuous island structure is predicted to persist to a higher average coverage than at low substrate temperatures. The inequality of eqn. (2.37) suggests that a nucleation barrier may exist at high substrate temperatures, whereas at lower temperatures it is reduced in magnitude. Because of the exponetial dependence of the nucleation rate, N^* on $\triangle G^*$, the number of supercritical nuclei decreases rapidly with temperature. Hence, a continuous film will take longer to develop at higher substrate temperatures. From eqn. (2.38), it is clear that increasing the deposition rate results in smaller islands. This is because $\triangle G^*$ is also reduced, nuclei form at a higher rate, resulting in the formation of a continuous film at lower average film thickness. High substrate temperatures and low deposition rates are associated with large r^* and $\triangle G^*$ values and this leads to the formation of large crystallites or even monocrystalline films. Alternatively, low substrate temperatures and high deposition rates yield polycrystalline deposits. It has been observed by several authors [95],[96] that substrate temperature has an effect on the microstructure of the film in terms of orientation, density and grain size, morphology and phase transitions.

2.5.2 Film thickness

Film thickness is a very important parameter that affects the microstructure and physical properties of the film, as the film thickness and grain size are related to each other. Hence the mechanical properties of a film depends on these properties. In this study, the grain size as a function of film thickness is evaluated using the Scherrer equation.

2.5.3 Substrate bias voltage

The substrate is negatively biased by a voltage $-V_b$. This floating potential enhances positive ion bombardment, i.e. the argon ions and the constituent BFO ions, while decelerating oxygen ions. As the bias voltage increases, collisions may become dominant and attenuate the ion energy. Hence, the average energy of particles striking the substrate will not increase rapidly with the applied bias voltage [50]. The negative substrate bias voltage *($-V_b$)* is the main deposition parameter in plasma

assisted film depositions. It determines the kinetic energies of the bombarding ions that arrive on the substrate. This process significantly affects the chemical composition, structure and residual stresses in the as-deposited films. The influence of bias voltage on the growth morphology of films made by RF magnetron sputtering has been studied by researchers [97]. In this study the effect of substrate bias voltage on the microstructure, morphology and the stress evolution in BFO thin films is investigated.

2.5.3.1 Incorporation of foreign atoms

Foreign atoms which are incorporated into the growing film due to biasing can form compounds with the film atoms or can assume interstitial or substitutional positions. Thus, foreign atoms can change the intrinsic stresses, the stoichiometry, the crystal structure of the films, etc. Impurities located at grain boundaries can lead to embrittlement. Within the grain boundary they can form polymorphic phases. Foreign substances can also prevent columnar film growth due to permanent renucleation so that a fine-grained microstructure is found. In this study argon ions were implanted into the BFO films to study the stress evolution.

2.5.4 Sputter power

The sputter power has the effect of increasing the argon bombardment rate on the target. This increases the deposition rate of the films. In addition, the carrier density changes [98] with increasing rf power. The change in the plasma density also affects the thermalization distance of the sputtered particles and as a result modifies the film properties and its stoichiometry [99]. As the sputtering power increases the structure of the BFO films can be changed from amorphous to polycrystalline. Hence, the use of different sputtering powers to grow BFO thin films can have an affect on their microstructure and physical properties.

2.6 Stress in RF magnetron sputtered thin films

2.6.1 Stress in sputtered thin films

Practically speaking, all vacuum deposited coatings are in a state of stress. The total stress is a constituent of both thermal and intrinsic stresses. The thermal stress arises from the difference between the thermal expansion coefficients of the coating and

the substrate and is generally independent of the deposition process. The instrinsic stress is due to the aggregate effect of the crystallographic flaws that are built into the coating during deposition [100].

2.6.1.1 Thermal stress (extrinsic stress)

Thermal stress results from strain associated with differing thermal expansion coefficients of the film and the substrate. The values for the BFO film and the substrate are $6.5 \times 10^{-6}\ K^{-1}\ -13 \times 10^{-6}\ K^{-1}$ [101] and $2.57{\times}10^{-6}\ K^{-1}$-$4.33{\times}10^{-6}\ K^{-1}$ [102], respectively . The thermal stress induced is somewhat less important here, as we can fairly think that the difference between thermal expansion coefficients are relatively small and the extrinsic stress is very small as compared to intrinsic stress.

2.6.1.2 Intrinsic stress / compressive and tensile strain

Intrinsic stress developed during thin film growth is attributed to the non-equilibrium processes of deposition and the changes in the growth parameters. The intrinsic stress δ_i generated during the film growth is expressed as [103]

$$\delta_i = \delta_{sh} + \delta_{diff} + \delta_{ip} \tag{2.40}$$

where δ_{sh} represents the tensile stress originating from the volume shrinkage accompanying grain growth, δ_{diff} is the compressive stress component due to the ad-atom diffusion to the grain boundaries and δ_{ip} is the intrinsic stress associated with irradition of the growing surface.

Chapter 3.

Characterization techniques

This chapter gives the theoretical background of the experimental tools used to carry out systematic measurements of morphology, structure and composition of the films. In this respect, the work examines the tools to investigate the effect of deposition conditions on surface morphology, microstructure and the crystal structure of BFO thin films. Atomic force microscopy (AFM) was used to control roughness of the films since surface Brillouin scattering experiments are sensitive to surface roughness of the films. Field emission scanning electron microscopy (FESEM) was employed to study the microstructure of the grown films. X-ray reflectivity (XRR) was carried out to determine the density, thickness and surface and interface roughness of the films as these are important input parameters for extraction of the elastic constants from surface Brillouin scattering measurements (SBS). The stoichiometry or composition of any material is very important in order to understand the material properties. In this regard, Rutherford backscattering spectroscopy (RBS) had been employed. The crystallinity phase of the samples was analysed by grazing incidence X-ray diffraction, as the structure of the films is needed for the derivation of the elastic constants.

3.1 Atomic Force Microscopy (AFM)

The surface topography and morphology were characterized by Tapping Mode Atomic Force Microscopy (TM-AFM) (The AFM was a Digital Instruments Dimension 3100, Veeco instrument). Images were acquired at room temperature using a silicon cantilever with a spring constant of 2 Nm^{-1}-5 Nm^{-1} and tip diameters of 20 nm. The machine operates Nanoscope v 531r1 software for both post-capture image and real-time analysis processing. The AFM was placed on a vibration isolation table and all images were captured while operating in non-contact mode under ambient

conditions. The working principles of the AFM are illustrated in Figure 3.1 below. The non-contact mode allows surface profiling by scanning a tip (Si_3N_4) on a flexible cantilever to follow the topography of the surface at an atomic-scale resolution. The short distance between the tip and the sample's surface enables a van der Waals interaction between the atoms on the tip and those on the sample. This interaction leads to the deflection of the cantilever, which gives the Z profile of the sample. The deflection is controlled by using a laser beam, which passes through the cantilever and reflected onto a position-sensitive photodetector (PSPD). A feedback loop is used to ensure that the force applied to the cantilever is kept constant.

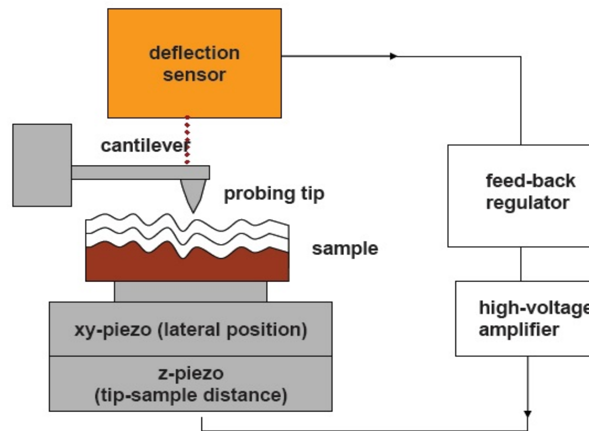

Figure 3.1: Atomic Force Microscope principles. Illustration of the feedback loop [104]

The roughness of the film can be calculated from the AFM image. The root mean square (RMS) roughness is the standard deviation of the Z values within a given area [105]:

$$RMS(nm) = \sqrt{\frac{\sum_{j=1}^{N}(Z_j - Z_m)^2}{N-1}} \tag{3.1}$$

where Z_m is the mean surface level within a given area, Z_i; is the current Z value and N is the number of pixels (related to the number of measurements) within a given area.

3.2 Field Emission Scanning Electron Microscopy (FE-SEM)

The microstructure analysis of the $BiFeO_3$ films deposited on (001) Si substrates was assessed by cross-sectional high resolution field emission scanning electron microscopy (FESEM). The instrument was a Jeol Ltd, Model 7001-F, (Tokyo, Japan) with a resolution of 3 *nm* at 15 *kV*.

3.3 X-ray Reflectometry (XRR)

X-ray reflectivity (XRR) measurements were carried out to determine the density, film thickness and surface roughness using a high-resolution X-ray diffractometer (Bruker AXS D8 Discover) based on a symmetrical arrangement of incident and secondary beam optics. The angles ω and 2θ can be configured from sample alignment with a scanning movement of speed 2:1. The scanning range is set to measure from critical angle $\theta_c \sim 0.8^\circ$ to the angle $2\theta = 5^\circ$, where the intensity diminishes to background levels. The XRR technique is based on total external reflection since the refractive index of the medium is less than 1. In this arrangement X-rays incident at an angle less than the critical angle θ_c will be reflected at the air-film interface. Using Snell's law and elastic scattering the electron density of the film can be obtained from the critical angle for total reflection, i.e. $\theta_c = \lambda\sqrt{\frac{r_e \rho_e}{\pi}}$, where r_e is the Bohr atomic radius and ρ_e is the electron density. The oscillation curve of the XRR spectrum is a function of the film thickness and refractive index σ of the layer in which information about the film thickness (thickness of Kiessing fringes) is obtained. The film thickness can thus be given as $d = \frac{1}{2}m\lambda\frac{1}{\sqrt{\theta_m^2 - \theta_c^2}}$ where m-th interference maximum and d is the thickness. Surface and interfacial roughness (from the decay of the oscillation) are extracted using the Fresnel reflection coefficients, $\rho_{v,h}.exp(-\frac{d}{2\sigma^2})$. A typical X-ray reflectivity diagram to illustrate the interference of the reflected X-rays at the film-substrate interfaces is presented in Figure 3.2. The X-ray reflectivity data were simulated by Leptos software from Bruker AXS [106].

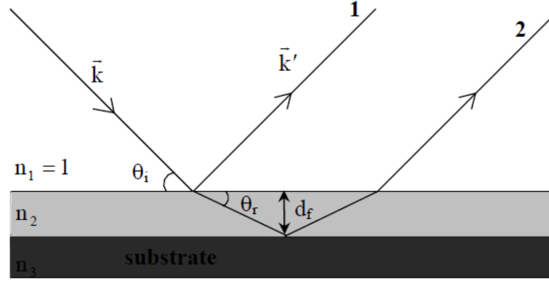

Figure 3.2: Schematic diagram depicting the X-ray total external reflection from a film substrate system [76].

3.4 Rutherford Backscattering Spectroscopy (RBS)

Rutherford Backscattering Spectroscopy (RBS) is a technique to determine the composition of BFO thin solid films. It is based on the principle of elastic scattering of $4He^{+}$ ions of energy 1.6 MeV upon irradiation of a sample. The energy and angle of the scattered ions yield information about the mass of the scattering atom in the sample. The backscattered energy E_1 of the ions is given by

$$E_1 = E_0(\frac{M_i cos\theta + \sqrt{M_f^2 - M_i^2 sin^2\theta}}{M_i + M_f}) \tag{3.2}$$

$$\equiv E_0 K_{M_f}(\theta) \tag{3.3}$$

where θ and $K_{M_f}(\theta)$ are the kinematic scattering factors, E_0 and M_i are the initial ion energy and mass, respectively, and M_t are the mass of the target atom (sample). The information exploited in this scattering phenomenon (the energy of the backscattered ions) can be used for compositional analysis of the thin films.

The incident ions lose energy as they traverse the sample due to inelastic collisions with electrons of the target (sample) atoms. This is explained as the stopping power, which is the energy loss per unit path length, dE/dx, given by

$$-\frac{dE}{dx} = \frac{2\pi Z_i^2 e^4}{E_i} N Z_t (\frac{M_i}{m_e}) ln \frac{2 m_e v_i^2}{I} \tag{3.4}$$

where N is the atomic density, m_e the electron mass, E_i and v_i the ion energy and velocity, respectively, and I is the excitation energy of the target atoms. The total

energy loss of the ion as it penetrates a distance x can be given as

$$\triangle E_{in} = \int_0^x \frac{dE}{dx}dx \approx x\frac{dE}{dx}\mid_{in} \tag{3.5}$$

This approximation is important for the computational simulations of RBS spectra. All the RBS measurements in this work were taken from the Tandem-Van de Graaff accelerator in the Universal beam line (0°), at the Department of Physics, University of Pretoria. All the measurements were done in a standard RBS chamber under a vacuum of 10^{-6} Torr and using a detector set at a laboratory angle of 165°with respect to the incoming incident radiation in Cornell geometry (5 *msr* solid angle). The beam current was 12 *nA*. The samples in the RBS chamber were bombarded with $4He^+$ ions that were deflected into the chamber. These ions were deflected as backscattered and their intensity was measured at the detector. The data were taken until an 8 μC charge was accumulated (about 12 minutes). Finally the RBS spectra were simulated and analysed off-line using the RUMP software package [107].

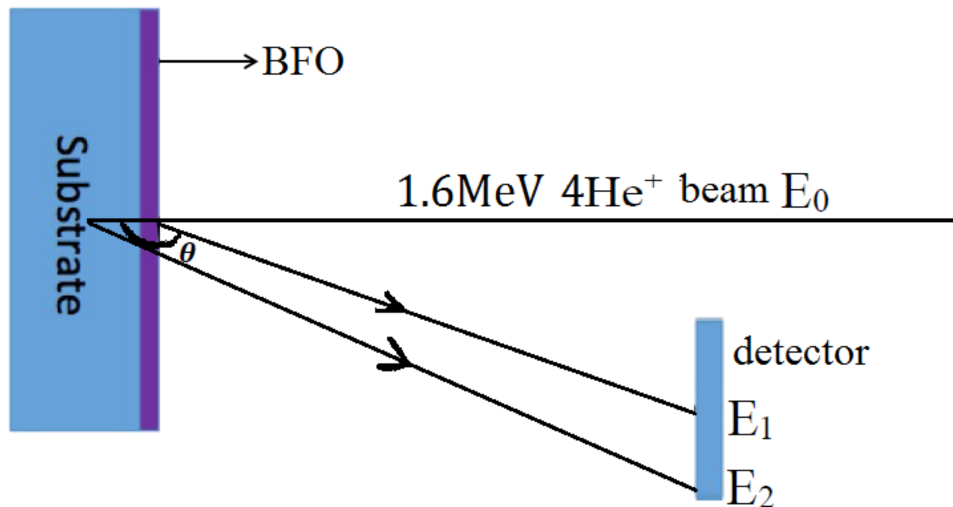

Figure 3.3: Schematic illustration of a typical RBS experiment [108]

Fig. 3.3 depicts the geometrical setup of an RBS experiment. The incoming beam of energy $E_\circ$ is backscattered by the sample to give backscattered energies of $E_1$and E_2, respectively. The laboratory angle for the detector was set to $\theta = 165^\circ$. In addition, Figure 3.4 shows a typical RBS spectrum of the as depostited films grown with 30 W sputter power. Three peaks are observed in the spectrum which represent the three elemental constituents of the BFO thin films. The energy difference ΔE between the reflected energy at the film surface E_1 and the energy reflected after hitting the film substrate interface E_2 gives information about the attenuation in the

ion energy. The area of the peak represents the atomic density and its height is related to the atomic concentration. The broader peak in the spectrum represents the backscatter edge of the silicon substrate. The broadening of the peak arises from the loss of the incident energy by the time it strikes the silicon substrate and hence ΔE is much larger as compared to the energy changes of the elements in the film.

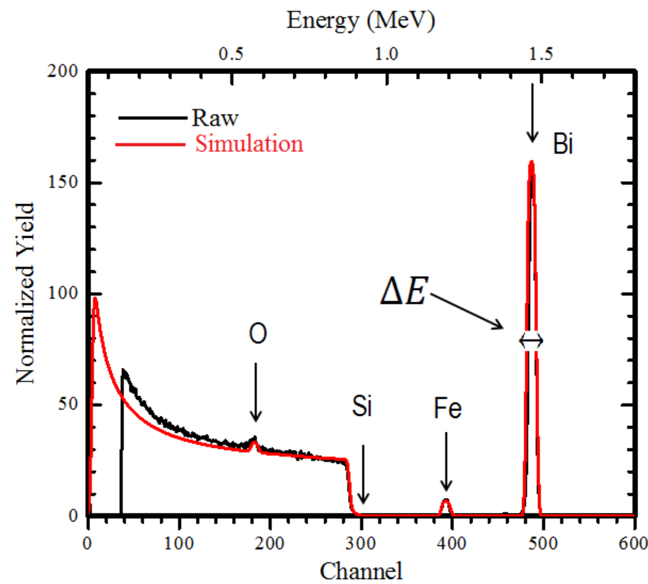

Figure 3.4: A typical RBS spectrum of a BFO thin film deposited on a silicon substrate with sputter power of 30 W.

3.5 Grazing Incidence X-ray Diffraction (GIXRD)

Grazing incidence X-ray diffraction is a non-destructive technique that employs a scattering geometry in combination with the Bragg condition. It uses the Seehmann-Brohlin scattering geometry in which the penetration depth typically ranges from $10-1000$ Å . This makes the diffraction method an excellent tool in the study of the crystal structure of thin film surfaces. GIXRD was used to identify the structural phases of the thin films. Glancing angle X-ray diffraction was done using a Bruker AXS D8 Discover diffractometer with $Cu\ K_{\alpha}$ radiation of $\lambda = 1.5406$ Å to analyse the structure of the deposited films. The diffraction profiles were collected between 20°and 60°with a glancing angle ω of about 1°. The crystalline phase and the d-spacing parameters were determined by comparing the peak positions and intensities using TOPAS software [99].

3.5.1 Bragg's condition

The monochromatic parallel beam of X-rays impinge on the sample to form constructive interference (diffraction) when the path difference is an integral number n of wavelengths λ.Thus, the mathematical expression for the condition for constructive interference of the incident and diffracted or scattered radiation is given as:

$$2d_{hkl}sin\theta = n\lambda \tag{3.6}$$

where d_{hkl}, θ, n and λ are the interplanar spacing, the angle of the lattice planes with respect to the incident X-ray beam, order of diffraction and the wavelength of the X-ray beam, respectively. Fig. 3.5 shows the scattered X-rays from atomic planes of spacing d_{hkl}. Bragg's law can be represented in terms of the reciprocal lattice. That is, the difference between $\vec{k_o}$ (incident vector) and $\vec{k'}$ (diffracted vector) is equal to a reciprocal lattice vector $\vec{G}$ (connecting two lattice points in reciprocal space) as shown in Fig. 3.5. The lattice spacing of the planes is given by $d_{hkl} = 2\pi/|\vec{G}|$.

$$2 \mid k_o \mid sin\theta =\mid G_{hkl} \mid= \frac{2\pi}{d_{hkl}} \tag{3.7}$$

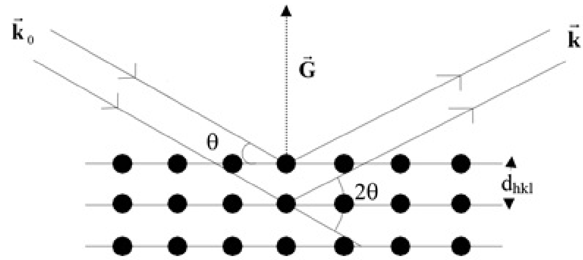

Figure 3.5: Bragg's condition for diffraction in real space. If the path difference $\triangle = 2d_{hkl}sin\theta$ between the rays scattered from the parallel planes is equal to multiples of the wavelength, λ, then constructive interference occurs and a Bragg peak appears at the corresponding angle 2θ [76].

3.5.2 Crystallite size

Crystallite size is defined as regions that are separated by large misorientation angles. Crystallite/grain size is the most fundamental parameter that play a major role in the mechanical properties of materials. This parameter can be controlled by the growth conditions. The shape, orientation and distribution of grain/crystallite size is important, as it determines the physical properties of thin films.

The X-ray diffraction measurements of the crystallite size and lattice strain depends on the XRD peak locations and widths. Thus there is a need to take the peak broadening into account. The d-spacing is directly affected by lattice strains, compositional variations and instrumental variables (diffraction slits, sample area, and diffracting layer thickness) and particle size.

The crystallite size can be given by using the Scherrer formula:

$$D = \frac{K\lambda}{\beta cos\theta} \tag{3.8}$$

where D is the crystallite size, β is the peak width in radians (FWHM) and it is the difference in angles at half maximum and can be calculated as the difference between 2θ high and 2θ low. θ is the Bragg angle, K is a constant having values between 0.9 to 1.0 depending on the grain shape . The above eqn. (3.8) is applicable for grain sizes ranging from 2 to 300 nm.

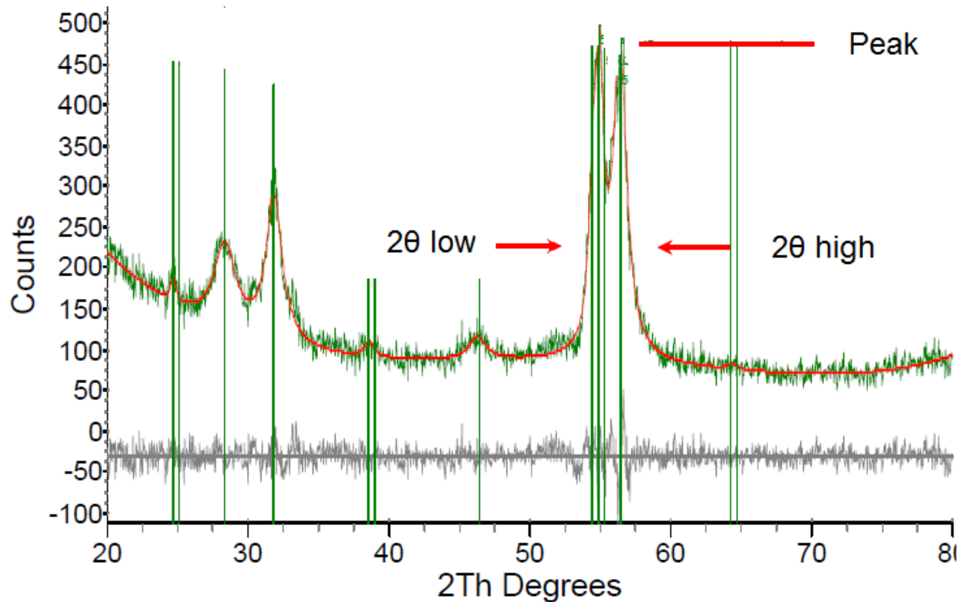

Figure 3.6: GIXRD profile with its 2θ peak position

3.5.3 Intrinsic strain determination

Intrinsic strain (ε_i) of the thin film is due to impurities, defects and lattice mismatch between the film and substrate. Hence, the strain depends on the substrate and the deposition parameters. Thus, the total strain ε in a thin film is given as :

$$\varepsilon = \varepsilon_i + (\alpha_f - \alpha_s)(\triangle T) \tag{3.9}$$

where α_f and α_s are the thermal expansion coefficients of the film and the substrate, respectively. $\triangle T$ is the difference between the deposition and room temperature. With the d-spacing of the strained film (d) being obtained from the GIXRD measurement, then the macro strain can be given as:

$$\varepsilon = \frac{d_0 - d}{d_0} \tag{3.10}$$

If d-spacing values are changed from their normal position to either a higher or lower value this indicates the presence of tensile or compressive strain in the film.

Chapter 4.

Experimental

This chapter discusses the experimental procedures that were employed for the techniques in order to fabricate and characterize our thin films and also for the determination of the stress evolution and elastic constants of our thin films. These includes RF magnetron sputtering, Atomic force microscopy (AFM), field emission scanning electron microscopy (FESEM), X-ray reflectivity (XRR), Rutherford backscattered (RBS), grazing incidence X-ray diffraction (GIXRD) and surface Brillouin scattering (SBS).

4.1 RF Magnetron Sputtering system

BFO thin films on a silicon substrate $[Si(001), 20 \times 20 \times 0.5\ mm^3]$ were prepared using the RF magnetron sputtering apparatus in the School of Physics of the University of the Witwatersrand. BFO target material manufactured by Semiconductor Wafer. Inc. with a diameter of 76 *mm*, thickness 6 *mm* and 99.9% purity was used. Figure 4.1 shows a picture of the RF sputter equipment used in the fabrication of the BFO thin films. The substrate was pre-cleaned ultrasonically, dried using pure N_2 and then loaded into the vacuum chamber with the BFO target material. The vacuum chamber was evacuated down to a base pressure of 10^{-6} *mbar* prior to deposition using a fore- and turbo-pump. The argon gas was then introduced into the chamber and the working pressure set to 10^{-3}*mbar* for plasma ignition.

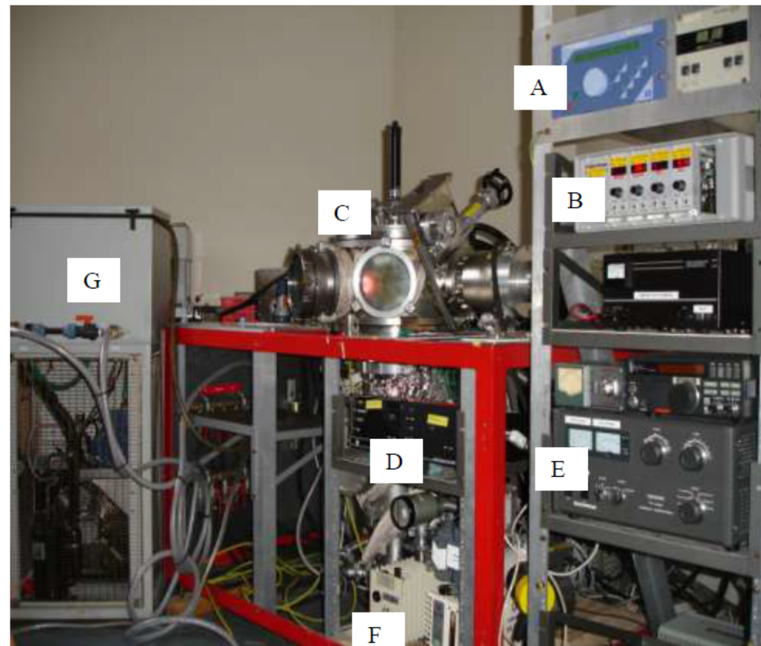

Figure 4.1: RF magnetron sputtering system. A-RF generator, PFG 300RF; B-gas control unit; C-vacuum chamber; D-turbo pump control unit, Turbotronik NT 150/360 VH; E-linear amplifier, Kenwood TL-922; F-fore pump; G-compact cooling unit [109].

The target was pre-sputtered for 10 min in an Ar atmosphere with sputter power of 100 W. The silicon substrates were etched with 6 W sputter power and substrate bias $-300\ V$ for 5 minutes in Ar atmosphere to remove the native oxide layer from the substrate surface and enhance adhesion. Table 4.1 shows the deposition parameters that were used for thin film synthesis.

Table 4.1: The sputtering parameters used for BFO growth.

Sputtering gas	*Operating pressure*	*RF power*	*Substrate temperature*	*bias voltage*	*Sputter time*
Ar	$10^{-3} mbar$	$(30-75)\ W$	RT, $(100-600^{\circ})\ C$	$(-25-100)\ V$	3 min–$6\frac{1}{2}$ hrs

4.2 Atomic Force Microscopy (AFM) apparatus

The AFM used in this study is a digital instruments Dimension 3100, (Veeco). It was operated in tapping mode. Si_3N_4-tips mounted on triangular-shaped Si cantilevers with a spring constant of $2\ Nm^{-1} - 5\ Nm^{-1}$ were used. The scanning areas used in this work were $1 \times 1\ \mu m^2$ and $2 \times 2\ \mu m^2$. The AFM images were analysed using the software package of $v531r1$.

4.3 Field Emission Scanning Electron Microscopy (FESEM)

The field emission scanning electron microscope (FESEM) used in this study is a JEOL 7001-F scanning electron microscope (FESEM) working at 15 kV, corresponding to a de Broglie wavelength of $\lambda = 0.0019$ Å. Its resolution at 15 kV is 3 nm. The electrons are emitted from a tungsten cathode. Cross sections of the samples were prepared by carefully cutting (breaking) perpendicular to the film surface.

4.4 X-ray Reflectivity (XRR)

X-ray reflectivity (XRR) measurements were carried out with the incidence and exit angle θ varied in the range from $0.1^{\circ} - 5^{\circ}$. As discussed in section 3.3, XRR provides information of the film's thickness, density and surface and interfacial roughness. Ex-situ X-ray measurements were performed using a Bruker D8 Discover diffractometer (Bruker AXS GmbH, Karlsruhe, Germany). The water-cooled stationary Cu-anode is bombarded with 40 mA electrons at 40 kV, which results in Bremsstrahlung and radiation characteristic of the Cu-anode to be emitted. The X-rays are filtered and focused by means of a Cu Gobel mirror, selecting only $Cu - K_{\alpha}$ radiation with $\lambda = 1.5406$ Å for the measurements. The raw reflectivity data were collected by a Lynx eye detector in OD mode after passing through computer-controlled motorized receiving slits with width of 0.1 mm. Auto-fitting was done by means of a genetic algorithm [106] with a logarithmic least-squares difference parameter used to evaluate goodness-of-fit.

4.5 Rutherford Backscattering (RBS)

The RBS measurements were performed using 1.6 MeV $4He^{+}$ ions obtained from a van de Graaff accelerator. The backscattered ion energies were measured by a Si semiconductor detector with energy resolution of about 20 keV. The detector is placed at an angle $\phi = 165^{\circ}$ with respect to the incoming ion beam. The backscattered ions impinge normal to the sample surface. However, for the sake of minimizing the possible effect of channeling, the samples were randomly tilted a few degrees with respect to the beam axis during measurement. The recorded spectra, i.e. the backscattered yield versus the ion energy, were analyzed using the RUMP software [107].

4.6 Grazing Incidence X-ray Diffraction (GIXRD)

The crystal structure of the BFO films was examined by standard Grazing Incidence X-ray Diffraction (GIXRD) with wide-angle Seehmann-Brohlin geometry. The $Cu\ K_{\alpha}(\lambda = 1.5406\ \text{Å})$ incident beam was used in the Bruker AXS D8 Discover diffractometer. The incident beam was conditioned using a Cu-Gobel mirror with a measured slit width of 0.1mm to give a high-intensity quasi-parallel beam. The diffracted X-ray intensity was collected by a Lynx eye detector in 2θ geometry (parallel beam geometry). The diffracted beam calibrated in the OD path was directed through the monochromatic, programmable receiving slit set at 9 mm to attain a parallel beam geometry in the secondary beam side. The angle of incidence of the X-ray beam was fixed at $\omega = 1^{\circ}$ to achieve a penetration depth of the order of the thickness of the films. Tube power was set to 40 kV/ 40 mA to attain a stable incident beam, and the detector (2θ) axis was scanned from 20°to 60°.

4.7 Surface Brillouin Scattering (SBS)

In this section the experimental setup used for the measurement of the surface Brillouin spectra is presented. The picture depicting this experimental arrangement is shown in Fig.4.2. This setup consists of essentially 4 main components. These are the laser source, the $(3+3)$ tandem Fabry–Pérot interferometer with the Sandercock configuration, computers for data acquisition and stabilization of the spectrometer, and finally the external optics for focussing the laser on the sample and simultaneous collection of the scattered light into the spectrometer. The details of the experimental setup of the surface Brillouin spectrometer used in this work are presented below.

4.7.1 Experimental setup

Brillouin light scattering experiments require the illumination of the sample with the laser beam, collecting the light in a given direction and spectrally resolving the shifted frequency of the scattered light. The filtering of the frequency shift of the back scattered light was performed by the tandem Fabry–Pérot interferometer. All the measurements are carried out at ambient temperature and pressure. The sample is on a sample holder on the optical table, as shown in Fig. 4.2.

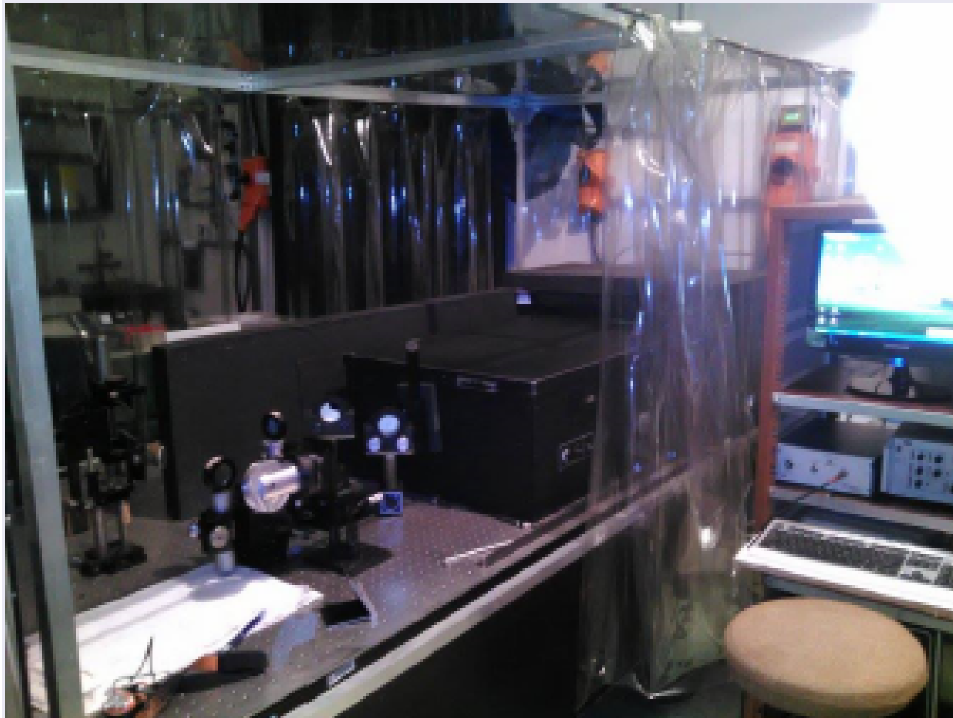

Figure 4.2: Systems of optics and other instrumentations of surface Brillouin scattering

SBS is a non-contact measurement which makes the technique best for experiments in which the specimen is kept in a controlled condition. The only condition needed is the optical access to the sample that is guaranteed by the optical windows. Figure 4.3 presents a schematic diagram of the whole experimental setup for surface Brillouin scattering. A single axial mode Ar^+ laser is used to illuminate the thin film sample after being directed by incidence mirror M1. It is focused onto the thin film sample surface by the front lens LA1. The backscattered beam is also focused onto the same lens LA1 and simultaneously collimates (make a parallel beam) the scattered light from the film surface. The backscattered light from LA1 is focussed onto the entrance pinhole P2 by the lens LA2. Spatial filtering is done by the pinhole. Two steering mirrors [M_3 and M_4] give additional degrees of freedom and are very useful for alignment purposes.

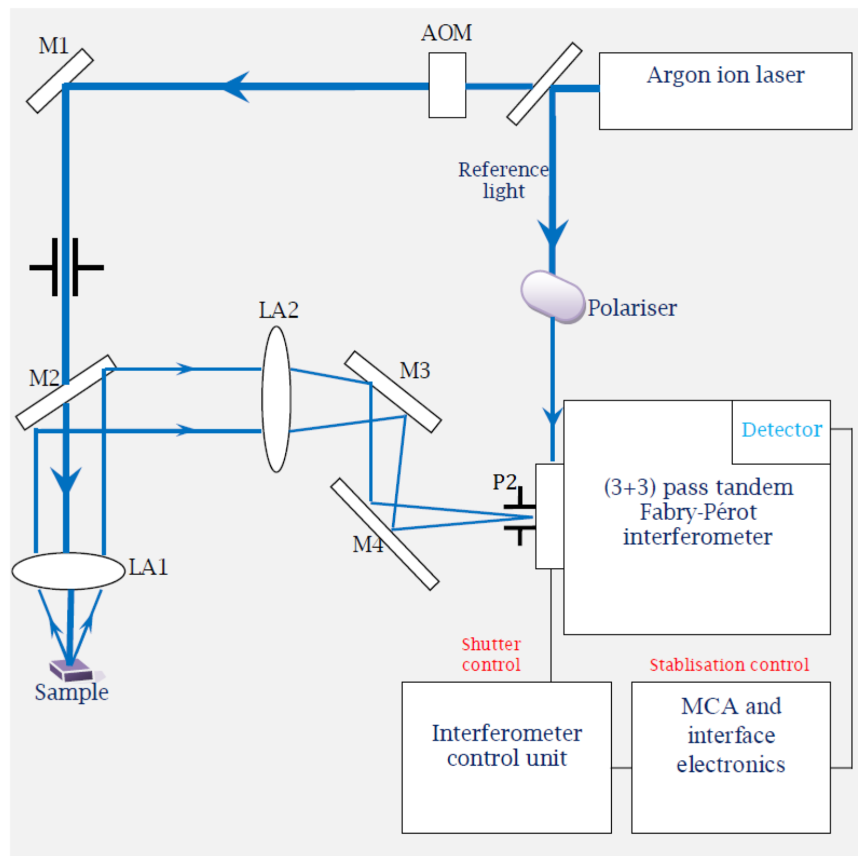

Figure 4.3: Schemetic diagram of the experimental arrangement used for surface Brillouin scattering spectroscopy including acoustic optical modulator (AOM) and multichannel analyser (MCA). M stands for mirrors and LA for lenses [110]

The reference light is required to stabilize and control the interferometer during scanning via the shutter control system. The polarizer controls the intensity of the reference beam. The incident light is polarized either parallel or orthogonal to the plane of incidence and the scattered light is collected without polarization analysis. A backscattering geometry is used to select a specific wave vector along the surface of the film and probe the surface acoustic waves. In addition, this permits the focussing of the laser onto the thin film surface and simultaneously collects the backscattered light with the same lens LA1.

4.7.2 Laser

A coherent Innova argon-ion laser that operated in a single axial (longitudinal) mode at wavelength 514.5 *nm* and power 200 *mW* was used for these measurements. The frequency shifts of the scattered light were in the range of a few *GHz* to about 150 *GHz* and therefore a very narrow laser linewidth or high resolution is required for

SBS measurements. From the broad gain profile of the laser as shown in the Figure 4.4, a single longitudinal mode was selected.

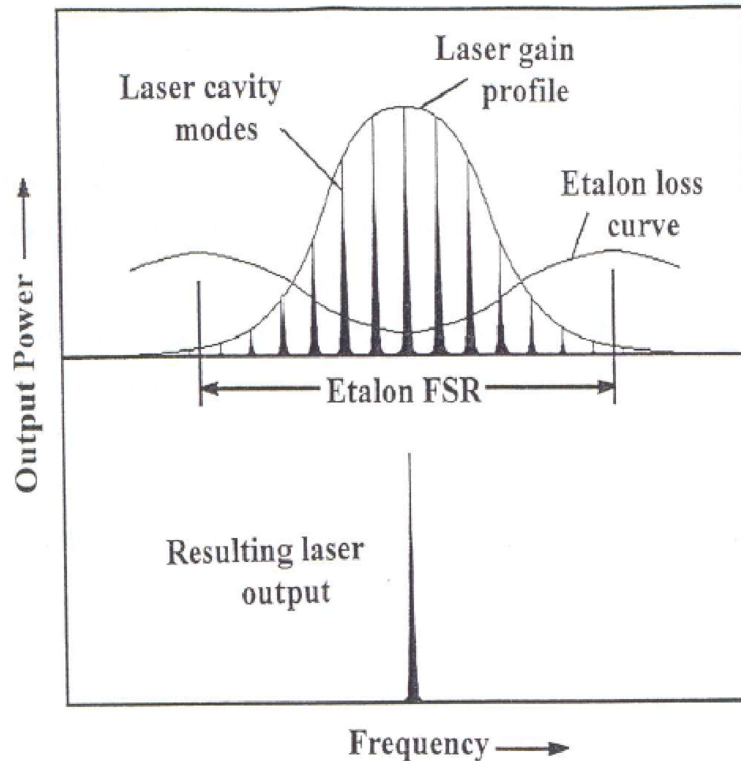

Figure 4.4: Selection of the single axial longitudinal mode from the intersection of the maximum of the laser gain profile and the minimum of the Etalon loss curve [109].

4.7.3 Fabry–Pérot interferometer

The frequency shift of the backscattered light is very small compared to the frequency of the laser (1 part in 100000 of the frequency of elastically scattered laser light). Hence, to filter out this frequency, a high resolution and high contrast interferometer is used. The Fabry–Pérot interferometer is an optical instrument that acts as a band pass filter. As its pass frequency can be adjusted, it can be used to scan the full spectrum width to be measured. The most widely used interferometer is the Sandercock type (Figure. 4.5) and it is able to resolve the weak Brillouin doublets. Sandercock showed that the contrast can be significantly improved by multipassing the interferometer with three, five or even seven passes. In our optical spectroscopy laboratory a (3+3) pass i.e. 6 times interferometer was used to achieve a contrast as high as 10^{11}. This contrast is sufficient enough to distinguish the weak scattered light from the intense elastically scattered light.

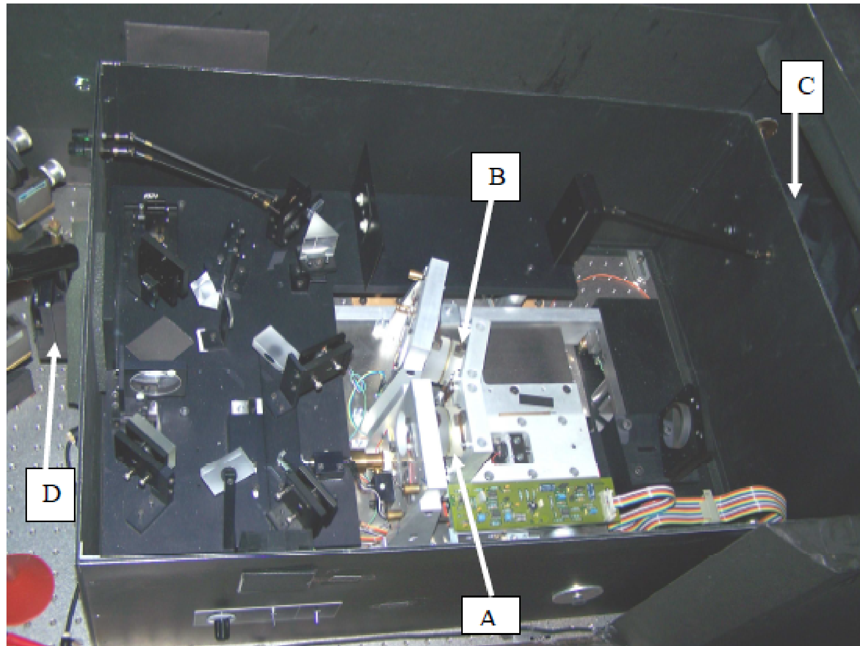

Figure 4.5: A photograph of a (3+3) multipass Tandem interferometer, in which A-FPI1(Fabry–Pérot 1), B-FP2 (Fabry–Pérot 2), C-the detector (placed on the TFPI box) and D- the shutter [109].

Two synchronized coupled Fabry–Pérot interferometers are used in tandem to prevent the overlapping of different orders of interference fringes. The most useful arrangement is a system with two interferometers in which the spacing of the second one L_2 is close to L_1, where L_2 and L_1 are the optical distances between the mirrors. In general a good practical value for L_2/L_1 is 0.95. A plane view of the two Fabry–Pérot interferometers on a single translational stage is depicted in Figure 4.6.

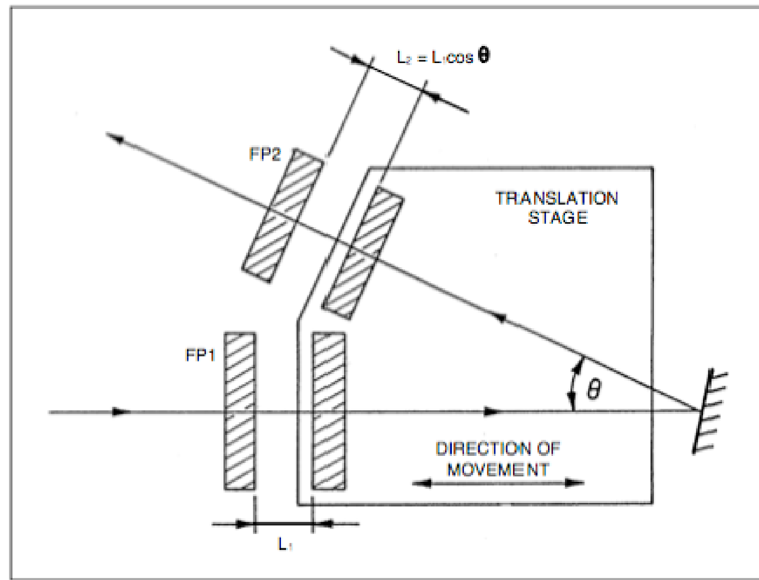

Figure 4.6: Translational stage of the two Fabry–Pérot interferometers, Fabry–Pérot 1, Fabry–Pérot 2 that are able to scan synchronously [111].

Chapter 5.

Results & Discussion: Characterization studies

5.1 Introduction

In this chapter the results of BFO thin film characterizations are presented and discussed.

5.2 Surface topography and cross-section image studies

The surface morphology and topography images of $BiFeO_3$ thin films on a (001) Si substrate under various deposition conditions are presented in Figs. 5.1-5.6. The micrograph of the film prepared at 30 W reveals a very dense and compact granular morphology, as shown in Fig. 5.1 [a]. Films produced at increased sputter power and substrate bias voltage show mosaic structure with defined columnar grains separated by voids (Figs. 5.1[b], 5.2[a]-[b], 5.5[a]-[b] and 5.6[a]-[b]). Figures 5.3[a]-[b] and 5.4[a] depict round like and fully developed grain structures of films fabricated at 50 W and substrate temperatues of $100°C$, $200°C$ and $400°C$. On the other hand, at $600°C$ the formation of quasi-interfaces was observed as indicated in Fig. 5.4[b]. The microstructure and morphology of the films conform to the Structural Zone Model (SZM) [112-113]. This model examines the effect of substrate temperature(T_s) on the film surface structure and microstructure, based on the $\left(T_s/T_m\right)$ ratio. The film microstructure is thus divided into 3 main structural zones with boundary temperature; $T_1 = 0.3T_m$ and $T_2 = 0.5T_m$, where $T_m(K)$ is the melting temperature of the target material. At low temperatures $(T < T_1$, zone 1), the surface diffusion of adatoms is limited and this leads to the formation of the

characteristic well defined columnar structure. Films deposited at higher temperatures ($T_1 < T < T_2$, zone 2) show larger columns and grains. In this instance, the surface diffusions of the adatoms enables surface crystallization of the film in the growth direction. The films deposited at ($T > T_2$, zone 3) exhibit big grains with flat and faceted faces [89]. The root mean square (RMS) roughness (Rq) parameter was measured using AFM software (v531r1) [112].

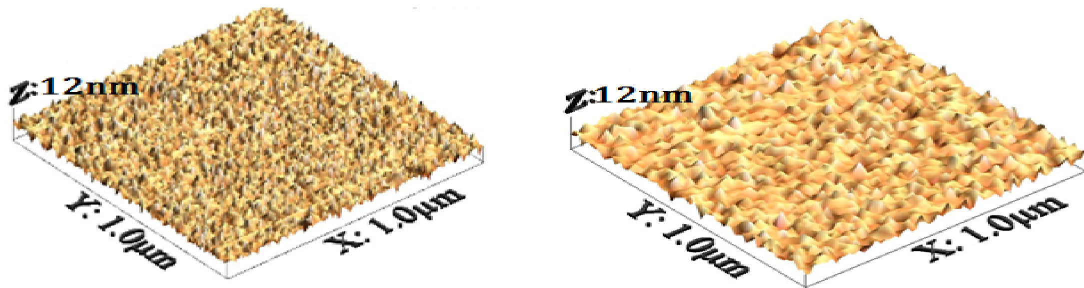

[a] 30 W sputter power ($R_q = 0.886$) [b] 40 W sputter power ($R_q = 0.946$)

Figure 5.1: Surface topography of the pristine BFO thin films deposited at 30 W and 40 W for 5 min at room temperature and $V_b = 0$ V, respectively.

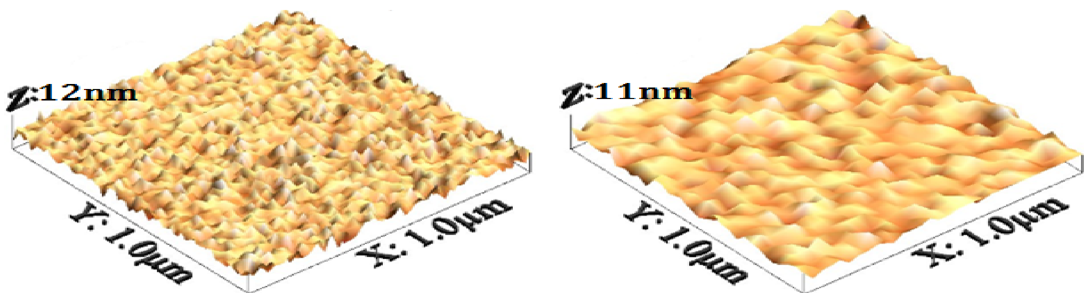

[a] 50 W sputter power ($R_q = 1.012$) [b] 75 W sputter power ($R_q = 1.031$)

Figure 5.2: Surface topography of the pristine BFO thin films deposited at 50 W and 75 W for 5 min at room temperature and $V_b = 0$ V, respectively.

The surface roughness and grain size of BFO films increase with sputter power, substrate temperature and substrate bias (Table 5.1). The increase in sputter power enhances the ad-atom mobility and contributes to the crystal growth and higher surface roughness. The increase in surface roughness of the films with increase in substrate temperature is due to grain growth, following surface and grain boundary diffusion, atomic peening effects, ad-atom mobility enhancement, film thickness, and induced thermal stress [113]. The grain growth of the films deposited

at a higher temperatures of 100°C , 200°C, 400°C and 500°C changes from island growth (Volmer-Weber mode) to the layer growth of the (Frank-van der Merwe mode) due to enhanced diffusion. BFO films grown at 600°C exhibit a higher surface roughness, attributed to voids and defects on the surface associated with the volatility of Bi. The grain growth mechanisms for films deposited at 600°C do not conform to the SZM but rather to a growth by ordered coalescence.

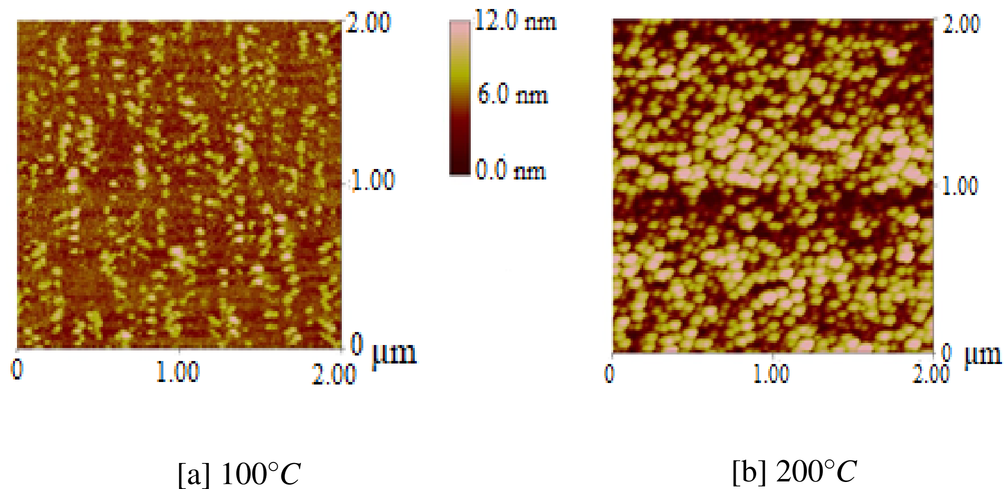

[a] 100°C [b] 200°C

Figure 5.3: AFM micrographs of the pristine BFO thin films grown at 50 *W*, at [a] 100°C and [b] 200°C for 5 *min*. The substrate bias voltage was set to zero for both cases.

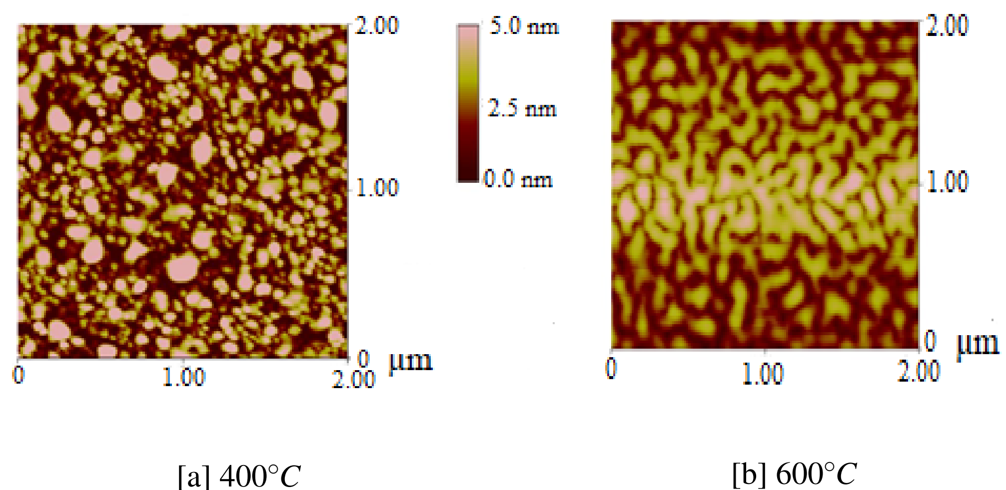

[a] 400°C [b] 600°C

Figure 5.4: AFM images of the pristine films produced at 50 *W*, at [a] 400°C and [b] 600°C for 5 *min*. The substrate bias voltage was set to zero for both cases.

The AFM images shown in Fig. 5.5 and Fig. 5.6 depict the variations of surface

roughness of BFO films deposited at various negative substrate biases. The change in roughness with negative substrate bias is attributed to the Ar^+ bombardment and re-sputtering at high energies (self-bias, plasma potential and bias voltage). The surface of a film may be roughened and this could increase mechanical interlocking [114].

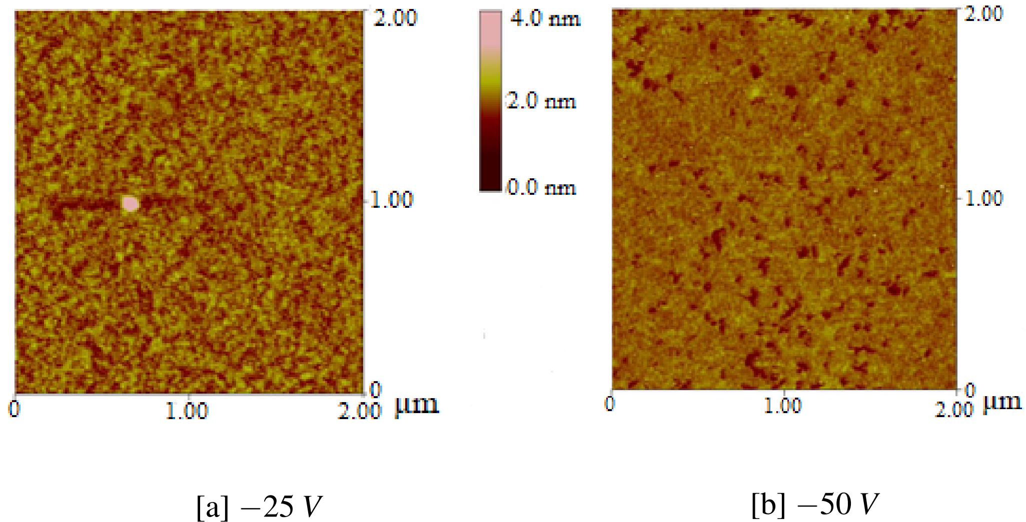

Figure 5.5: AFM images of films grown at 50 W with varying substrate bias of [a] -25 V $(R_q = 0.232)$ and [b]-50 V $(R_q = 0.197)$, respectively.

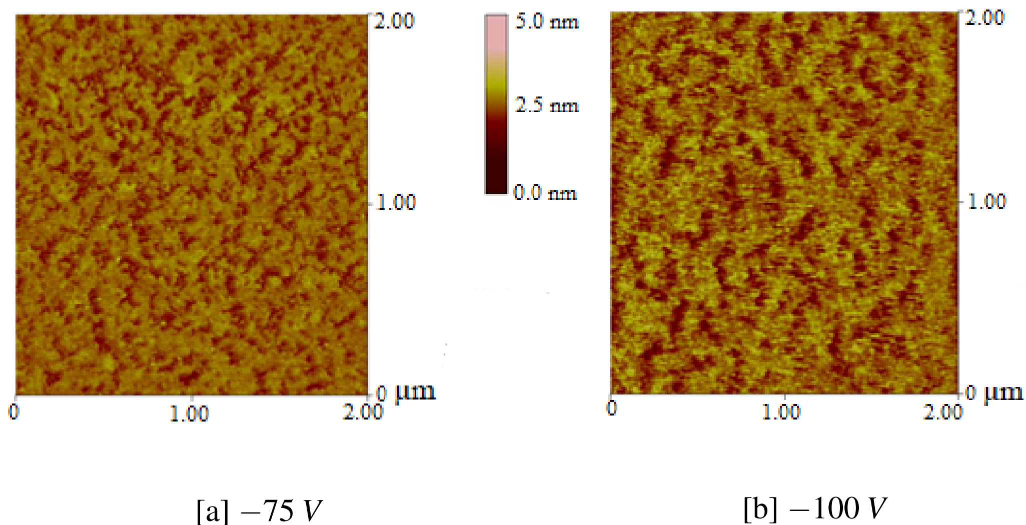

Figure 5.6: AFM micrographs of films grown at 50 W with substrate bias of [a]-75 V $(R_q = 0.219)$ and [b] -100 V $(R_q = 0.383)$, respectively.

The BFO films deposited at room temperature, (in which, $T_s/T_m = 0.18$) showed a less dense morphology. This relates to the boundary between zone 1 and zone

2, in the Structural Zone Model (Fig. 5.1 [a]-[b] and 5.2 [a]-[b] ; Fig 5.3 [a]-[b]-Fig. 5.4 [a] and Fig. 5.5 [a]-[b]; Fig. 5.6 [a]-[b]). However BFO films grown with $T_s/T_m > 0.3$ have shown that the film growth mode is incompatible with the predictions of the Structural Zone Model (Fig. 5.4 [b]). The morphology of the BFO films grown with different sputter power, substrate temperature ($< 600°C$) and bias voltage are in agreement with the Structural Zone Model (SZM).

Table 5.1: Effect of deposition parameters on surface roughness and crystallite size

Parameters	RMS roughness (nm)	T_s/T_m	SZM	Film thickness(nm)
30 W	0.886	0.18	I	40.52
40 W	0.946	0.18	I	56.44
50 W	1.012	0.18	I	66.86
75 W	1.031	0.18	I	117.36
$100°C$	1.131	0.222	I	29.91
$200°C$	1.393	0.281	I	28.53
$400°C$	1.762	0.399	II	24.51
$600°C$	2.905	0.581	not governed	18.37
-25 V	0.232	0.18	I	84.98
-50 V	0.197	0.18	I	58.38
-75 V	0.219	0.18	I	60.89
-100 V	0.383	0.18	I	70.29

In addition, the film cross-section images have been studied by field emission scanning electron microscopy (FESEM) by scanning a transversal surface section of the film on the cut edges perpendicular to the growth direction. The growth mode of the as deposited film on Si (001) based on the SZM for thicknesses 375 *nm*, 750 *nm*, 950 *nm* and 1000 *nm* and sputter powers of 30 *W* and 75 *W* are shown in Fig. 5.7 and Fig. 5.8. The influence of the sputtering time and power are evident in the microstructure of the deposition growth made for 3 *hrs*, 5 *hrs,* and $6\frac{1}{2}$ *hrs* at 300 K. The average surface roughness and grain size of the BFO films increases with the deposition time and sputter power. Fig. 5.7 [a] shows that BFO films (375 *nm*) has a very dense columnar growth. A dense, fine and grainy columnar growth is seen for all images irrespective of the sputter and deposition time. As shown in Fig. 5.7 [a]-[b] and 5.8 [c]-[d], the increase in deposition time facilitates grain growth and densification during thin film growth. This effect can be attributed to the prolonged dissipation of the kinetic energy of the ad-atoms. The higher sputter power facilitates grain growth as can be compared and seen from Figures 5.8 [c] and [d].

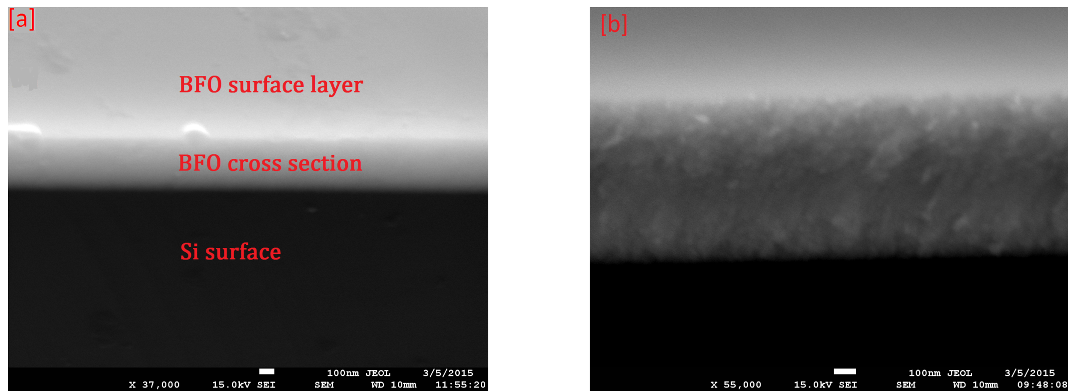

Figure 5.7: FESEM cross-sectional image of the BFO films prepared at [a] 30 W-3 hrs, [b] 30 W-5 *hrs,*

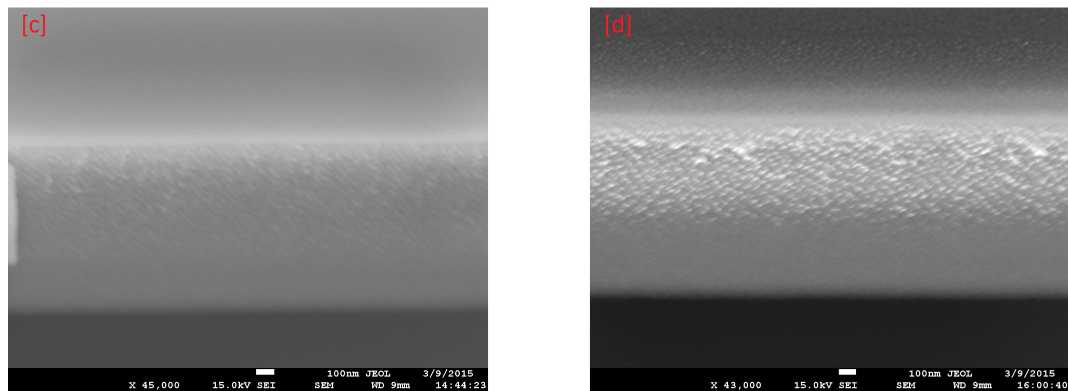

Figure 5.8: FESEM cross-sectional image of the BFO films prepared at [c] 30 W-$6\frac{1}{2}$ hrs and [d] 75 W-3 *hrs*.

5.3 Stoichiometric (composition) studies by RBS

The stoichiometry of the samples was determined by Rutherford Backscattering (RBS) analysis. The RBS data were fitted using the Rutherford Universal Manipulation (RUMP) computer code [107]. This fitting procedure gives layer by layer information about the film thickness and composition. A typical RBS spectrum of the as-deposited films grown at a sputter power of 30 W is shown in Fig. 5.9. The arrows indicate the surface channel positions of Bi, Fe, O, Si, and Ar. The Ar peak is not clearly discernable in the spectrum; it is inserted merely to locate and show the channels of the Ar element in the spectrum. The raw data is represented by the black solid line overlaid with a red solid line obtained from the RUMP simulations. The spectra indicate distinct signals of Bi, Fe, and O. The Ar signals become more

pronounced in the spectrum of thin films deposited at various negative substrate bias voltages.

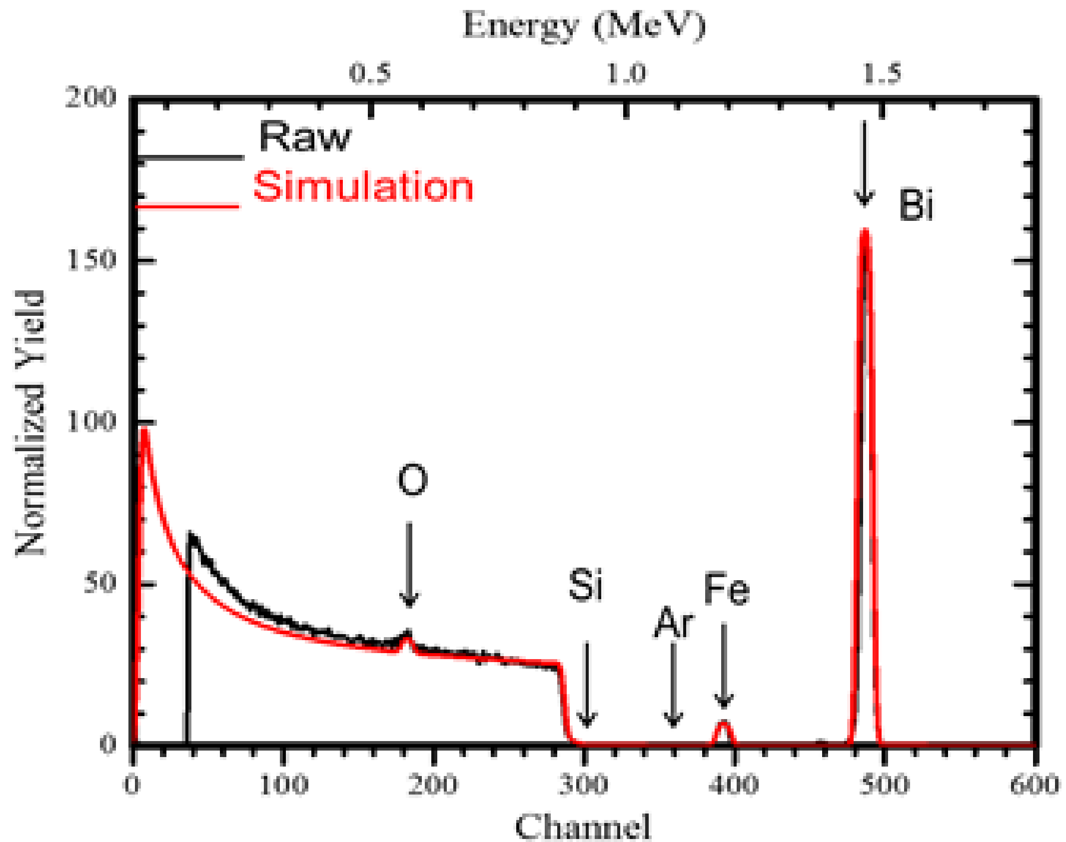

Figure 5.9: RBS spectrum of as deposited layer of pristine BFO film deposited at 30 W, room temperature and $V_b = 0\ V$ on (001) Si. The black and red plots are raw and simulated data, respectively.

In Fig. 5.10 [a] the RBS experimental spectra of a BFO thin films on Si (001) for samples prepared with 30 W, 40 W, 50 W and 75 W are presented. Fig. 5.10 [b] represents the enlarged diagram to precisely illustrate the composition variation with sputter power. The zoom out is carried from the 200-400 channels. All the BFO layers are non-stoichiometric as shown in Table 5.2. Similarly, Fig. 5.11 shows a single layer structure of BFO of the RBS data for the films made with substrate bias set at -25 V, -50 V, -75 V and -100 V, respectively.

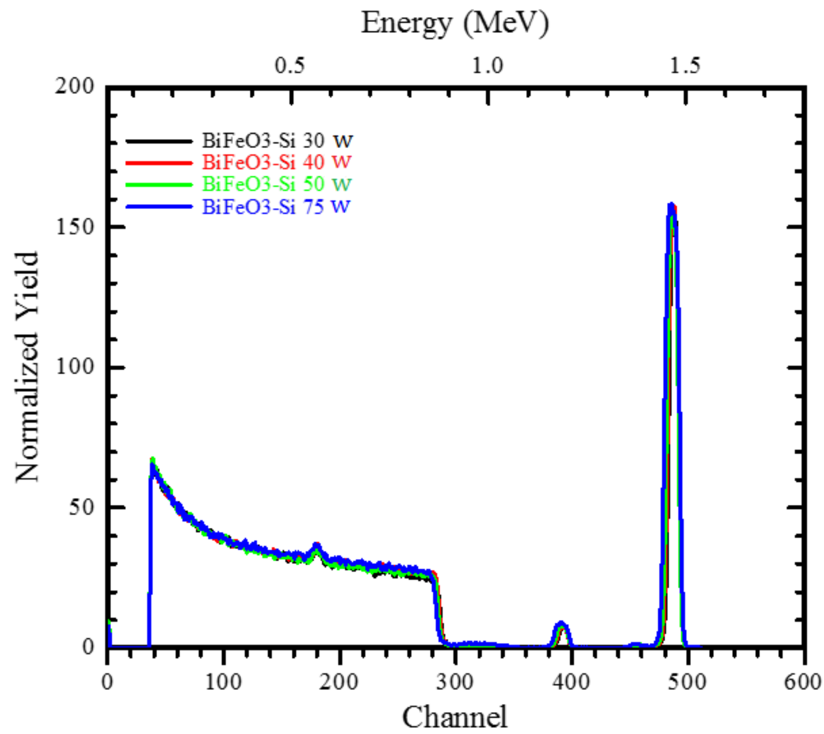

Fig. (a)

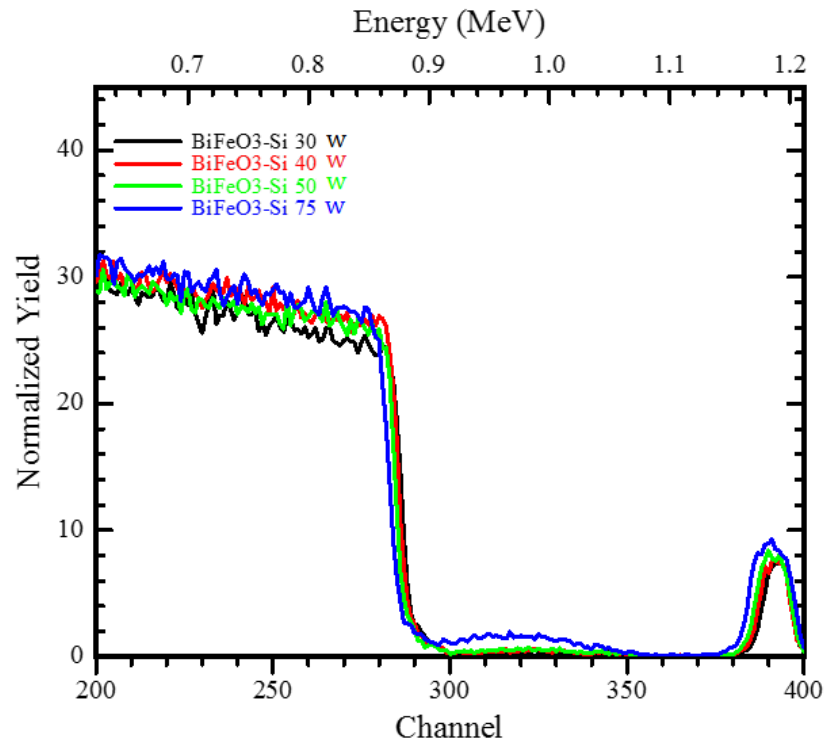

Fig. (b)

Figure 5.10: [a] RBS spectra of the pristine BFO deposited at 30 *W*, 40 *W*, 50 *W* and 75 *W* for 15 *min* at room temperature and zero substrate bias voltage. The black, red, green and blue plots are used for comparison of the raw data. [b] A zoom in from channels 200 to 400 to depict the compositional variation of BFO films under the various deposition conditions.

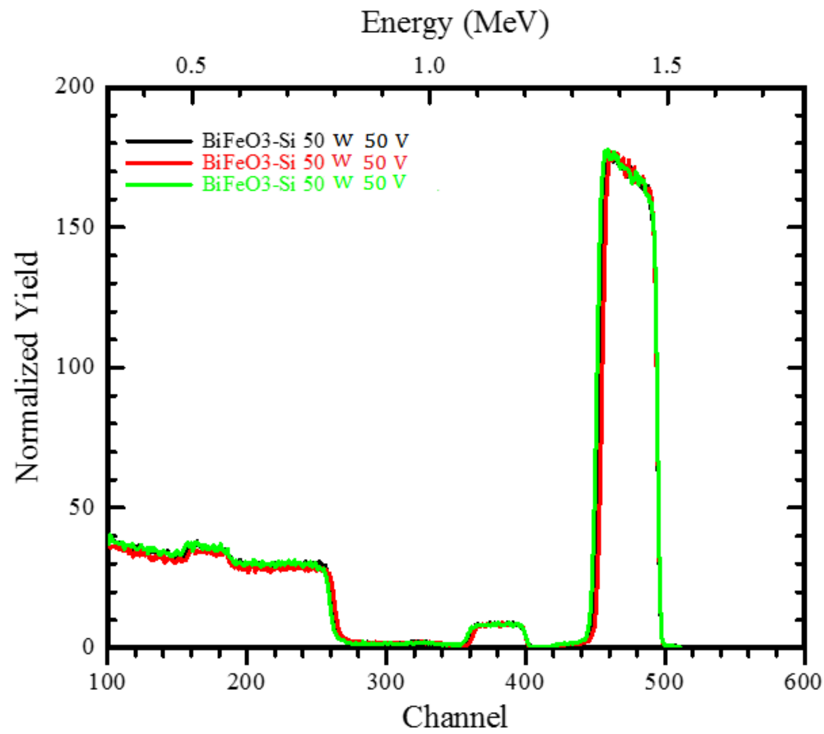

Fig. (a)

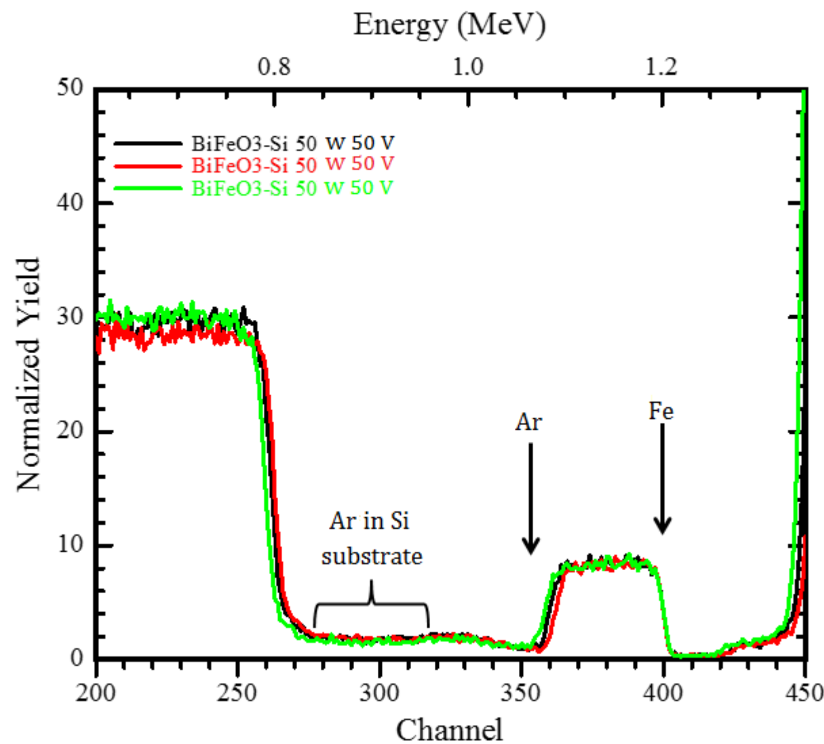

Fig. (b)

Figure 5.11: [a] RBS spectra of BFO deposited with a -50 *V*, -75 *V* and -100 *V* substrate bias voltage. The black, red and green plots depict the experimental data. Fig. [a] is zoomed in from channels 200 to 450 as shown in [b] in order to see the compositional variation among the films.

Table 5.2: Stoichiometry of the BFO layer on (001) Si by RBS

Parameter	Bi ($\pm$1.4%)	Fe($\pm$1.4%)	O($\pm$1.4%)	Ar($\pm$1.4%)	Fe/Bi	O/Bi
30 W	25.5	10.6	63.8		0.416	2.502
40 W	25.5	10.6	63.8		0.416	2.502
50 W	24.4	10.8	64.8		0.443	2.656
75 W	22.9	13.5	63.6		0.590	2.777
-25 V	24.4	14.3	61.2	0.1	0.586	2.508
-50 V	24.9	13.0	60.1	2	0.522	2.414
-75 V	26.5	12.4	57.3	3.8	0.468	2.162
-100 V	27.4	12.0	55.2	5.5	0.438	2.015

From the RBS results it is evident that the Bi content decreases with increasing sputter power, while the content of Fe and O increases. This observation correlates with the bond dissociation enthalpy (energy) of Bi-O (D^0_{298}=337±12.6 *kJ/mol*) and Fe-O (D^0_{298} = 407.0±1.0 *kJ/mol*) as more dissociation of Bi is expected with increasing power. (D°_{298} is the bond dissociation energy at 298 K). Furthermore, the metallization (changes in oxidation state of bismuth) by Ar^+ of Bi on the target surface during sputtering could lead to a lower Bi content in the films [115]. RBS analysis of the BFO films deposited at various substrate bias shows a decrease in the oxygen content with increasing substrate bias; in addition, it appears that a negative substrate bias voltage promotes positive ion bombardment and incorporation; i.e. the argon ions, bismuth and iron ions. This assertion is further supported by the presence of Ar ions in the film, the increased content of which correlates with increasing substrate bias. The depth profiling analysis for the films grown at 50 W rf power with varied deposition times revealed surface enrichments of Fe and O (Fig. 5.12).

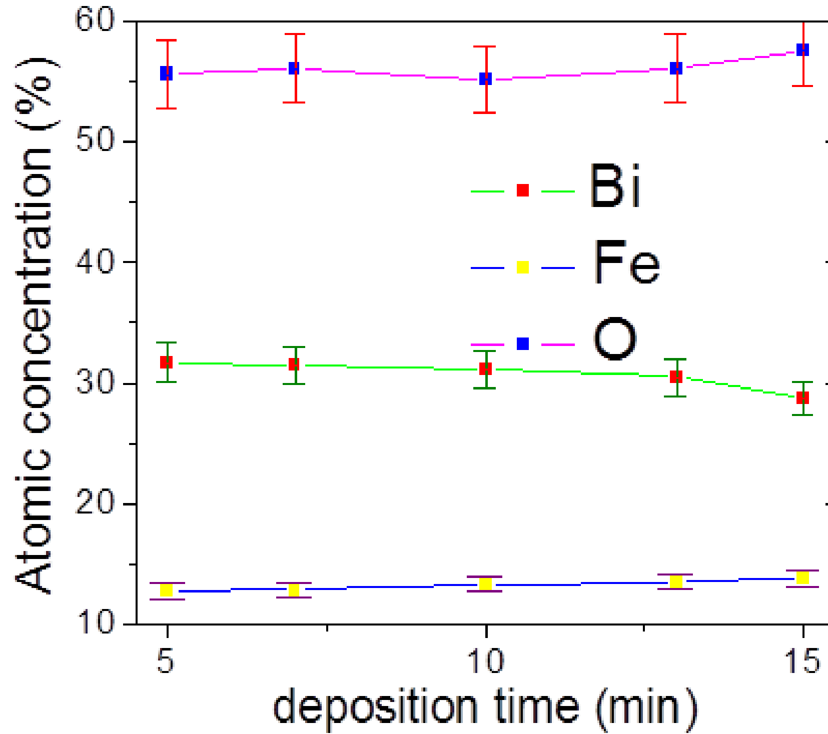

Figure 5.12: Depth profile analysis for films produced at 50 *W* and zero bias as a function of deposition time.

5.4 Density, thickness, surface and interface roughness measurements

A representative X-ray reflectivity spectrum together with the simulated data is presented in Fig. 5.13. The simulations of raw data have been carried out using Leptos software [106]. Fig. 5.13 shows that the total external reflection for $2\theta \leq 0.7°$ is characterized by a nearly constant maximum intensity. The extracted density of the BFO layer (8.14 ± 0.05 gcm^{-3}) is comparable to that of bulk BFO (8.34 gcm^{-3}) [55]. The errors in the measurements are attributed to the experimental uncertainties in the X-ray optical constants and the uncertainties given by the adopted simulation program with precision ranging from 2 to 5.6%. From the analysis of Fig. 5.13, the simulation curve fits well with the experimental one for a layer stack of BFO thin film / $(2\ nm\text{-}SiO_2)/Si$. The film thickness, the density, the surface roughness and the interfacial roughness (the interface between the BFO layer and SiO_2) have been extracted to be (17.55 ± 0.01 nm), (8.15 $\pm$ 0.05 gcm^{-3}), (0.95 $\pm$0.01 nm) and (0.97$\pm$0.01 nm), respectively. The roughness values obtained from XRR are comparable with AFM root mean squared roughness.

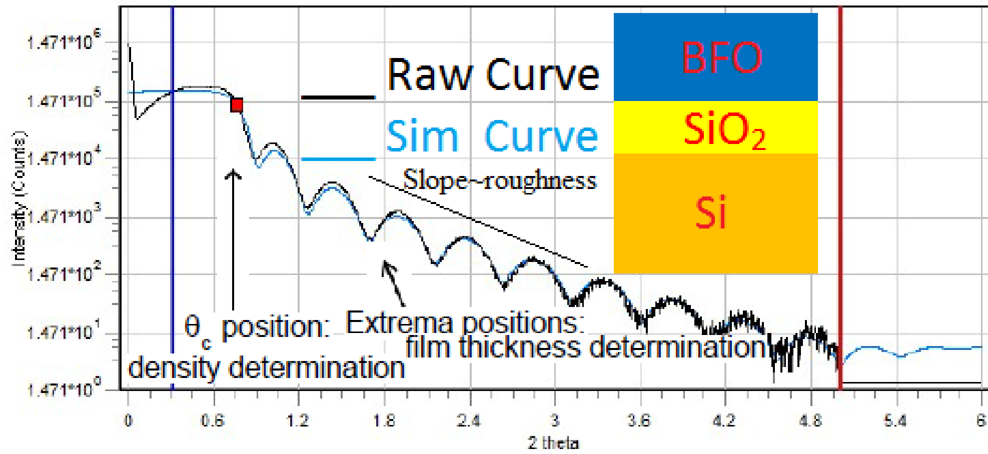

Figure 5.13: Raw (measured) and simulated XRR spectrum of RF magnetron sputtered BFO/SiO_2/Si layer stack with sputter power of 40 *W* and deposition time of 3 *min.*

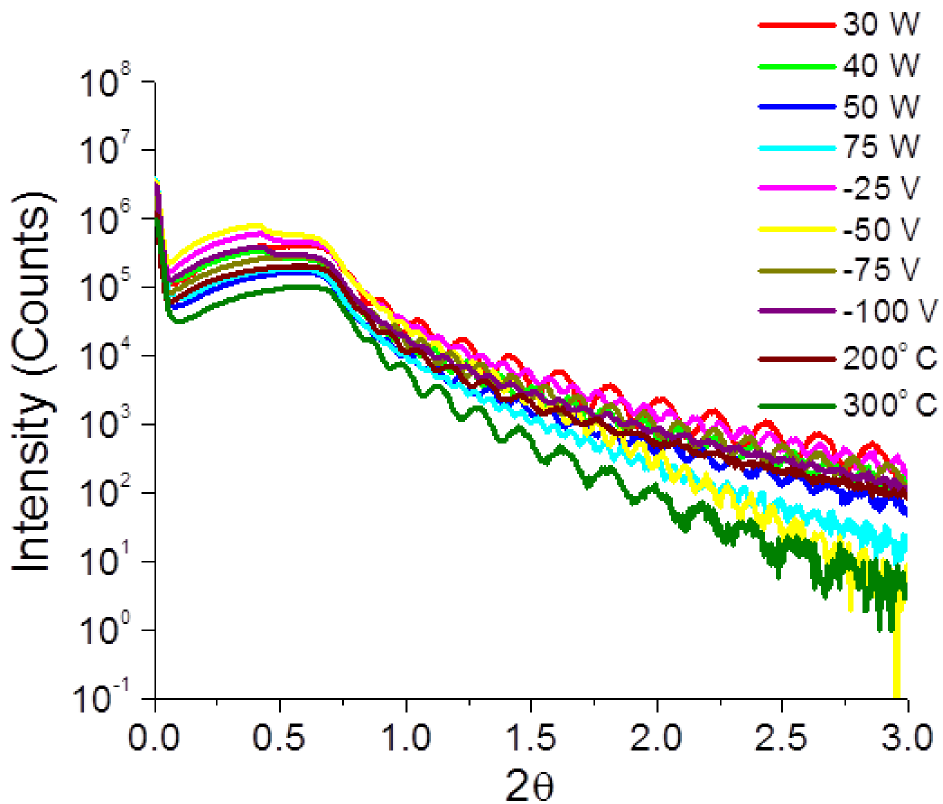

Figure 5.14: XRR spectra of the as-deposited BFO samples with different sputtering power values, substrate bias voltages and temperatures.

Figure 5.14 shows the reflectivity curves of the as-deposited BFO films fabricated at various RF powers, substrate bias and temperatures. It is evident from the Fig.

5.14 that BFO films grown with a substrate bias are denser due to the large values of the critical angle for total external reflection. This also corroborates the RBS data for the biased films and is attributed to the presence of *Ar* in the films. At higher substrate bias (-75 *V*) it is expected that resputtering effects and O^{2-} repulsion leads to lowering of the density of the biased thin films. The films deposited at elevated substrate temperatures are less dense due to the sticking coefficient of Bi (0.49 below 1003 *K*) [116] compared to Fe (1.36 at 508 *K*) [117]. These coefficients contribute to the volatility of Bi leading to a low mass density. The surface and interfacial roughness of the films varied between 0.47 and 3.12 nm, respectively. Table 5.3 presents a summary of density, thickness, surface roughness (from the BFO layer) and interface roughness (from SiO_2-BFO interface) values. Besides the composition variations, the BFO thin films undergo morphotropic phase transitions with increasing temperature.

Table 5.3: Values of the parameters obtained by fitting X-ray reflectivity for films produced under diverse conditions

Parameters	roughness (nm)	thickness (nm)	density(gcm^{-3})
30 W	0.89	40.52	8.14
40 W	0.90	56.44	7.92
50 W	1.30	66.86	7.71
75 W	1.18	117.36	7.61
-25 V	0.72	84.98	8.13
-50 V	0.94	70.29	8.46
-75 V	0.86	60.89	8.01
-100 V	0.83	58.38	8.10
200°*C*	0.74	53.02	7.71
300°*C*	1.21	43.21	7.51
400°*C*	2.09	39.38	7.36
600°*C*	2.92	38.22	6.56

The changes in density correlate with the variation of the Bi content in the films and the Ar^{+} bombardment, as illustrated in Figure 5.15. The variations in density at 25.5 at % of Bi is associated with the different sputter powers used. At 30 *W* RF power the film density is determined to be 8.14 gcm^{-3} for a Bi composition of 25.5 at %. On the other hand a film deposited at 40 *W* RF power yields a lower density of 7.92 gcm^{-3}.

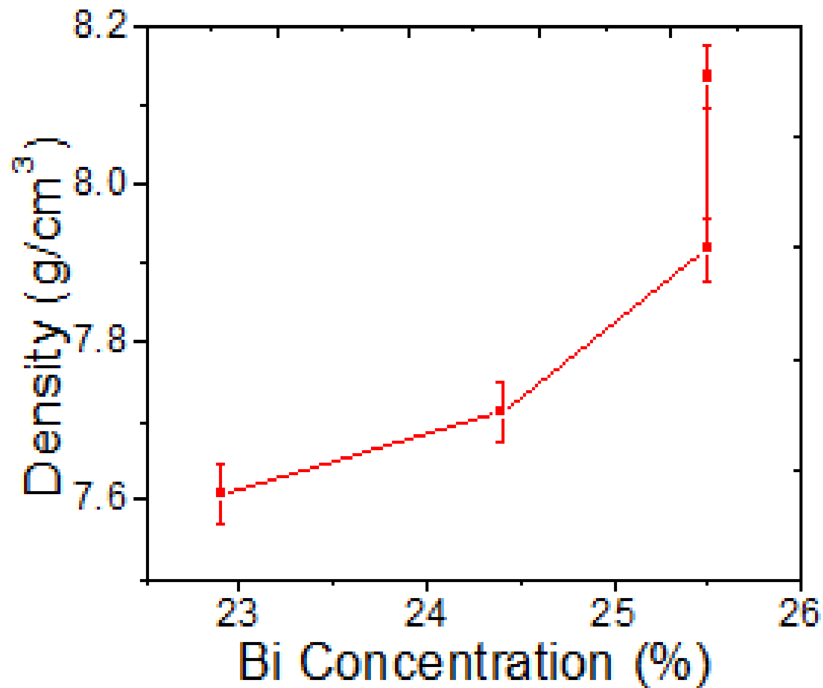

Figure 5.15: Graph of bismuth density versus concentrations of the films as determined by RBS. The films were prepared at different sputter powers and hence have different densities. The bismuth content of films fabricated at 30 *W* and 40 *W* is the same (25.5 at %) but the films have different densities.

RBS studies revealed that substrate bias yields films with higher Bi content and very dense granular microstructure as observed from AFM and cross-sectional FESEM analysis. The reduction in Bi content with increased sputter power is also shown in Fig. 5.16. The concentration of Bi in the films decreased monotonically with sputter power, from 25.5 to 22.9 at. %. The surface roughness values measured with both AFM and XRR are in good agreement as shown in Tables 5.1 and 5.3. Moreover, the surface roughness increases with increasing in substrate temperature due to the grain growth in BFO films.

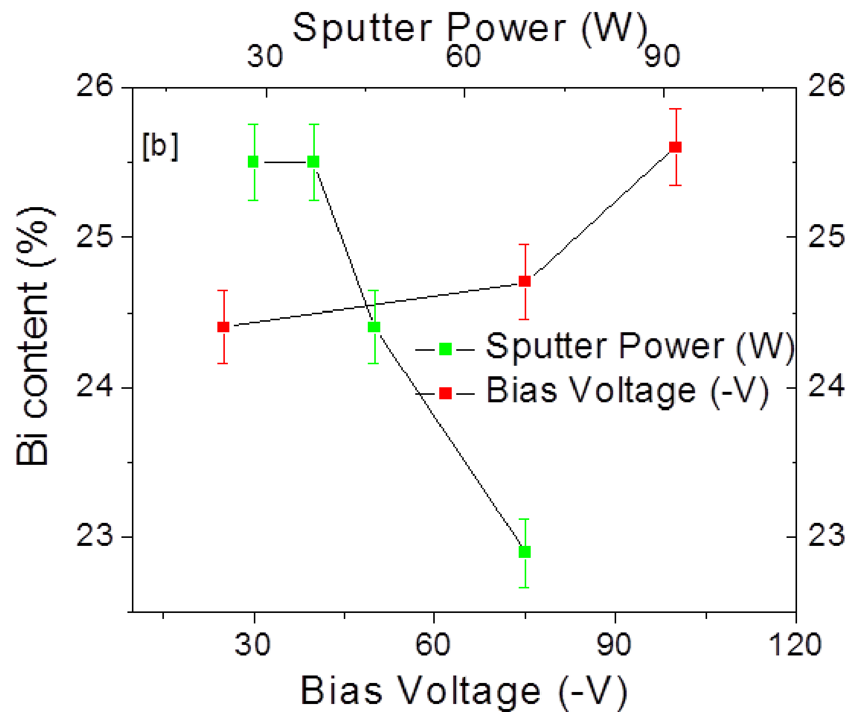

Figure 5.16: Bismuth contents in RF substrate biased and with different sputter power films as determined from RBS measurement.

The surfaces of the BFO samples become dense, smooth-continuous structures as the bias voltage is increased, which is a result of increased surface diffusivity of BFO ad-atoms to occupy near low potential sites. The film thickness increased linearly with the deposition time under the same sputter conditions, suggesting that the deposition rate is independent of exposure time.

5.5 Phase identification studies

The GIXRD patterns were collected in the range $20^\circ \leq 2\theta \leq 60^\circ$ at a glancing angle of 0.7°. The crystalline phase and grain size were determined from the peak positions and the Debye-Scherrer equation (Table 5.4). The GIXRD data of samples grown with different sputtering power are presented in Figure 5.17. Only two broad humps corresponding to an amorphous phase are observed for films grown at 30 W. For higher sputter power it is observed that nano-crystalline grains could be present in an amorphous matrix due to the broad peaks at higher 2θ. The degree of crystallinity in BFO thin films is observed to increase with increasing sputter power. Using Scherrer's formula, the grain sizes of BFO films deposited at 50 *W* and 75 *W* were determined as 20 *nm* and 30 *nm*, respectively. The grain size of

the films are generally found to increase with increasing substrate temperature up to 400°C; then a reduction in grain size occurs at 500°C and 600°C as depicted in Figure 5.18. This reduction in grain size at higher T is attributed to possible surface melt crystallization. Similarly, in Fig. 5.19 the grain size increases as sputter power increases and it is also observed that grain growth varies with negative substrate bias.

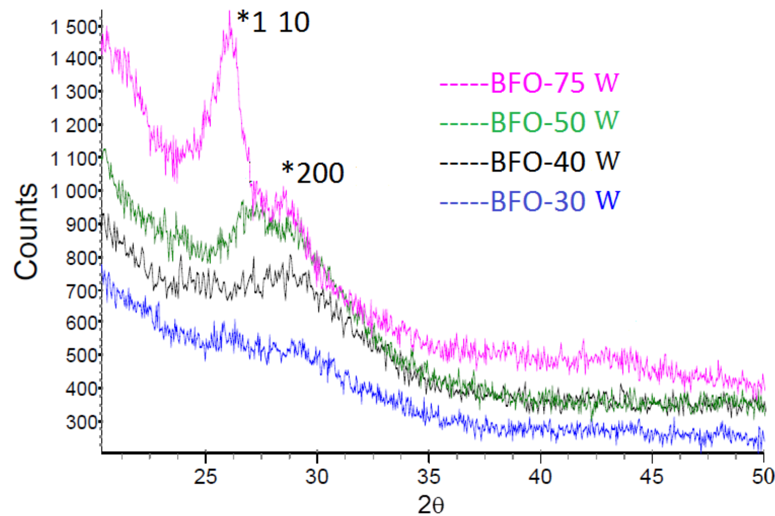

Figure 5.17: Room temperature GIXRD patterns from BFO thin films deposited with different RF sputter powers. All films were deposited with the same sputtering conditions (13 sccm Ar flow, deposition time 15 *min)*.

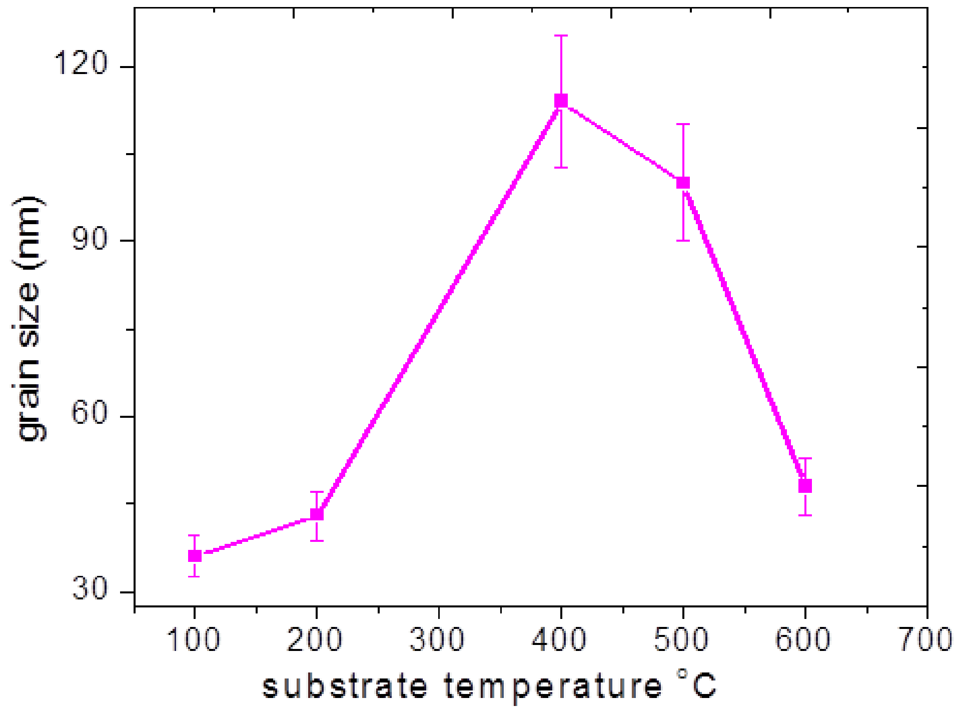

Figure 5.18: Variations of grain size with substrate temperature.

As can be seen from the AFM images of Figures 5.1[a]-[b] and 5.2 [a]-[b], films produced at 30 *W* are very dense and have a compact structure (with no defined grain boundaries) as compared to those produced at 40 *W*, 50 *W* and 75 *W*. All the films show zone I type of microstructure with dense morphology owing to inadequate adatom mobility. A significant microstructure change for BFO films produced with 50 *W* and 75 *W* sputter power is evident from the AFM and FESEM images (Figures 5.2 [a]-[b] and Figures 5.7 and 5.8, respectively). An increase in sputter power results in the reduction of impurity phases and the stoichiometric ratio of Bi and O [118], which lead to an increase of the crystallinity of the samples, as shown in the distinct Bragg peaks of the BFO film deposited at 75 *W* (Fig. [5.17]).

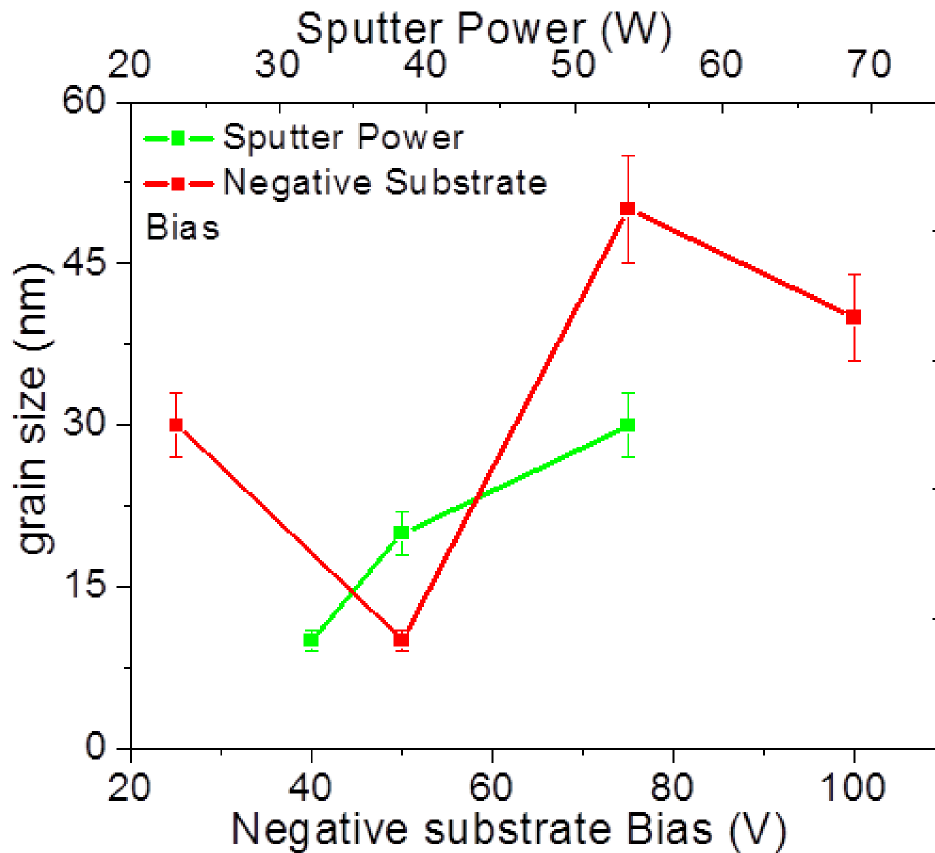

Figure 5.19: Variations of grain size with sputter deposition parameters.

Applying a bias voltage (negative) to the substrate extracts Ar^+ ions from the plasma to the substrate leading to the incorporation of Ar^+ ions into the film. So the grain growth kinetics can be determined by surface (2D) nucleation and by the effect of negative substrate voltage. The biasing reduces the number of O ions. The Ar^+ ions are attracted to the substrate and these ions are scattered off Bi ions and Fe adatoms, thereby lowering the deposition rates due to re-sputtering, as observed from the thicknesses of the films in Table 5.3. From the AFM images of Figures 5.5[a]-[b] and Figures 5.6 [a]-[b], the effect of substrate bias voltage -25 to -100 V on the microstructure are clearly observed as the enhanced growth of mosaic-like structures with increase in bias voltage. At -25 V (Fig. 5.5 [a]) the BFO films exhibit a very fine grain structure. As the bias voltage increases to -50 V (Fig. 5.5 [b]), the structure changes to a dense smooth-continuous structure. This is a result of the increased surface diffusivity of Bi ad-atoms due to Ar^+ bombardment that leads to momentum transfer in order to accommodate low potential sites. At higher substrate bias of -75 V and -100 V, re-sputtering of the growing film competes with Ar^+incorporation, leading to mosaic like grains. Re-sputtering increases heterogeneous nucleation sites which impedes grain boundary motion. Thus, the films

become thinner, smoother and fine-grained with an increase of bias-voltage, generally resulting in the degradation of the film crystallinity. This is also confirmed from the GIXRD diffraction spectra as shown in Fig. 5.20. Despite the increase in ion-bombardment energy with increase in substrate bias voltage, the films produced with high bias voltage show a decrease in crystallinity. Films deposited at -100 V show a reduction in crystallinity due to re-sputtering and possible energy dissipation effects of Bi, Fe and O adatoms from the growing surface. For films fabricated with -25 V, -50 V and -75 V negative substrate voltage, the preferred growth is in the (*020) plane, as the surface energy is dominant [91]. The inclusion of Ar^+ ions in the films (as also confirmed by the RBS study, Table 5.2) induces compressive stresses in the film, hence producing point defects and dislocations loops as seen in the AFM images in Figures 5.5 and 5.6. The macro strain developed in the films is tabulated in Table 5.4.

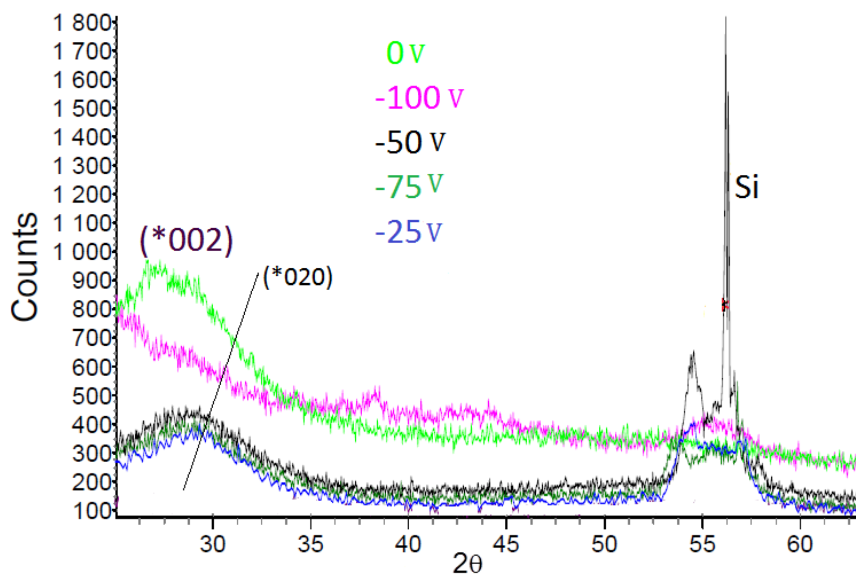

Figure 5.20: GIXRD patterns of BFO films with various substrate negative bias voltage. All films were deposited at the same sputtering conditions.

Table 5.4: Effect of bias voltage and temperature on lattice parameters and macro strain in BFO films

$Parameters$	GIXRD$Peak$ (2θ)	$Calculated$ $d-spacing$ Å	$\varepsilon(macro$ $strain)$	$Crystallite$ $size(nm)$
30 W	29.52			amorphous
40 W	29.37	3.038		~10
50 W	28.50	3.129		~20
75 W	28.75	3.108		~30
-25 V	28.92	3.084	-1.125E-3	~30
-50 V	28.94	3.083	-2.520E-3	~10
-75 V	28.78	3.099	-2.384E-3	~50
-100 V	28.30	3.150	-2.740E-3	~40
100° C	29.16	3.065	-1.808E-3	~36
200° C	29.10	3.066	-1.926E-6	~43
400° C	28.75	3.102	-1.054E-6	~114
500° C	28.33	3.148	-2.034E-6	~100
600° C	29.46	3.029	3.483E-3	~48

Figure 5.21 shows the GIXRD pattern for BFO films deposited at a substrate temperatures of 100°C, 200°C, 400°C, 500°C and 600°C at 50 W. Distinct crystalline peaks appear due to in-situ high temperature deposition, which supports grain growth in BFO films. The peaks shown in the GIXRD patterns at $2\theta = 32.44°$, $2\theta = 47.03°$ and $2\theta = 53.01°$ and are indexed to (*200), (*111) and (*310) reflections. All the films grown with substrate temperatures of 400°C and 500°C show better crystallinity (grain growth) compared to the films fabricated at varying substrate bias voltage and sputter power. Fig. 5.21 shows that at elevated temperature crystallization with large grain size is attained. However, at 600°C the crystallization in the films reverts to sublimation contrary to what is expected from the Structural Zone Model (SZM). This is due to surface melting and is associated with the formation of a stabilized quasi-liquid film on the crystalline surface below the crystal melting point ($T_m = 630°C$) [88]. The compositional variations in films produced with varying substrate temperatures cause morphotropic phase transitions. Hence, film growth in the temperature regime 200°C - 400°C leads to a tetragonal phase which transitions to a rhombohedral phase at 600°C.

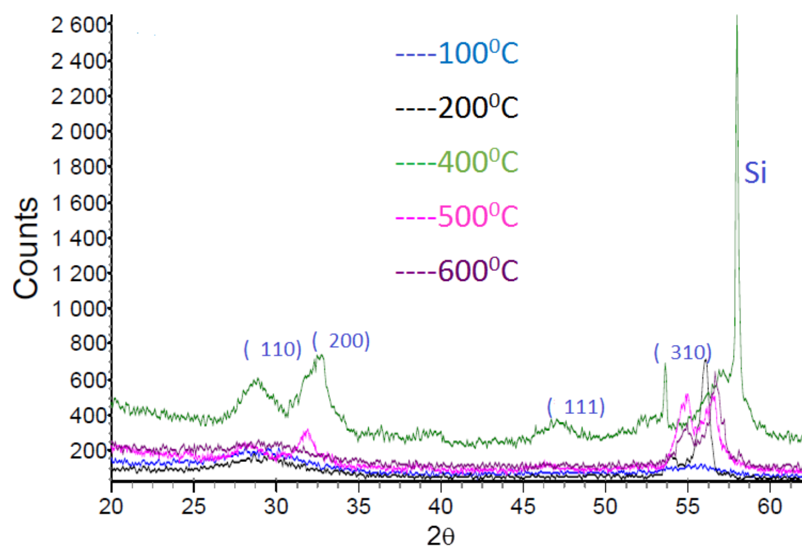

Figure 5.21: The GIXRD patterns of BFO films produced at various substrate temperatures. All the films were deposited at 50 *W* for 15 *min*.

Chapter 6.

Results & Discussion: Surface Brillouin Scattering studies

In this chapter the dynamics of surface acoustic waves of BFO thin films grown under various conditions is presented. The role of ad-atom energy on the elastic constants and microstructure is discussed in this chapter. The chapter ends by highlighting the evidence of stress evolution using the elastic constants.

6.1 Measured and simulated SBS spectra for $BiFeO_3$ thin films

Many SBS measurements and simulations have been done on the BFO/Si film substrate system for the investigation of the dispersion of surface acoustic waves propagating in the film in the range of $k_{||}h$ between 0.7 to 15 (where $k_{||}$ is the wave vector parallel to the film surface and h is the film thickness). The dimensionless parameter $(k_{||}h)$ represents the product of the film thickness from 30 nm to 652 nm with $k_{||} \approx 0.023\ nm^{-1}$. All the films were deposited under the same conditions and with sputter powers of 50 W and 75 W without biasing and also with a negative bias voltage of -50 V at 50 W. The values of $k_{||}h$ have been calculated at a constant incidence angle θ_i at 71.5° (in which the light is scattered with maximum efficiency) and with the respective film thicknesses as tabulated in Table 6.1.

Table 6.1: $k_{||}h$ values for the various film thicknesses of BFO/Si

$h(nm)$	30	91	109	228	319	578	602	652
$k_{||}h$	0.7	2.1	2.5	5.25	7.33	13.3	13.85	15

The combined results of the dispersion curves of all the films produced at 50 W having $k_{||}h$ in the range 0.7 to 15 with the various film thickness are exhibited in Figure 6.1. The error bars in the dispersion curves are mainly due to the inaccuracies in identifying the peak positions in the Brillouin spectra. The frequency shift f is often identified by using a Lorentzian best-fit procedure. Therefore, the uncertainty σ_f is related to the best-fit procedure and it is only dependent on the peak position. As seen from the dispersion curves of figure 6.1, all of the data for different film thicknesses merge quite well, except at one point. Thus it can be concluded that the films don't exhibit pronounced layered substructure i.e. can be regarded as a homogenous film-substrate system. For homogeneous films the surface acoustic waves depend on the product of $k_{||}$ and the film thickness h [64]. Hence, the dispersion curves of the acoustic waves is studied by changing the dimensionless product $k_{||}h$.

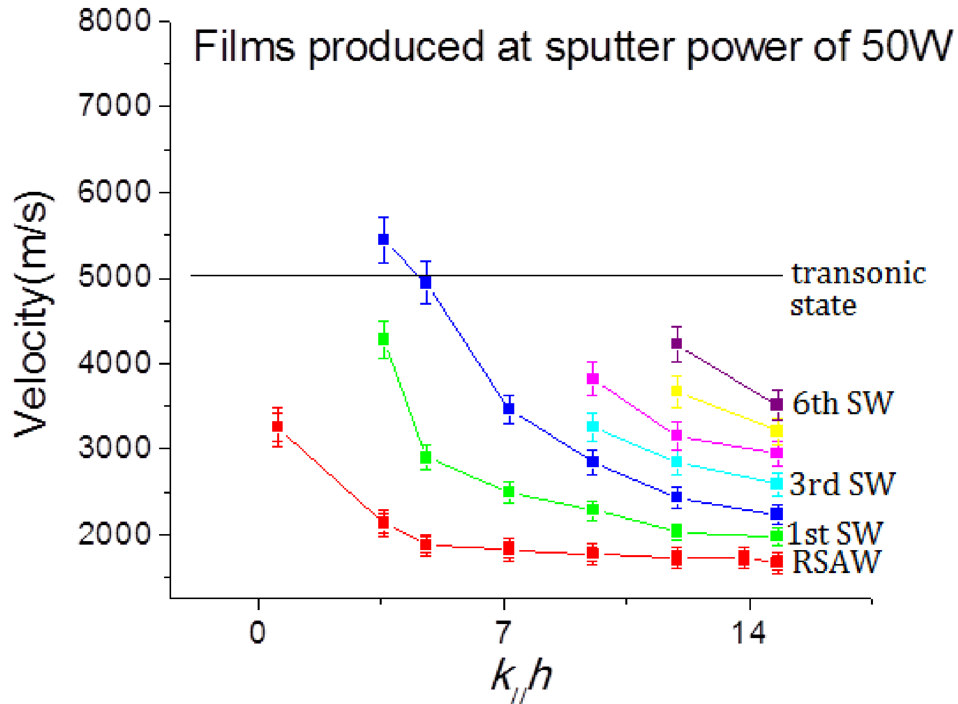

Figure 6.1: Velocity dispersion curves of BFO films with thickness h ranging from 30 to 652 nm. This dispersion was found by varying film thickness while keeping $k_{||}$ constant.

The Rayleigh surface acoustic wave (RSAW) is the surface propagating mode with the lowest velocity. Its velocity remains the same for the thickest films, which means that the Rayleigh mode is not affected by the substrate and demonstrates the true elastic properties of the film material (i.e as $h \to \infty$, all propagating modes converge to that of the Rayleigh mode). On the other hand, if the film thickness approaches zero i.e. $h \to 0$, the Rayleigh mode becomes equal to the Rayleigh mode of the

silicon substrate, which is 5074 ms^{-1}. Our film-substrate system is a slow-on-fast system such that the BFO layer has an effect of reducing the Rayleigh mode frequency compared to that of the substrate. The propagation of higher order modes known as Sezawa waves (SWs) are observed in this film-substrate configuration. These higher order modes exist in the film-substrate system whenever the transverse velocity of the substrate (V_T) is greater than that of the transverse velocity of the layer. True Sezawa waves are surface waves localized in the film. In our case we have observed that the transverse velocity of the silicon substrate is $V_{TS} = 5074$ ms^{-1} and the transverse velocity of the BFO layer is $V_{TL} = 1720$ ms^{-1}. Therefore, below the transonic state (discrete spectrum), which is known as the subsonic state or region, we have the presence of two propagating waves in the system. These are the Rayleigh surface acoustic wave that is characteristic of surface modes of the layer and the higher order vibrational modes called Sezawa waves. These modes are known as film modes. As observed from Fig. 6.1, the dispersion curves of the phase velocities of these two types of modes decrease with increasing $k_{\parallel}h$. For phase velocities above the transverse velocity (V_{TS}) of the substrate (which can be considered as the lowest bulk velocity in a given direction and polarization) or above the transonic state (continuous spectrum or hypersonic state), there are propagating substrate bulk modes which can be considered as the continuation of the Sezawa modes into this region and exist as attenuated excitations called pseudo-Sezawa waves (pSWs) or will show up as a resonance [61]. The simulation of the G_{33} component of the Green's function at $x_3 = -h$ of the sagittal coordinates of the free surface of the film gives the scattered mode intensities for a given value of $k_{\parallel}h$, as shown in Figure 6.2. For G_{33} calculations, we have used the elastic constants of $C_{11} = 184$ GPa, $C_{12} = 141$ GPa , $C_{44} = 21$ GPa and density $\rho = 7.83$ gcm^{-3}.

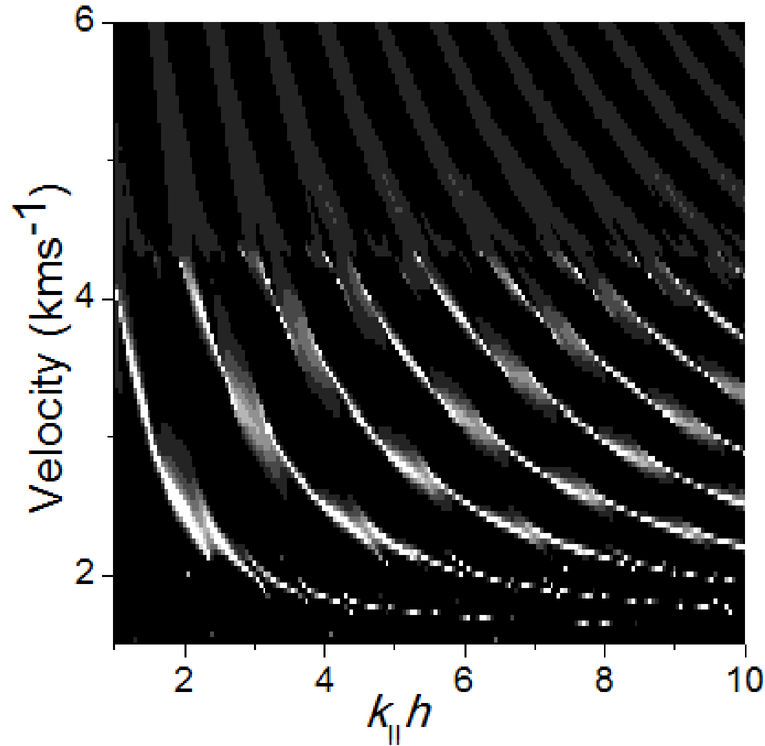

Figure 6.2: The simulated cross sections of an elastodynamic Green's function calculation using the G$_{33}$ component.

The elastodynamic Green's function determines the surface displacement amplitude of the phonons and thereby predicts the SBS spectra. The cross sections of the calculated curves of Figure 6.2 are normalized for the discrete and the continous ($v_T > 5074$ ms^{-1}) spectra for each value of $k_{||}h$. Since the thin film is opaque, the cross sectional contribution to the surface Brillouin spectra are dominated by the scattering from the surface ripple mechanism, which is linearly related with the power spectrum of the vertical displacement component at the free surface. The low cross sections seen at around $v = 5074$ ms^{-1} are due to the longitudinal character of the partial waves and are related to the longitudinal sound velocity of the material parallel to the film. Many damped resonant excitations are present in the continuous spectrum as shown in Figure 6.2. Figure 6.3 shows a representative measured surface Brillouin spectrum of films having thickness of 318 nm, for which $k_{||}h = 7.33$, taken at an incident angle of $\theta_i = 71.5°$. The spectrum exhibits the frequency doublets, Stokes and anti-Stokes, and the peaks of the Rayleigh surface acoustic wave (RW), seven Sezawa waves (SWs), one pseudo Sezawa wave (pSWs); (pSWs shows surface wave character, but its energy leaks into the substrate and hence its lifetime is reduced), resonance, and one high-frequency pseudo surface mode (HFPSM)[119].

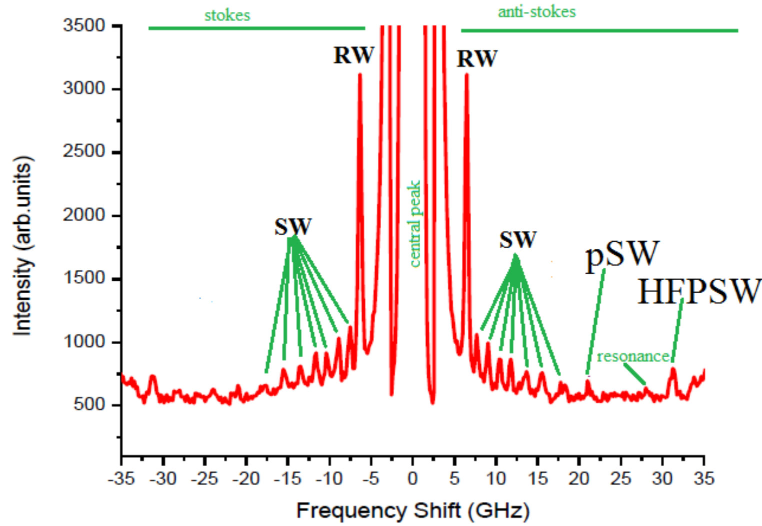

Figure 6.3: Typical Brillouin spectrum of the 318 nm BFO thin film taken at an incidence angle of 71.5°. The central peak is the result of elastically scattered light, hence it is unshifted in frequency. In the transmission range from ±6 to ±35 *GHz*, indicated by the solid lines, the Rayleigh mode, seven Sezawa modes, pseudo Sezawa mode and high-frequency pseudo surface modes are clearly visible.

Figure 6.4 shows the representative measured surface Brillouin spectra for films with thicknesses $30-652$ *nm* fabricated at 50 W and with no substrate bias. The spectrum of inelastically scattered peaks consists of the Rayleigh mode, Sezawa modes, pseudo surface modes, resonances and high-frequency pseudo surface mode (HFPSW). The peak at zero represents the elastically scattered laser beam. The elastically scattered peak is modified by the effect of the shutter. In the spectrum of the thinner film, i.e. $k_{\|}h = 0.87$ the influence of the substrate becomes discernible due to the presence of the mode at $\triangle f = 15.8$ GHz. For $k_{\|}h > 2.1$, it is observed that more modes appear at higher frequency shifts (> 6.66 GHz), which means that as the film thickness increases the film-substrate system tends to support one surface mode (RSAW) and several film modes (SWs). Moreover, a slow-on-fast system is characterized by having a stiffening effect on the SAWs velocity. For $k_{\|}h \geq 2.1$ the velocity of Rayleigh surface acoustic waves (RSAW) decreases at the expense of the increasing of Sezawa waves. As $k_{\|}h$ increases the RSAW velocity increases at $k_{\|}h$= 0.87 and then decreases until it levels off at 1750 ms^{-1}.

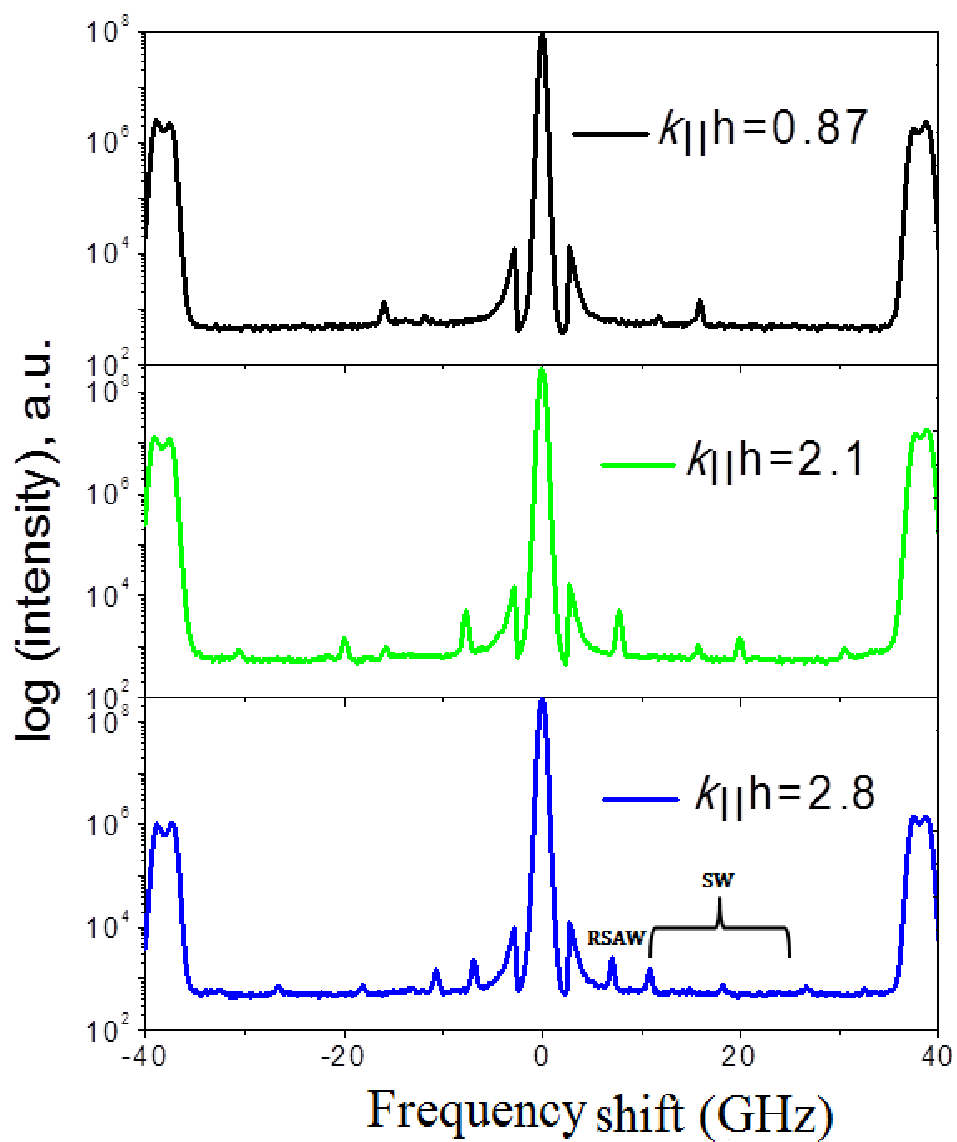

(Fig. 6.4 [a]) $k_{\|}h = 0.87$ to $k_{\|}h = 2.8$

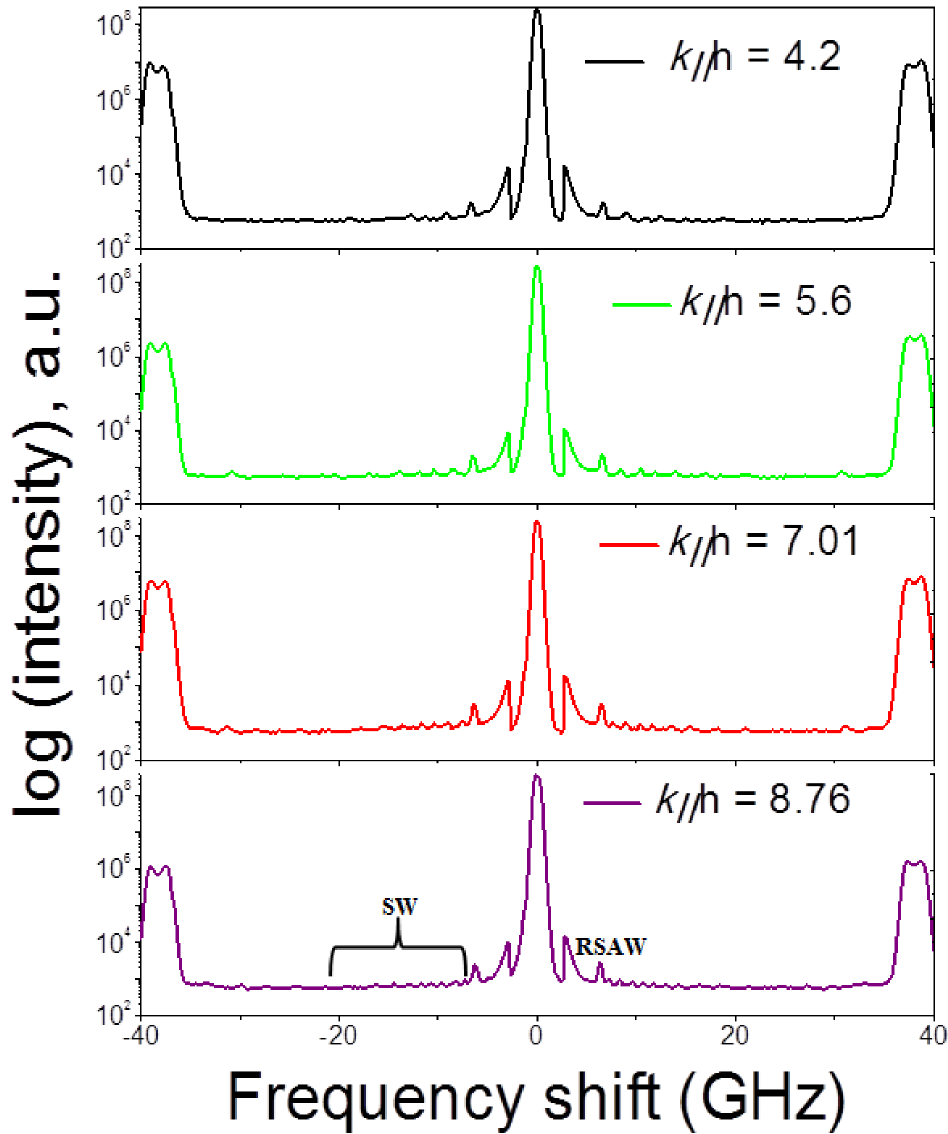

(Fig. 6.4 [b]) $k_{\parallel}h = 4.2$ to $k_{\parallel}h = 8.76$

Figure 6.4: [a and b] Representative measured SBS spectra of intensity as a function of the frequency shift for BFO films produced at 50 W sputter power on a silicon substrate.

Measured surface Brillouin spectra of films having the same thickness but deposited at 50 W, 75 W and with -50 V substrate bias voltage at 50 W sputter power are illustrated in Figure 6.5. It is clearly exhibited in the spectra that the first dominant peak for all of the spectra is the RSAW. The velocities of the RSAW increase with increasing sputter power. This leads to an increase of the phase velocities of the Sezawa modes at low $k_{\parallel}h$ range. The reason for this might be that films made with low sputter power might contain a more compliant layer in the film's structure. The variation of the peak positions of the different modes of surface Brillouin spectra

shown in Fig. 6.5 might possibly be attributed to variations in the microstructure of the films and the presence of density defects in the films (the densities of films produced at 50 *W*, -50 *V* & 50 *W* and 75 *W* are 7.83, 8.13, and 7.71 gcm^{-3}, respectively).

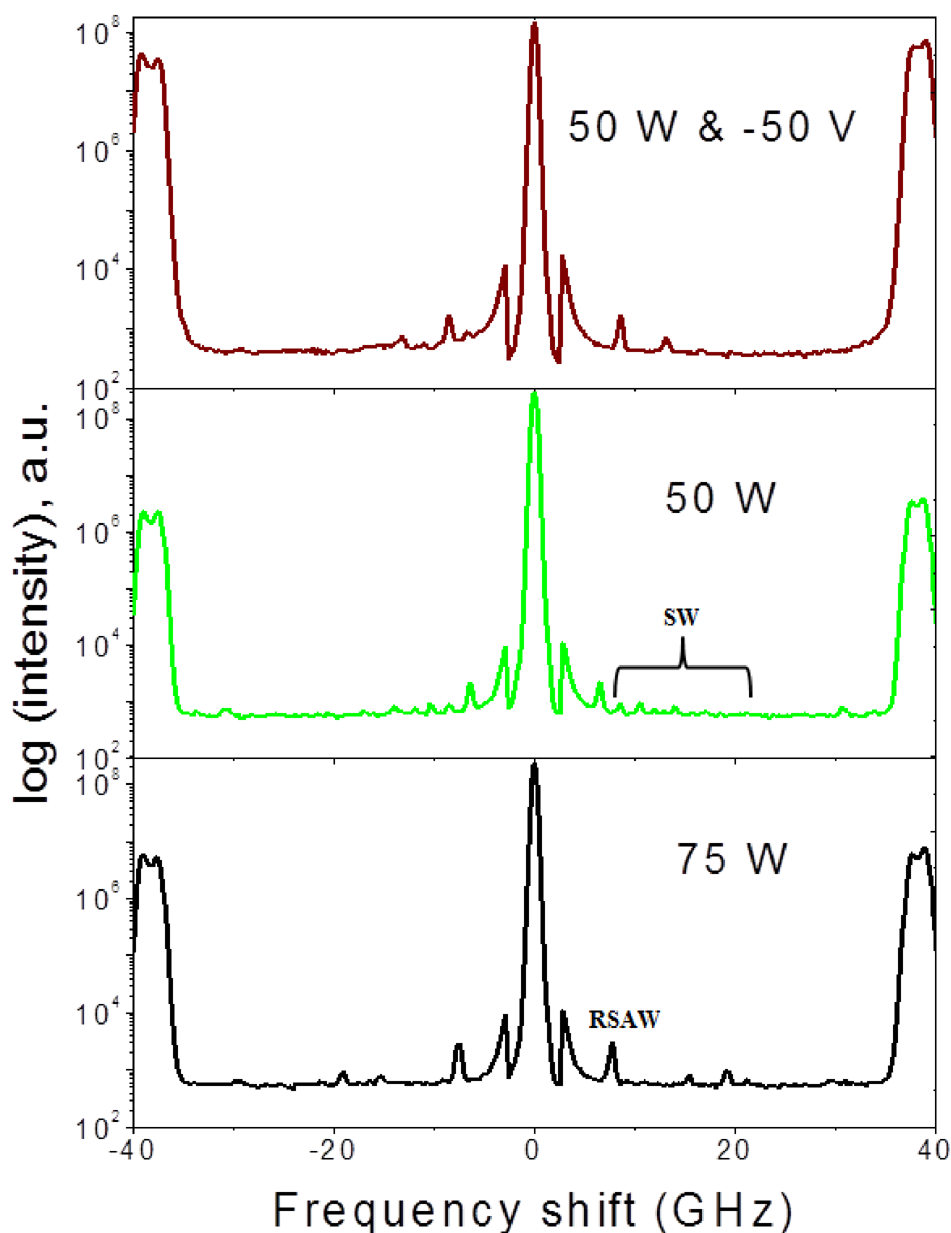

Figure 6.5: Representative measured SBS spectra of intensity as a function of the frequency shift for BFO films produced on a Si substrate at 50 *W* with a substrate bias of -50 *V*, 50 *W* with no substrate bias and 75 *W*, respectively. All the films have the same thickness of 228 *nm*.

6.2 Derivation of effective elastic constants of BFO thin films

The discrete part of the spectrum (the region of the dispersion curves below the transonic state) is used to derive the elastic constants by fitting the experimental (measured) data to the simulated (calculated) acoustic phonon wave velocities. The discrete part of the spectrum of the propagating modes (Rayleigh and Sezawa modes) provides sufficient information to extract a full set of the elastic constants. The calculated dispersion curves of the discrete spectrum of the propagating modes are obtained from a least squares fit to the experimental data, using the elastic constants as free parameters. Figures 6.6, 6.7 and 6.8 are the dispersion curves of the calculated and measured data in which the solid squares and the red circles indicate the fitted and measured data points, respectively. The error bars are due to the uncertainities in determinating the peak positions of the propagating modes from measured SBS spectra. Some of the data points in these figures do not fit the simulated data exactly, due to film inhomogeneity. Fitting the dispersion curves is a physical inversion problem and the best fit is obtained by a least-squares minimization procedure given by [72]:

$$\chi^2(C_j) = \sum_i (\frac{v_i^{calc}(C_j) - v_i^{meas}}{\sigma_i})^2 \tag{6.1}$$

where σ_i is the variances of each v_i^{meas}, $\chi^2(C_j)$ is chi square minimization in the distribution of C_j, v_i^{calc} is calculated velocities and v_i^{meas} is measured velocities. The best fit of the dispersion curves are characterized by a minimum in the χ^2sum and the elastic constants used to get this minimum are considered as the elastic constants of the thin films. Of course, there is no global or standard sum minimum as it depends on the amount of data provided.

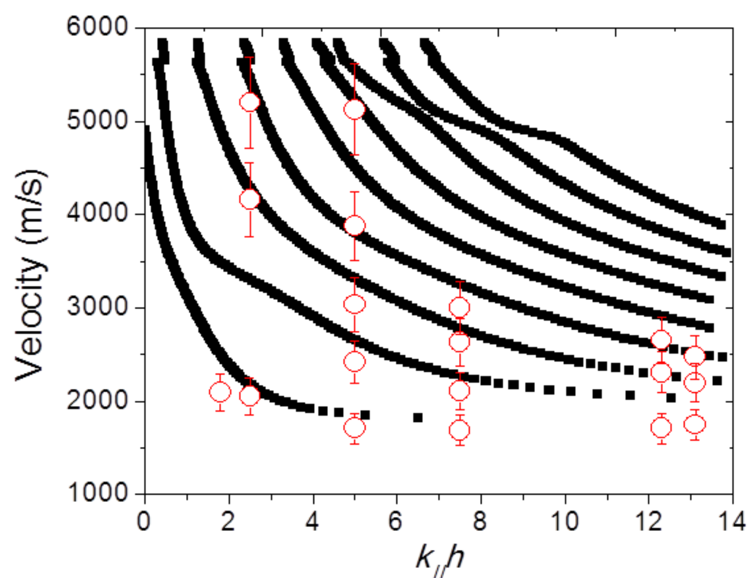

Figure 6.6: Dispersion curves (measured and calculated) of the pristine films produced at 75 *W* and zero substrate bias voltage. The circles are the measured raw data.

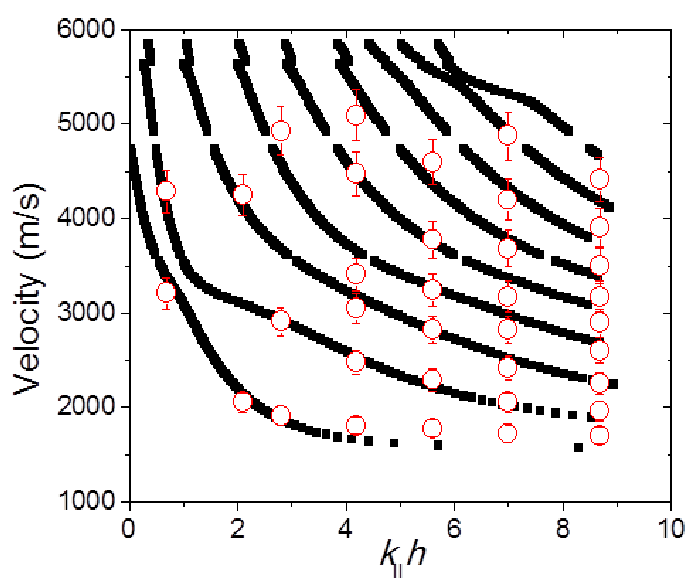

Figure 6.7: Dispersion curves (measured and calculated) of the pristine films produced at 50 *W* and zero substrate bias voltage. The circles are the measured raw data.

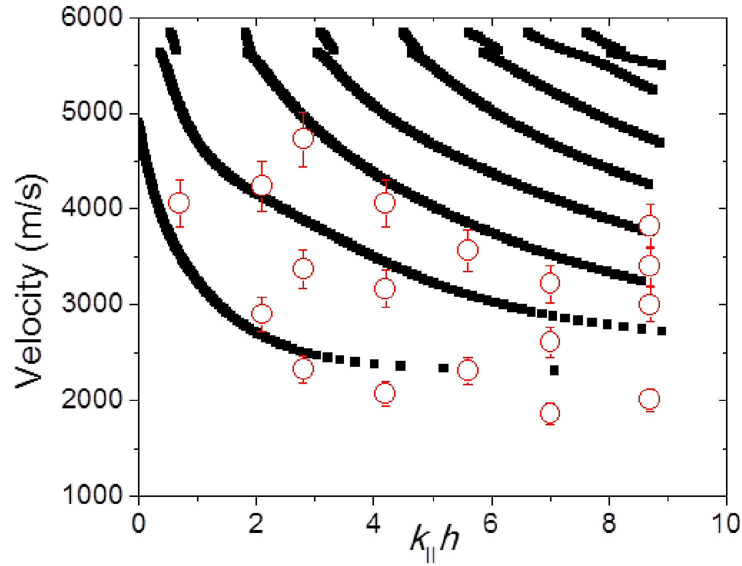

Figure 6.8: Dispersion curves (measured and calculated) of films fabricated at 50 *W* and negative substrate bias voltage of -50 *V*. The circles are the measured raw and the solid squares represent the calculated best fits to the raw data.

As shown in the Figure 6.8, the dispersion curves contain more discontinuities among the measured data points for films fabricated with -50 *V* substrate bias voltage. The set of the effective elastic constants was recovered in a routine least squares fitting by assigning a correct mode order using an initial set of parameter values for the elastic constants and density of the films. A FORTRAN source code was used to extract the effective elastic constants from the measured Rayleigh surface wave (RSAW) and Sezawa wave velocities and their corresponding $k_{||}h$ values. The measured XRR densities were used in the simulations and these values tabulated in Table 5.3. The elastic stiffness constants of the films extracted from the best fits are tabulated in Table 6.2. For the silicon substrate we have used the values: mass density $\rho = 2.332\ gcm^{-3}$, $C_{11} = 165.7$, $C_{12} = 63.9$, and $C_{44} = 79.6\ GPa$, respectively [64].

Table 6.2: Effective elastic constants of BFO films obtained from the best fit of the calculated to the measured phonon dispersion curves, under the assumption of homogeneous films.

parameters	Density (g/cm^3)	$C_{11}(GPa)$	$C_{12}(GPa)$	$C_{44}(GPa)$
50 W	7.83±0.05	184±10	141±8	21±1
50 W &-50 V	8.13±0.05	222±20	124±11	49±4
75 W	7.71±0.05	163± 15	106±10	28±3

The Brillouin scattering cross section spectra were simulated using the Green's function and the derived elastic constants, in order to compare with experimentally measured surface Brillouin spectra as shown in Figures 6.9-6.11 for film thicknesses 109 *nm*, 228 *nm*, and 91 *nm*, respectively. The simulated and the measured spectra show a good agreement. For high thickness values there are more modes supported in the films, as observed in Fig. 6.10.

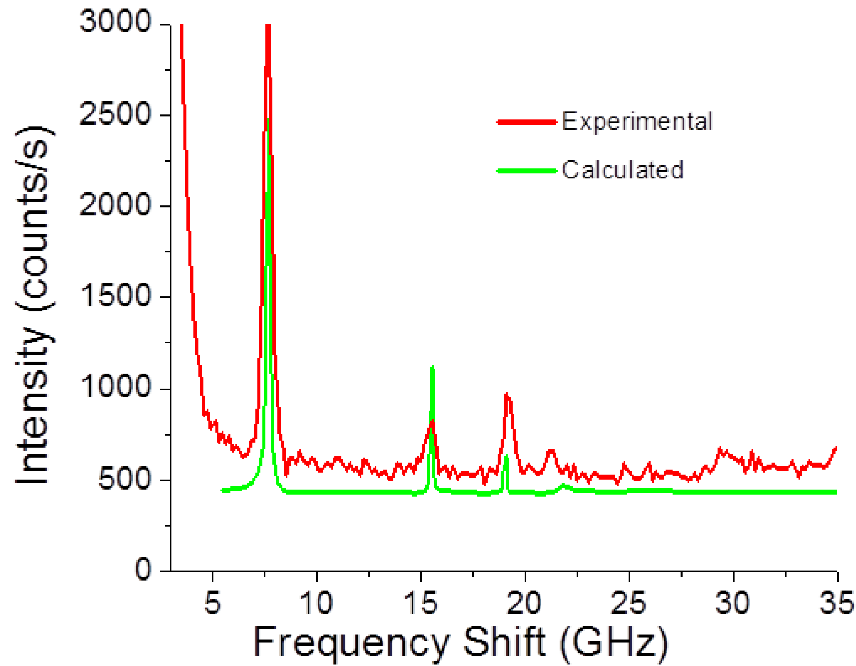

Figure 6.9: Simulated and measured surface Brillouin spectra at 71.5° incident angle for a 109 *nm* BFO film fabricated at 75 *W* on a silicon substrate.

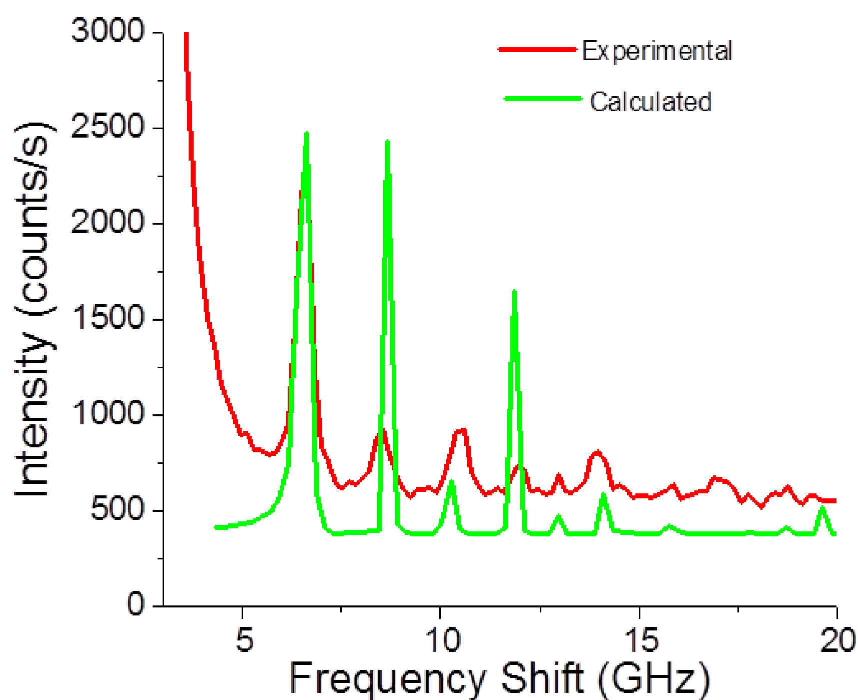

Figure 6.10: Simulated and measured surface Brillouin spectra at 71.5° incident angle for a 228 *nm* BFO film fabricated at 50 *W* on a silicon substrate.

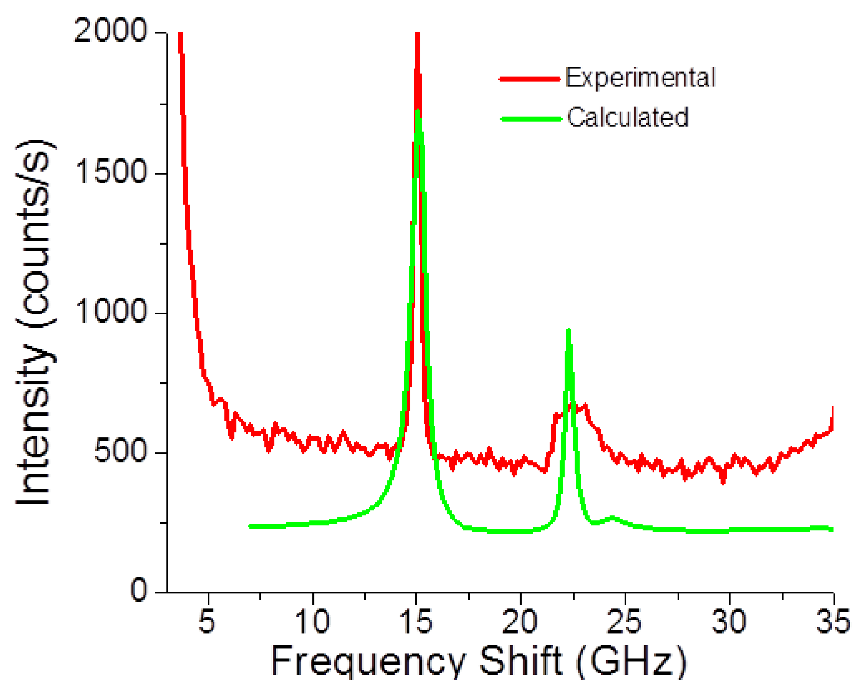

Figure 6.11: Simulated and measured surface Brillouin spectra at 71.5° incident angle for a 91 *nm* BFO film fabricated at of 50 *W* and -50 *V* negative substrate bias voltage on a (001) silicon substrate.

6.3 Stress evolution

There are many mechanisms that could induce intrinsic stress in a film during growth [120]. The intrinsic stress evolution during our BFO thin film growth was governed by Ar^+ incorporation (dynamic process), defects (i.e. vacancies, adatoms and ledges) and nanocrystallite formation in the growing amorphous thin films upon applying a negative substrate bias voltage. The presence of the incorporated Ar^+ has been confirmed by Rutherford backscattering measurement (RBS). Surface Brillouin Scattering has been used to investigate the stress evolution during the film growth. Figure 6.12 shows the surface acoustic dispersion curves of thin films produced at a sputter power of 50 W with zero substrate bias (the triangular data points) and for films produced at the same sputter power but with a negative substrate bias voltage of -50 V (the circular data points). This study on these films is merely intended showing stress evolution upon Ar^+ incorporation. The effect of film thickness was minimized for the pristine (0 V) and the biased film (-50 V) as their XRR values were similar for the same deposition time.

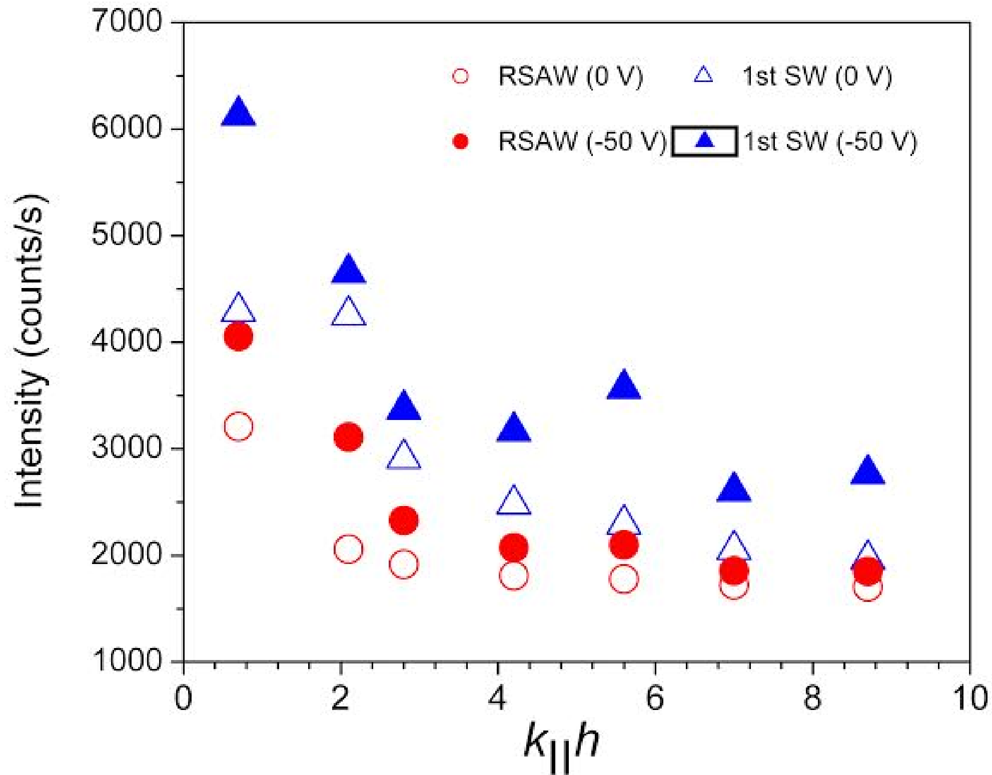

Figure 6.12: Surface acoustic wave (SAWs) dispersion curves of films produced with -50 V (circular data points) and zero (triangular data points) substrate bias voltage

The dispersion curves in Figure 6.12 show that the films produced with -50 *V* possess higher phase velocities for RSAW and film guided modes than for unbiased films. Thus, the increase in the surface phase velocities for films produced with -50 *V* substrate bias voltage corroborate the *in situ* Ar^+ incorporation and defect formation during film growth deduced from RBS. Table 6.2 shows that the elastic constants of the films fabricated with negative -50 *V* substrate bias voltage are larger than for films produced with zero substrate bias voltage [121]. The bulk modulus of the stressed and the pristine (unbiased) films are evaluated as 164 *GPa* and 171 *GPa* respectively, showing that Ar^+ incorporation due to substrate bias leads to a decrease in bulk modulus and increase in compressive stress. The Ar^+ incorporation leads to a decrease in bulk and increase in shear moduli, $G = C_{44}$ (from 21 to 49 *GPa*). In addition, the macro strains developed in the pristine and biased film were calculated from GIXRD data as 1.748×10^{-3} and 2.520×10^{-3}, respectively.

Chapter 7.

Conclusions and Future Work

7.1 Conclusions

RF magnetron sputtered BFO films on (100) Si have been studied to establish the effect of deposition conditions on film properties, based on the SZM model. FE-SEM and AFM results have shown a thickness dependent surface roughness in BFO films. Furthermore FESEM measurements have revealed a fine-grained dense columnar growth mode at low powers and coarser, larger grains of size 100-114 *nm* at elevated substrate temperatures. RBS investigations have confirmed the non-stoichiometric composition in BFO films. XRR results have shown that the film thickness and surface roughness were dependent on the sputter power (deposition rate), substrate - bias and - temperature. It has further been shown that the surface roughness increases with substrate temperature and sputter power. The roughness of the films produced by different substrate bias voltage was caused by the high energy ion bombardment that resulted in partial re-sputtering from the films and Ar^+ incorporation. The mass density of the films correlated with Bi content and Ar^+ incorporation. High mass density values were observed in films with high Bi content. GIXRD patterns have shown that low sputter powers yield amorphous phases, due to the low ad atom energy. Higher sputter powers led to nanocrystalline phases with small grain sizes. Re-sputtering facilitates the creation of nucleation sites, which favour the formation of nano- and micro-crystalline phases in BFO films. BFO films grown with negative substrate bias decreased in thickness with increased bias voltage. Substrate bias led to grain size reduction due to re-sputtering by energetic Ar^+ ions. This decrease in grain size at 600°C has been attributed to ordered coalescence of nano-crystals of BFO and it is not compatible with the predictions of the Structural Zone Model (SZM). Ar^+ incorporation due to substrate bias induced compressive stress in the films.

Surface Brillouin scattering has proven to be an excellent method to characterize

the elastic constants of the BFO thin films produced with different sputter conditions. Stress evolution has also been studied in Ar^+ incorporated films. Our film-substrate system is a slow on fast system such that the presence of the BFO thin film on the substrate reduces the velocity of RSAW (Rayleigh surface acoustic waves) and the formation of film guided modes of higher frequency, known as Sezawa waves (SWs), with displacement fields extending throughout the layer and decreasing exponentially into the substrate. Sezawa wave- like peaks called pSWs (pseudo Sezawa waves) were observed in the region above the transonic state, called hypersonic state. Moreover, the resonance and high-frequency pseudo surface modes (HFPSM) have been observed in the experimental surface Brillouin scattering measurements. Using the HFPSM mode, the value of C_{11} is determined to 270 GPa, and it corresponds to the value for the Bulk BFO. However, this value is larger than that determined using inverse extraction by the Green's function method,($C_{11} = 184 \pm 10$ GPa). This is not unusual as the values of the elastic constants of thin films are much lower compared to that of bulk.

The elastic constants of isotropic BFO thin films have been extracted by fitting the experimental dispersion curves with the calculated phase velocities, obtained by a least-squares minimization method.

A variation in the elastic constants of the BFO films with increased sputter power (50 W and 75 W) have been observed. The change in the elastic stiffness of the films with increase in sputter power is attributed to changes in film morphology and microstructure.

The residual intrinsic stress in BFO thin films is associated with Ar^+ incorporation (its ionic radius is 154 pm) and energy dissipation on the film surface, leading to the formation of nanocrystalline domains within an amorphous matrix [122],[123]. Thus the Ar^+incorporated films become more stressed than the unbiased ones at the expense of a reduced grain size (Ar^+ incorporated films are amorphous) [124].

The dispersion curves from Figure 6.12 have shown that the films produced with -50 V resulted in higher phase velocities for RSAW and film guided modes than in unbiased films. Thus, the increase in the surface phase velocities for films produced with -50 V substrate bias voltage is related to *in situ* Ar^+ incorporation and defect formation during film growth. This results in an increase in intrinsic stress in the film, as seen in the values of the elastic constants of Table 6.2. Moreover, the phase velocities are related to the elastic constants of the thin film. This is due to films produced with -50 V substrate bias voltage tend to be stiffer ($C_{11} = 222 \pm 20$ GPa, $C_{12} = 124 \pm 11$ GPa and $C_{44} = 49 \pm 4$ GPa) than for films produced with no substrate bias voltage ($C_{11} = 184 \pm 10$ GPa, $C_{12} = 141 \pm 8$ GPa and $C_{44} = 21 \pm 1$

GPa). The bulk modulus of the stressed and the pristine (unbiased) films are 164 *GPa* and 171 *GPa*, repectively. The Ar^+ incorporation decreases the bulk modulus of the BFO films.

7.2 Future work

The present work has been restricted to the fabricating and characterization of BFO thin films on Si substrates with different sputter powers, negative substrate bias voltages and substrate temperatures. The films were then studied by SBS to establish their elastic constants.

Bismuth ferrite thin films as a ferroelectric thin film material have many further research areas for the optimization of the film fabrications and characterization techniques for further improvement of the films properties. The latter include mechanical properties, domain structure, transport properties,thermal properties, polarization behavior etc. for device application purposes. In this regard some of the possible future work directions are highlighted:

- The choice of the substrate material for the growth of epitaxial thin films of this multiferroic material is very important in order to maintain and improve the mechanical, optical and functional properties (electro-magnetic properties) at a nano-meter scale. Thus, for advanced applications of the BFO thin films for integration in electronics, the use of a flexible substrate (that can be twisted and stretched) such as an elastomeric substrate (organic and plastic) should be considered. In addition for epitaxial thin film growth, substrate like $SrTiO_3$, $GdScO_3$ and $LaAlO_3$ are proposed.

- As bismuth ferrite is a multiferroic material it has ferroelectric and antiferromagnetic orderings well above room temperature. So the study of acousto-electric interactions (dielectric constants) and phonon-magnon (spin modes) scatterings using surface Brillouin study for epitaxial BFO thin films would be very valuable for optical trigger control of piezotransducers and for future applications in ferrolectric random access memory (FeRAM).

- Phase transitions studies of bismuth ferrite using surface Brillouin scattering at its curie temperature ($T_C = 643\ K$) and relation between strain and polarization fluctuations.

- Growth optimizations and characterizations of BFO films grown using molecular beam epitaxy (MBE) method.

- Functional properties studies of BFO thin films such as electrical and magnetic characterizations.
- Annealing of the thin films to understand the stress relaxations and correlate it with the evolution of electric polarization in the film should be investigated.
- It might be very interesting to study research issues that are not addressed yet; like coupling effects of different order parameters in bismuth ferrite thin film system, topological defects in domain structure, interface electrostatics, ferroelectric size effects and strain engineering.
- Future developments of novel phenomena and properties of $BiFeO_3$ thin films with broader applications (for example the physics behind controlling optically triggered piezotransducers are not yet studied).

Bibliography

[1] T. Zhao, A. Scholl, F. Zavaliche, K. Lee, M. Barry, A. Doran, M. P. Cruz, Y. H. Chu, C. Ederer, N. A. Spaldin, R. R. Das, D. M. Kim, S. H. Baek, C. B. Eom, and R. Ramesh. Electrical control of antiferromagnetic domains in multiferroic $BiFeO_3$ films at room temperature. *Nature Materials*, 5:823–829, 2006.

[2] R. Ramesh and N.A. Spaldin. Multiferroics: Progress and prospects in thin films. *Nature Mater*, 6:21–29, 2007.

[3] H. Béa, M. Bibes, S. Fusil, K. Bouzehouane, E. Jacquet, K. Rode, P. Bencok, and A Barthélémy. Investigation on the origin of the magnetic moment of $BiFeO_3$ thin films by advanced x-ray characterizations. *Phys. Rev. B*, 74:75–78, 2006.

[4] W. Eerenstein, N. D. Mathur, and J.F. Scott. Multiferroic and magnetoelectric materials. *Nature*, 442:759–765, 2006.

[5] A.Q. Jiang, C. Wang, K.J. Jin, X.B. Liu, J.F. Scott, C.S. Hwang, T.A.Tang, H.B. Lu, and G.Z. Yang. A resistive memory in semiconducting $BiFeO_3$ thin-film capacitors. *Adv. Mater*, 23:1277–1281, 2011.

[6] B.W. Wessels. Ferroelectric epitaxial thin films for integrated optics. *Annu. Rev. Mater*, 37:659–679, 2007.

[7] J. Allibe, K. Robin, E. Jacquet, I.C. Infante, S. Fusil, C. Carrétéro, J.L. Reverchon, D. Crete, J.C. Mega, A. Barthélémy, and M. Bibes. Optical properties of integrated multiferroic $BiFeO_3$ thin films for microwave applications. *Applied Physics Letters*, 96:1–5, 2010.

[8] L. Brillouin. Propagation of light in a dispersive medium. *Ann. Phys. (Paris)*, 44:203–240, 1922.

[9] P. Bao, T.J. Jackson, X. Wang, and M.J. Lancaster. Barium strontium titanate thin film varactors for room-temperature microwave device applications. *J. Phys. D*, 41:1–22, 2008.

[10] P. Ruello, T. Pezeril, S. Avanesyan, G. Vaudel, V. Gusev, I.C. Infante, and B. Dkhil. Photoexcitation of gigahertz longitudinal and shear acoustic waves in $BiFeO_3$ multiferroic single crystal. *Applied Physics Letters, American Institute of Physics (AIP)*, 100:212906–212909, 2012.

[11] S.Y. Chun. Bias voltage effect on the properties of tin films by reactive magnetron sputtering. *Journal of the Korean Physical Society*, 56:1134–1139, 2010,.

[12] B.G. Priyadarshini, S. Aich, and M. Chakraborty. Substrate bias voltage and deposition temperature dependence on properties of rf-magnetron sputtered titanium films on silicon (100). *Bull. Mater. Sci.*, 37:1691–1700, 2014.

[13] M.T. Le, Y.U. Sohn, J.W. Lim, and G.S. Choi. Effect of sputtering power on the nucleation and growth of Cu films deposited by magnetron sputtering. *Materials Transactions*, 51:116–120, 2010.

[14] P.Malik, S. Pandya, and V. Katyal. Synthesis and application of magnetic nanomaterials for memory storage devices. *International journal of advanced research*, 1:1–28, January 2013.

[15] T. Choi, S. Lee, Y.J. Choi, V. Kiryukhin, and S.W. Cheong. Switchable ferroelectric diode and photovoltaic effect in $BiFeO_3$. *Science*, 324:63–66, 2009.

[16] V.M. Fridkin. Bulk photovoltaic effect in noncentrosymmetric crystals. *Crystallogr. Rep*, 46:654–658, 2001.

[17] J. Zhang, X. Su, M. Shen, Z. Dai, L. Zhang, X. He, W. Cheng, M.U. Cao, and G. Zou. Enlarging photovoltaic effect: Combination of classic photoelectric and ferroelectric photovoltaic effects. *Sci. Rep*, 3:1–6, 2013.

[18] G. Zhang, H. Wu, G. Li, Q. Huang, C. Yang, F. Huang, F. Liao, and J. Lin. New high T_c multiferroics $KBiFe_2O_5$ with narrow band gap and promising photovoltaic effect. *Sci. Rep*, 3:1–9, 2013.

[19] J. Seidel, D. Fu, S.Y. Yang, E. Alarcon-Liado, J. Wu, R. Ramesh, and J.W. Ager. Efficient photovoltaic current generation at ferroelectric domain walls. *Phys. Rev. Lett*, 107:126805–126809, 2011.

[20] M.E. Lines and A.M. Glass. *Principles and Applications of Ferroelectrics and Related Materials*. Oxford University Press, 1977.

[21] M.H. Lee, R. Guo, and A.S. Bhalla. Pyroelectric sensors. *J. Electroceram*, 2:4:229–242, 1998.

[22] G.D. Cicco, B. Morten, D. Dalmonego, and M. Prudenziati. Pyroelectricity of PZT-based thick-films. *Sens. Actuators A*, 76:409–415, 1999.

[23] A.G. Chynoweth. Dynamic method for measuring the pyroelectric effect with special reference to barium titanate. *J. Appl. Phys*, 27:78–84, 1956.

[24] D. Pantel, S. Goetze, D. Hesse, and M. Alexe. room-temperature ferroelectric resistive switching in ultrathin $Pb(Zr_{0.2}Ti_{0.8})O_3$ films. *ACS Nano*, 5:6032–6038, 2011.

[25] J. Choi, J.S. Kim, I. Hwang, S. Hong, IK-Su. Byun, S.W. Lee, S.O. Kang, and B.H. Park. Different nonvolatile memory effects in epitaxial $Pt/PbZr_{0.3}Ti_{0.7}O_3/LSCO$ heterostructures. *Appl. Phys. Lett*, 96:262113–3, 2010.

[26] D. Ielmini, F. Nardi, and C. Cagli. Physical models of size-dependent nanofilament formation and rupture in nio resistive switching memories. *Nanotechnology*, 22:1–22, 2011.

[27] R. Waser, R. Dittmann, G. Staikov, and K. Szot. Redox-based resistive switching memories-nanoionic mechanisms, prospects and challenges. *Adv. Mater*, 21:2632–2663, 2009.

[28] R. Waser and M. Aono. Nanoionics-based resistive switching memories. *Nat. Mater*, 2007.

[29] M. Ohring. *Materials Science of Thin Films*. Elsevier: Amsterdam, the Netherland, 2001.

[30] L.I. Mandelshtam. Light scattering by inhomogeneous media. *Zh. Russ. Fiz-Khim.Ova*, 58:381–395, 1926.

[31] G.B. Benedek and K. Fritsch. Brillouin scattering in cubic crystals. *Phys. Rev*, 149:647–662, 1966.

[32] R.W. Gammon and H.Z. Cummins. Brillouin-scattering dispersion in ferroelectric triglycine sulfate. *Phys. Rev. Lett*, 17:193–195, 1966.

[33] E.M. Brody and H.Z. Cummins. Brillouin scattering study of the ferroelectric transition in KH_2PO_4. *Phys. Rev. Lett*, 21:1263–1266, 1968.

[34] J.D. Comins. *Handbook of elastic properties of solids, liquids, and gases, vol 1. Dynamic methods for measuring the elastic properties of solids*. Academic Press, San Diego, 2001.

[35] J.R. Sandercock. In M. Balkanski, editor, *In Proc. 2nd Int. Conf. on Light Scattering in Solids*, pages 9–12. Paris: Flammarion, 1971.

[36] V. Bortolani, F. Nizzoli, and G. Santoro. Strong interference effects in surface brillouin scattering from a supported transparent film. *Phys. Rev*, 25:3442–3445, 1982.

[37] M. Montagna. Brillouin and raman scattering from the acoustic vibrations of spherical particles with a size comparable to the wavelength of the light. *Physical Review B*, 77:1–9, 2008.

[38] L. Sui, L. Huang, P. Podsiadlo, N.A. Kotov, and J. Kieffer. Brillouin light scattering investigation of the mechanical properties of layer-by-layer assembled cellulose nano crystal films. *Macromolecules*, 43:9541–9548, 2010.

[39] H.T. Nguyen, G. Gubbiotti, M. Madami, S. Tacchi, and M.G. Cottam. Brillouin light scattering study of the spin dynamics in nanoscale permalloy stripes: Theory and experiment. *Microelectronics Journal*, 40:598–600, 2009.

[40] E. Salas, R.J. Jimenez-Rioboo, A. deAndres, and C. Prieto. Brillouin light scattering characterization of the surface acoustic wave velocity in SP_2 allotropes thin films. *Eur.Phys.J.B*, 75:151–155, 2010.

[41] N. Lou, G. Benassayag, and A. Zwick. Acoustics at nanoscale: Raman-brillouin scattering from thin silicon-on-insulator layers. *Applied Physics Letters*, 97:141908–141911, 2010.

[42] G. Gubbiotti, S. Tacchi, M. Madami, G. Carlotti, A.O. Adeyeye, and M. Kostylev. Brillouin light scattering studies of planar metallic magnonic crystals. *J. Phys. D: Appl. Phys*, 43:1–14, 2010.

[43] Q. Zhao, M. Guerette, and L. Huang. Nanoindentation and Brillouin light scattering studies of elastic moduli of sodium silicate glasses. *Journal of Non-Crystalline Solids*, 358:652–657, 2012.

[44] B.A. Mathe. *Surface Brillouin scattering studies of elastic properties of materials at high temperature*. PhD thesis, School of Physics, University of the Witwatersrand, 2008.

[45] V. Bortolani, A.M. Marvin, F. Nizzoli, and G. Santoro. Theory of brillouin scattering from surface acoustic phonons in supported films. . *Phys. C: Solid State Phys*, 16:1757–1776, 1983.

[46] E. Borissenko, M. Goffinet, A. Bosak, P. Rovillain, M. Cazayous, D. Colson, P. Ghosez, and M. Krisch. Lattice dynamics of multiferroics $BiFeO_3$ studied by inelastic x-ray scattering. *J. Phys.: Condens. Matter*, 25:1–7, 2013.

[47] S. L. Shang, G. Sheng, Y. Wang, L. Q. Chen, and Z. K. Liu. Elastic properties of cubic and rhombohedral $BiFeO_3$ from first principles calculations. *Physical Review B*, 80:1–4, 2009.

[48] M. P. Cruz, Y.H. Chu, J.X. Zhang, P.L. Yang, F. Zavaliche, Q. He, P. Shafer, L.Q. Chen, and R. Ramesh. Strain control of domain-wall stability in epitaxial $BiFeO_3$ (110) films. *Phys. Rev. Lett.*, 99:217601–217605, 2007.

[49] S. Nakashima, D. Ricinschi, J.M. Park, T. Kanashima, H. Fujisawa, M. Shimizu, and M. Okuyama. Ferroelectric and structural properties of stress-constrained and stress-relaxed polycrystalline $BiFeO_3$ thin films. *Journal of Applied Physics*, 105:1–6, 2009.

[50] L.W. Martin, S.P. Crane, Y.H. Chu., M.B. Holcomb, M. Gajek, M. Huijben, C.H. Yang, N. Balke, and R. Ramesh. Multiferroics and magnetoelectrics: thin films and nanostructures. *J. Phys.: Condens. Matter*, 20:1–13, 2008.

[51] C. Michel, J.M. Moreau, G.D. Achenbach, R. Gerson, and W.J. James. The atomic structure of $BiFeO_3$. *Solid State Communications*, 7:701–704, 1969.

[52] B.T. Ruette. *Induced Phase Transition in Magnetoelectric* $BiFeO_3$ *Crystals, Thin-layers and Ceramics*. PhD thesis, Materials Science and Engineering, 2003.

[53] J.R. Teague, R. Gerson, and J. James. Dielectric hysteresis in single crystal $BiFeO_3$. *Solid State Communications*, 8:1073–1074, 1970.

[54] J. Wang, H. Zheng, Z. Ma, S. Prasertchoung, M. Wutting, R. Droopad, J. Yu, K. Eisenbeiser, and R. Ramesh. Epitaxial $BiFeO_3$ thin films on si. *Appl. Phys. Lett*, 85:2574–2576, 2004.

[55] G. Lawes and G. Srinivasan. Introduction to magnetoelectric coupling and multiferroic films. *J. Phys. D: Appl. Phys*, 44:1–22, 2011.

[56] I.M. Sosnowska. Neutron scattering studies of $BiFeO_3$ multiferroics: a review for microscopists. *Journal of Microscopy*, 236:109–114, 2009.

[57] R. Cebulla, R. Wendt, and K. Ellmer. Al-doped Zinc oxide films deposited by simultaneous rf and dc excitation of a magnetron plasma: relationships between plasma parameters and structural and electrical film properties. *Journal of Applied Physics*, 83:1087–1095, 1998.

[58] T. Hanabusa, H. Hosoda, K. Kusaka, and K. Tominaga. Abnormal residual stress state in ZnO films synthesized by planar magnetron sputtering system with two facing targets. *Thin Solid Films*, 343-344:164–167, 1999.

[59] L.D. Landau and E.M. Lifshitz. *Electrodynamics of Continouos media*. Pergamon press, 1970.

[60] R. E. Newnham. *Properties of Materials: Anisotropy, Symmetry, Structure*. Oxford University Press, Oxford, UK, 2005.

[61] X. Zhang, J.D. Comin, A.G. Every, P.R. Stoddart, W. Pang, and T.E. Derry. Surface brillouin scattering study of the surface excitations in amorphous silicon layers produced by ion bombardment. *Physical Review B*, 58:13677–13685, 1998.

[62] X. Zhang. *Surface Brillouin scattering studies of bulk materials and thin films*. PhD thesis, School of Physics, University of the Witwatersrand, 1999.

[63] W. Cheng. *Hypersonic Elastic Excitations in Soft Mesoscopic Structures : A Brillouin light scattering study*. PhD thesis, der Johannes Gutenberg-Universität Mainz, 2007.

[64] G.W. Farnell and E.L. Adler. *Physical Acoustics*. Academic Press, N.Y, 1972.

[65] T. Wittkowski, K. Jung, B. Hillebrands, and J.D. Comins. Structural and chemical phase transitions in tungsten carbide films evidenced by the analysis of their stiffness tensors. *Journal of applied physics*, 100:1–11, 2006.

[66] J.A. Rogers, A.A. Maznev, M.J. Banet, and K.A. Nelso. Optical generation and characterization of acoustic waves in thin films: Fundamentals and applications. *Annu.Rev.Mater.Sci.*, 30:117–174, 2000.

[67] J.R. Sandercock. Light scattering from surface acoustic phonons in metals and semiconductors. *Solid State Communications*, 26:547–551, 1978.

[68] T. Blachowicz. *Brillouin spectroscopy in crystal lattices, acoustic and spin waves*. Silesian University of Technology, 2003.

[69] B.A. Auld. *Acoustic fields and waves in solids*. R.E. Krieger, 1990.

[70] R. Loudon and J.R. Sandercock. Analysis of the light-scattering cross section for surface ripples on solids. *J. PhyJ. P: Solid State Phys*, 13:2609–2631, 1980.

[71] R.E. Kumon and M.F. Hamilton. Effect of harmonic phase on nonlinear surface acoustic waves in the (111) plane of cubic crystals. *J. Acoustic.soc.am*, 113:1293–1303, 2003.

[72] M.G. Beghi, A.G. Every, and P.V. Zinin. *Ultrasonic nondestructive evaluation Engineering and Biological Material Characterization*. CRC Press, 2003.

[73] T. Wittkowski, J. Jorzick, K. Jung, and B. Hillebrands. Elastic properties of thin h-BN films investigated by Brillouin light scattering. *Thin Solid Films*, 353:137–143, 1999.

[74] E.D. Mcclanahan and N. Laegreig. *Sputtering by particle bombardment III:Characteristics of Sputtered Particles, Technical Applications*. Berlin: Springer Verlag, 1991.

[75] R. Behrisch. *Sputtering by particle bombardment; physical sputtering of single-element solids*. Berlin: Springer Verlag, 1981.

[76] P.M. Karimi. *Atomic Mechanisms of Stress Formation of Group IVB-VIB Transition Metal Nitrides Deposited by DC Magnetron Sputtering*. PhD thesis, Physikalischen Insitut , RWTH Aachen, 2007.

[77] L. Meng. *Plasma Diagnostic and ITO film deposition by RF-assisted closed-field dual magnetron system*. PhD thesis, Department of Nuclear, Plasma, and Radiological Engineering University of Illinois at Urbana-Champaign, 2010.

[78] F.A.M. Visinoiu. *Growth mechanism and structure of epitaxial perovskite thin films and superlattices*. PhD thesis, Martin-Luther-Universität, 2003.

[79] J. A. Floro, E. Chason, R.C. Cammarata, and D.J. Srolovitz. Physical origins of intrinsic stresses in volmer-weber thin films. *MRS Bulletin*, 27:19–25, 2002.

[80] C. V. Thompson and R. Carel. Texture development in polycrystalline thin films. *Materials Science and Engineering B*, 32:211–219, 1995.

[81] C. V. Thompson. Structure evolution during processing of polycrystalline films. *Annual Reviews of Materials Science*, 30:159–190, 2000.

[82] I. Petrov, P.b. Bama, L. Hultman, and J.E. Greene. Microstructural evolution during film growth. *Journal of Vacuum Science and Technology A*, 21:117–128, 2003.

[83] M. Ohring. *The Materials Science of Thin Films*. Academic Press Inc., San Diego, 2002.

[84] D. A. Porter and K. E. Easterling. *Phase transformations in Metals and Alloys*. Nelson Thornes Ltd., Cheltenham, United Kingdom, 2001.

[85] C. V. Thompson. Grain growth in thin films. *Annual Review of Materials Science*, 20:245–268, 1990.

[86] J. E. Burke. Some factors affecting the rate of grain growth in metals. *Transactions of the American Institute of Mining and Metallurgical Engineers*, 180:73–91, 1949.

[87] C. Suryanarayana and C. C. Koch. Nanocrystalline materials - current research and future directions. *Kluwer Academic Publisher*, 130:5–44, 2000.

[88] J. Hu. *Grain Growth by Ordered Coalescence of Nanocrystals in Ceramics*. PhD thesis, Department of Materials and Environmental Chemistry, Stockholm University, 2013.

[89] J. A Thornton. High rate thick film growth. *Annual Review of Materials Science 7*, 7:239–260, 1977.

[90] B. Merle. *Mechanical Properties of Thin Films Studied by Bulge Testing*. PhD thesis, FAU University, 2013.

[91] E. Alfonso, J. Olaya, and G. Cubillos. Thin film growth through sputtering technique and its applications. *Universidad Nacional de Colombia Colombia*, 15:397–432.

[92] J.E. Greene. Nucleation, film growth, and microstructural evolution, deposition processes for films and coating. *Noyes Publications*, 2:681–739, 1994.

[93] Y. Wang, W. Chen, B. Wang, and Y. Zheng. Ultrathin ferroelectric films: Growth, characterization, physics and applications. *Materials*, 7:6377–6485, 2014.

[94] M. Ohring. *Materials science of Thin Films: Deposition and Structure*, volume Second edition. Academic Press Inc., San Diego, 2002.

[95] T.J. Vink, W. Walrave, J.L.C. Daams, P.C. Baarslag, and J.E.A.M. van den Meerakker. On the homogeneity of sputter-deposited ITO films part i. stress and microstructure. *Thin Solid Films*, 266:145–151, 1995.

[96] B. Chapman. *Glow Discharge processes*. John Wiley and Sons, 1980.

[97] N. Martin, D. Baretti, C. Rousselot, and J.Y. Rauch. The effect of bias power on some properties of titanium and titanium oxide films prepared by r.f. magnetron sputtering. *Surface Coat*, 107:172–182, 1998.

[98] E. Terzini, P. Thilakan, and C. Minarini. Properties of ITO thin films deposited by rf reactive magnetron sputtering at elevated substrate temperature. *Material science and engineering B*, 77:110–114, 2000.

[99] *DIFFRACPlus TOPAZ Software, Bruker AXS GmbH, Karlsruhe, Germany, 2006-2009.*

[100] J.L. Perry. Effects of sputter deposition parameters on stress in tantalum films with applications to chemical mechanical planarization of copper. Master's thesis, Rochester Institute of Technology, 2004.

[101] J.D. Bucci, B.K. Robertson, and W.J. James. The precision determination of the lattice parparamet and the ccoefficient of thermal expansion of $BiFeO_3$. *J. Apply. Cryst.*, 5:187–191, 1972.

[102] H. Watanabe, N. Yameda, and M. Okaji. Linear thermal expansion coefficient of silicon from 293 to 1000k. *International Journal of Thermophysics*, 25:221–236, 2004.

[103] H. Guo and M. Alam. Strain in cvd diamond films: effects of deposition variables. *Thin Solid Films*, 212:173–179, 1992.

[104] Uppsala university department of physics and materials science. atomic force microscopy (afm). website, april 2010. http://surfint.fysik.uu.se/ techniques.afm.html.

[105] G.J. Simpson, D.L. Sedin, and K.L. Rowlen. Surface roughness by contact versus tapping mode atomic force microscopy. *Langmuir*, 15:1429–1434, 1999.

[106] *DIFRRACPLUS LEPTOS 7 Software, Bruker AXS GmbH, Karlsruhe, Germany, 2006-2009.*

[107] Genplot and rump documentation, http://genplot.com/.

[108] H. A. Basantani. Effect of rf substrate bias on vanadium oxide thin films during reactive pulsed dc magnetron sputter deposition. Master's thesis, The Pennsylvania State University The Graduate School, 2011.

[109] L. Kotane. Study of elastic properties of semiconductors by surface brillouin scattering. Master's thesis, School of Physics, University of the Witwatersrand, 2010.

[110] C. Sumanya. *Surface Brillouin scattering in opaque thin films and bulk materials*. PhD thesis, School of Physics, University of the Witwatersrand, 2012.

[111] R. Mock, B. Hillebrands, and R. Sandercock. Construction and performance of a Brillouin scattering setup using a triple-pass tandem Fabry-perot interferometer. *J. Phys. Instr*, 20:656–659, 1987.

[112] *SPM Training Notebook 004-130-000 (standard) 004-130-100 (cleanroom), 2003 Veeco Instruments Inc.*

[113] H. Savaloni, A. Taherizadeh, and A. Zendehnam. Residual stress in Cu sputtered films on glass substrates at different substrate temperatures. *Physica B*, 15:277–282, 2004.

[114] C. W. Jennings. Surface roughness and bond strength of adhesives. *J Adhesion*, 4:25–38, 1972.

[115] P.W. Paul, M. Guttag, and C.S. Tu. Surface modification of multiferroic $BiFeO_3$ ceramic by argon sputtering. *Journal of Surface Engineered Materials and Advanced Technology*, 4:295–308, 2014.

[116] S. Migita, K. Sakai, H. Ota, Z. Mori, and R. Aoki. The influence of Bi-sticking coefficient in the growth of Bi (2212) thin films by ion beam sputtering. *Thin solid films*, 281-281:510–512, 1996.

[117] R. Vanselow and R. Howe. Chemistry and physics of solid surfaces vii. *Springer series in surface sciences 10, Springer-Verlag Berlin Heidelberg*, 1988.

[118] H. Yan, N. Ding, G. Wu, P. YanP. Yang. Chu, and H. Deng. The influence of bi content on the properties of bismuth ferrite thin films fabricated by magnetron sputtering. *Materials Science Forum*, 745-746:131–135, 2013.

[119] T. Wittkowski, K. Jung, and B. Hillebrands. Brillouin light scattering study on nanoporous low dielectric constant films. *AG Magnetismus.Universitat Kaiserslautern.*, 6:1–3.

[120] D. Flototto. *Mechanisms of intrinsic Stress formation in thin film systems*. PhD thesis, Max-Planck-Institute for Intelligent System, Stuttgart, 2013.

[121] D.M. Wamwangi, C. Sumanya, T.Wittkowski, and J. D. Comins. Stress relaxation of rf sputtered Cr_3C_2 thin films by surface brillouin scattering. *World Conference on Nondestructive testing*, 18:1–6, 2012.

[122] D. J. Cohen, K.C. Ruthe, and S.A. Barnett. Transparent conducting Zn1-xMgxO:(Al,In) thin films. *Journal of Applied Physics*, 96:459–467, 2004.

[123] P. Nunes, E. Fortunato, P. Tonello, F.B. Fernandes, P. Vilarinho, and R. Martins. Effect of different dopant elements on the properties of ZnO thin films. *Vacuum*, 64:281–285, 2002.

[124] K. Srinivasarao, G. Srinivasarao, K. V. Madhuri, K.K. Murthy, and P. K. Mukhopadhyay. Preparation and characterization of r.f. magnetron sputtered Mo:ZnO thin films. *Hindawi Publishing Corporation*, 684730:1–7, 2013.